NORTHWESTERN UNIVERSITY

Structural Studies of Particulate Methane Monooxygenase in a Native Lipid Bilayer

A DISSERTATION

SUBMITTED TO THE GRADUATE SCHOOL
IN PARTIAL FULLFILLMENT OF THE REQUIREMENTS

for the degree

DOCTOR OF PHILOSOPHY

Field of Interdisciplinary Biological Sciences

By

Christopher Wellington Koo

EVANSTON, ILLINOIS

June 2022

ABSTRACT

Methanotrophs, bacteria that can metabolize methane, remain a promising solution to mitigating the effects of climate change by removing atmospheric methane and converting it to useful chemical precursors. However, a full understanding of the main enzyme they use to oxidize methane, particulate methane monooxygenase (pMMO), is critical for harnessing their unique metabolism. pMMO has several features that have made it a challenging enzyme to study. pMMO is a multi-subunit membrane enzyme, precluding a recombinant expression system and requiring disruptive detergents to isolate from the cell membrane, causing a loss of activity with each step of purification. It requires copper for activity and yet too much copper is inhibitory. In addition, advanced spectroscopy remains difficult since only Cu(II) has an electron paramagnetic resonance (EPR) signature while Cu(I) is EPR-silent. Finally, while genetic tools for methanotrophs are available, pMMO continues to resist mutagenesis studies. Despite these challenges, steady progress has been made on understanding the enzyme by applying cutting-edge techniques and taking new approaches.

At the beginning of this dissertation work in 2016, crystal structures from multiple species of methanotrophs consistently revealed the trimer-of-trimers structure composed of subunits PmoA, PmoB, and PmoC, and two conserved copper binding sites, Cu_B and Cu_C. During this time, attention had started to shift from the periplasmic Cu_B site to the strictly conserved Cu_C site embedded in the membrane as the possible active site. Cu_C was shown to be labile compared to Cu_B and could be replaced with zinc, inhibiting activity. Concerningly, there was always ~25 amino acid stretch of disorder in the crystal structures near Cu_C that contained strictly conserved residues. Additionally, Cu_B could be modeled as both mono- or dinuclear copper ions in some pMMO crystal structures. During the course of this work, efforts focused on re-creating the

membrane environment around pMMO in order to study it in a native-like environment. Bicelles successfully restored enzymatic activity and nanodiscs were shown to recover activity as well. At the same time, a double electron-electron resonance (DEER) study showed that Cu_C in purified pMMO samples contained copper and electron-nuclear double resonance (ENDOR) was used to determine that Cu_B was mononuclear. A native top-down mass spectrometry study on pMMO embedded in nanodiscs linked enzyme activity with the presence of at least one copper in the PmoC subunit.

In this thesis dissertation, three more techniques were used to characterize pMMO: single-particle cryogenic electron microscopy (cryoEM), cryogenic electron tomography (cryoET), and cell-free protein synthesis (CFPS). The cryoEM study resulted in the highest resolution structure (2.14 Å) of pMMO to date in a nanodisc with lipids derived from the methanotroph and structures from three species in total. These structures uncovered stabilized lipids within the enzyme, structural features in the previously disordered region, and a new copper site (Cu_D), creating a new paradigm for modeling the architecture of the active site. A collaborative study using cryoET resulted in the highest resolution structure of a membrane protein using this technique (4.8 Å) and revealed the in vivo array organization of pMMO within the specialized intracytoplasmic membranes that stretch across the body of the methanotroph. Finally, the CFPS study resulted in the foundation of a viable recombinant platform for expressing the pMMO complex and generating mutants. Together, these studies highlight the importance of investigating pMMO in its native environment and highlights new possibilites that cryoEM and synthetic biology techniques can bring to future pMMO studies.

ACKNOWLEDGEMENTS

First, thanks to my advisor and mentor Amy Rosenzweig. Amy, your guidance, thoughtfulness, and leadership have helped me to be a better scientist and a better person. I'll always strive to be as practical, efficient, thoughtful, and composed as you always manage to be in the face of any situation. I always felt reassured knowing that a conversation with you could stop my fixating and provide a clear path forward. I am grateful for all the times I'd swing by your office and, no matter what you were in the middle of, leave an hour later with a clear and practical idea of what to do next. Knowing I had a supportive mentor gave me such a sense of confidence to try new things and to not worry as much about failed experiments, knowing that we could discuss the results either way. I appreciate all the time, latitude, and funding that you gave me to learn and play around with various approaches. I'm grateful to have a good role model to emulate and positive examples to draw upon in the face of complexity and adversity. Thanks Amy!

Thanks also to Yuan He, who's mentorship and support helped me get my main project off the ground. Thanks for sitting with me while I struggled along with the cryoEM and microscope techniques and for pointing me in the right directions whenever I hit a wall with my project. I'm so grateful for your time and encouragement! Thanks also to Ryan Abdella, Jonathan Remis, Rahul Purohit, Kasia Soczek, and Jason Pattie who were great resources along the way as I learned cryoEM techniques and data processing. Thanks to my co-author Frank Tucci for being a great rotation student and now indispensable lab member and for helping me take this project across the finish line. You really helped me plow through a tough period of the project and it was fun working with and commiserating with you along the way. Thanks to my mentors in the lab – Grace Kenney during my rotation and Soo Ro afterwards – for teaching me about keeping methanotrophs happy and how to be successful doing research. Thanks also to my numerous collaborators through the

years including Yanan Zhu, Zhengyi Yang, and Peijun Zhang at Oxford, Jasmine Hershewe, Andrew Hunt, and Mike Jewett in the Chemical Engineering Department and Luis Schachner in the Kelleher lab.

Thanks to my parents and my family for all your support along the way. I have been so lucky to have the opportunities that you made possible for me and am grateful to have been welcomed into new families along the way. Graduate school certainly taught me to be a better scientist, but the challenges taught me about what things in life are essential and what is just background noise – thanks for helping me remember what is most important. I'm grateful for the new connections and reconnections during this time and I'm looking forward to the next chapter where hopefully I'll live closer to everyone in the family.

Thanks so much to my friends from before Northwestern. You all helped me keep perspective during this time and reminded me that life goes on outside of lab and Northwestern. Particularly Eric, Julie, David, Vince x2, Virginia, and Vivian – your friendship means a lot to me and I'm glad that we've stayed in touch though the years. Thanks for supporting me and pushing me through challenging times and sharing in the good times with me. Thanks also to the original UCLA Dragonboat Chicago diaspora – Patrick, Vince, Virginia, Colleen, Chris and Kevin. Those thanksgivings, picnics, and get-togethers were a great way to be welcomed to a new city! Also thanks to my longtime friend Justin who helped inspire me to take the leap to grad school and our longtime partner in crime, Chris.

Thanks to my science mentors through the years starting with my high school chemistry teacher, Bethany Blackwell, who is such a great teacher and taught me to appreciate science. Thanks to the UCLA PETC crew – Mark Arbing, Sum Chan, and Annie Shin. You taught me to enjoy research and patiently helped me learn the skills to succeed at Northwestern. Also thanks to

Jack Bracken for always being entertaining, always bringing good vibes (aka a bottle of whiskey), and teaching me about the grad school experience. Thanks also to Todd Yeates for encouraging me to pursue my PhD.

Thanks to my current and former Rosenzweig labmates. Former labmates – Aaron and Laura – thanks for welcoming me to the lab - I learned a lot about the day-to-day of doing research from the examples you set. Tom, thanks for breaking down that professional atmosphere whenever you had the chance – I'm glad we overlapped a bit and I got to see how to be a bit irreverent while doing great work. Oriana and Rahul, it was great hanging out and I'm glad to see you succeeding in your own endeavors. Grace, thanks for showing the ropes and getting me off the ground in the lab, I appreciate all the time you took to get me going. Matt, I learned a lot about chemistry from you and learned about how approaching the same project from different directions can lead to a much more holistic overall result. Candy, Yue Wen, Amanda, Hong - you are all rockstars, thanks for keeping the lab fun and keeping me in the loop on youth culture. Thanks to Yunji for being a pMMO fan and helping me stay grounded while doing research. We made a good team in the end! Tasha, thanks for waking up early with me for those cycle classes. Rose, it's been great getting to work with you more recently. Dayna, it's been great to meet you, I hope you have a lot of fun during your time here! Frank, it's always great chatting about pMMO and sci-fi with you, I'm excited to see where your project ends up. Reyvin, thanks for teaching me about K-pop culture. Gerri, you're becoming a true multidisciplinary expert, keep it up! Ricky, thanks for your deep dives into figuring out what the heck is going on at the pMMO copper sites and the toolbox of techniques you've helped me understand better. Madison, thanks for always being down to chat. Caitlin, and Joey thanks for bringing so much enthusiasm to the lab and your work. I hope you enjoy your journey through grad school!

Thanks to my friends that I made at Northwestern. Laughter and commiseration were essential ingredients for getting through grad school. The lab shutdown in 2020 helped me realize how randomly dropping into your labs to visit, catching up at seminars, and running into each other while getting coffee were vital to my grad school experience. I'm glad that we got through it and have had time to reconnect before we all leave. Thanks to the biophysics crew Alexis and Nic – you guys were my first friends at Northwestern and after going through the Biophysics training program together and working near each other all this time, I'm glad that we'll be graduating together! I'll have fond memories of shooting the breeze in the hallways or eating lunch together, always lingering and laughing just a bit longer before getting back to it. Thanks to my apartment-mate Kristin who helped me be a better cook and a more independent, capable, passionate person. I'm so grateful now that we threw all those get-togethers when we had the chance! Thanks to my pandemic buddy Nicolle - I think that we're going to be lifelong friends after going through that together. I am grateful that it brought us closer and may we never have to do that again! Also thanks to the pod: Yunji, John, and Soo. Looking forward to beating the next Overcooked game with you all. Thanks to Vas for your unlimited energy and indominable spirit through the years. Thanks to my Chicago adventure buddy Miranda - we really did turn out to be BEST FRIENDS.

Finally, thanks to my #1 KakaoTalk friend - 다람쥐 사랑해.

TABLE OF CONTENTS

LIST OF TABLES AND FIGURES

CHAPTER 1: Introduction to methanotrophs and methane monooxygenases

Previous versions of this chapter have been published as:

Christopher W. Koo & Amy C. Rosenzweig, *Chem. Soc. Rev.* (2021)

Christopher W. Koo & Amy C. Rosenzweig in *Encyclopedia of Inorganic and Bioinorganic Chemistry* (2020)

1.1. Abstract

Methanotrophic bacteria represent a potential route to methane utilization and mitigation of methane emissions. In the first step of their metabolic pathway, aerobic methanotrophs use methane monooxygenases (MMOs) to activate methane, oxidizing it to methanol. There are two types of MMOs: a particulate, membrane-bound enzyme (pMMO) and a soluble, cytoplasmic enzyme (sMMO). The two MMOs are completely unrelated, with different architectures, metal cofactors, and mechanisms. The more prevalent of the two, pMMO, is copper-dependent, but the identity of its copper active site remains unclear. By contrast, sMMO uses a diiron active site, the catalytic cycle of which is well understood. Here we review the current state of knowledge for both MMOs, with an emphasis on recent developments and emerging hypotheses. In addition, we discuss obstacles to developing expression systems, which are needed to address outstanding questions and to facilitate future protein engineering efforts.

1.2. Introduction

During an era of unprecedented climate change, increasing atmospheric methane concentrations are a constant source of concern and debate.[1,2] Anthropogenic methane emissions from oil and gas production, livestock, and agriculture threaten to fuel unstoppable global warming if left unchecked. Methane is the second most abundant greenhouse gas after carbon dioxide and accounts for at least 25% of current global warming. Moreover, its superior heat-trapping capacity confers a global warming potential 84 times that of carbon dioxide over a 20-year period. The effectiveness of methane as a greenhouse gas combined with its ~10 year lifetime means that immediate small reductions in atmospheric methane can have a large impact on climate change.[3]

Unlike other greenhouse gases, methane can be converted to desirable fuels and chemicals, which could simultaneously mitigate global warming and meet increasing energy demands.[4] However, activation of the 105 kcal mol^{-1} methane C-H bond[5] presents a significant challenge. Industrial methods rely on the conversion of methane and water to a mixture of carbon dioxide and hydrogen (syngas) followed by Fischer-Tropsch synthesis of longer-chain hydrocarbons.[6] This technically complex and expensive process must be carried out in large refineries to capture economies of scale.[4] The high capital expenses combined with the abundance of methane in remote locations have renewed interest in biological methane activation, which offers the possibility of deployable smaller-scale methods with higher conversion efficiencies and less environmental impact.[7-9] Aerobic biological methane activation occurs in a group of methane-consuming bacteria called methanotrophs.[10,11] In contrast to energy-intensive industrial processes, methanotrophs activate methane at ambient temperature and pressure. Harnessing this unique ability could dramatically alter industrial methane processing practices.[12-14]

Aerobic methanotrophs were historically divided into two groups based on metabolic pathways, membrane lipid content, and physical characteristics. *Gammaproteobacteria* comprise the first group, commonly referred to as type I. These methanotrophs are distinguished by their use of the ribulose monophosphate (RuMP) pathway for carbon assimilation,[15,16] membranes comprising mainly 14-16 carbon phospholipids,[17] and disc-shaped intracytoplasmic membrane (ICM) structures. The second group, type II, consists of *Alphaproteobacteria* that use the serine pathway,[16] have primarily 18-carbon membrane phospholipids in their membranes,[18] and exhibit ICMs along the periphery of the cells. As new species have been characterized, types I and II have become synonymous with *Gammaproteobacteria* and *Alphaproteobacteria*.[19] A third group of methanotrophs, the *Verrucomicrobia*, was discovered recently.[20] These methanotrophs live at extreme temperatures, use the Calvin-Benson-Bassham cycle, and possess mainly saturated phospholipids.[21,22] Methanotrophs of all types are common in soils, rice paddies, swamps, and lakes where they have access to anthropogenic and bacterial sources of methane.[10] In addition, methanotrophs inhabit the tundra,[23] salt lakes,[24,25] and volcanic soil[26-29] where they oxidize methane under extreme conditions of temperatures, salinity, and acidity. Understanding the enzymes involved in methane activation under these wide-ranging conditions is critical to realizing the biotechnological potential of methanotrophs.

Methane activation is accomplished by methane monooxygenase enzymes (MMOs), which convert methane to methanol in the first step of methanotroph metabolism (eq. 1). Methanol is then converted to formaldehyde by methanol dehydrogenase (MDH), after which the metabolic pathways diverge depending on the type of methanotroph.[16] There are two types of MMO: the copper-dependent, membrane-bound or particulate methane monooxygenase (pMMO) and the iron-dependent, soluble methane monooxygenase (sMMO).[30-32] pMMO is the primary MMO in nature and is present in all methanotrophs except a few species from the *Methylocella*[33,34] and *Methyloferula*[35] genera, which only possess sMMO.[11] pMMO is typically housed within extensive ICM structures,[36,37] and is highly abundant, representing ~20% of the total protein in the cell.[38,39] Under copper-starved conditions, some methanotrophs utilize sMMO, expression of which is regulated by a poorly-understood mechanism called the copper switch.[40,41] Once copper becomes available, sMMO expression is downregulated by 2-3 orders of magnitude, ICMs form, and pMMO is mildly upregulated.[42]

$$CH_4 + O_2 + 2e^- + 2H^+ \longrightarrow CH_3OH + H_2O \quad \text{(eq. 1)}$$

Although pMMO is more prevalent across methanotroph species, progress toward elucidating its active site and mechanism has been hampered by challenges intrinsic to handling integral membrane proteins. By contrast, sMMO, which is more amenable to study due to its soluble nature, is better understood. One challenge common to the two MMOs is the lack of a recombinant expression system.[43-46] The catalytic components of sMMO and pMMO must instead be isolated and purified directly from native methanotrophs, precluding generation of site-directed mutants. Nevertheless, each MMO has been studied extensively by biochemical, spectroscopic, and structural techniques. Several key aspects of both MMOs have been revisited in the past five years, altering and enriching our understanding of how these enzymes work. Here we review the current state of knowledge with an emphasis on recent developments and areas of controversy.

1.3. Particulate methane monooxygenase

1.3.1. Overall structure

pMMO consists of three subunits encoded by the *pmoCAB* operon, which is present in up to three copies in the methanotroph genome, depending on the species.[27,47-55] Most methanotrophs also possess up to two extra copies of *pmoC* that are relatively divergent from those in the *pmoCAB* operons.[56,57] Since methanotrophs are frequently identified by detection of the *pmoA* gene in soil or marine bacterial populations using mRNA probes, *pmoA* genes are highly represented in databases.[58]

Crystal structures of pMMOs from five species have been determined.[59-63] The three subunits, PmoA (α), PmoB (β), and PmoC (γ), form an αβγ protomer, and three protomers related by a threefold axis of symmetry form the full $(\alpha\beta\gamma)_3$ oligomer (Fig. 1.1). This trimer, observed in all pMMO structures, adopts a cylindrical shape approximately 90 Å in diameter and 105 Å in length. PmoA (24 kDa) and PmoC (22 kDa) are composed of 7 and 5 transmembrane helices, respectively, and are almost entirely embedded in the lipid bilayer. PmoB (42 kDa) comprises a soluble domain of two cupredoxin-like folds that are connected by two transmembrane helices.[59] In crystal structures of pMMO from type II methanotrophs,[60-62] an ~20 residue helix cocrystallizes with the full complex, adjacent to each PmoC subunit with a lipid mediating the interaction (Fig. 1.2).[62] This helix has yet to be identified, and is reminiscent of supernumerary subunits found in the crystal structures of some respiratory complexes.[64] Additional lipids have been observed in the pMMO crystal structures, and may regulate activity and assembly.[62]

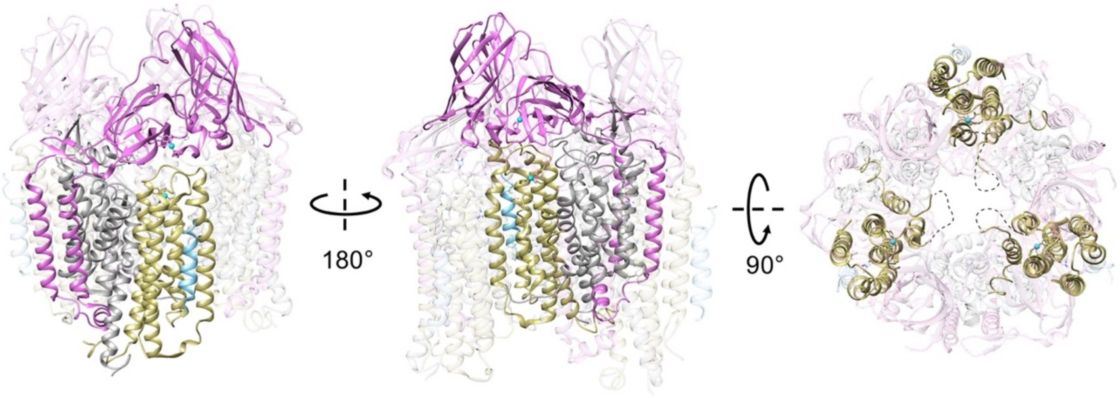

Figure 1.1. **Crystal structure of pMMO from *Mc.* sp. Rockwell** (PDB accession code 4PI0).[62] The PmoB subunits are shown in pink, the PmoA subunits are shown in gray, the PmoC subunits are shown in yellow, and the unidentified helix is shown in blue. Copper ions are shown as cyan spheres. In the two left images, a single αβγ protomer is highlighted. In the right top down image, the PmoC subunits are highlighted and the location of the unmodeled, highly conserved region is marked with a dashed line.

In all crystal structures of pMMO, there is significant disorder in the PmoC region, rendering it impossible to model part of the sequence (Figs 1.1, 1.2). In *Mc*. sp. str. Rockwell pMMO, this disordered region corresponds to residues 199–225,[62] which are also the most conserved residues among PmoC sequences. Perhaps due to this flexibility, the conformation of PmoC varies the most among species (Figure 1.2). This disorder and variability may be related to the loss of activity upon detergent solubilization.[38,63] Finally, several lipid molecules are found in the structure of *Mc*. sp. str. Rockwell pMMO, mediating interactions between the mystery helix and PmoC as well as between PmoC and PmoA.[62]

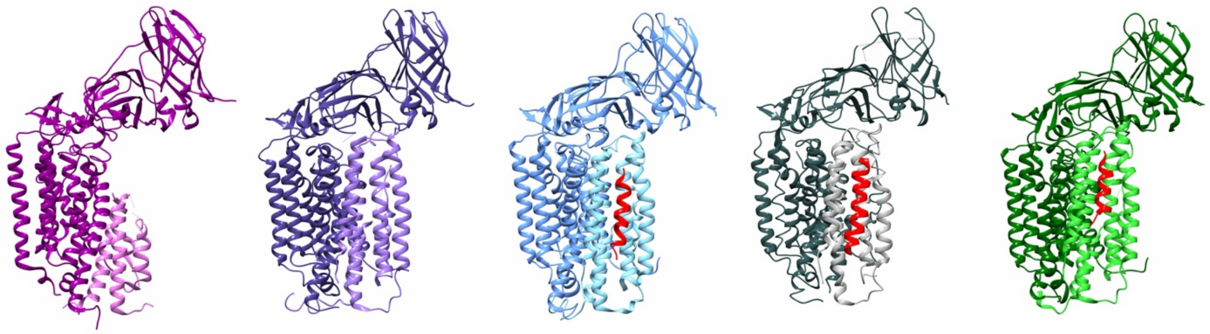

Figure 1.2. One protomer from each crystal structures of pMMO with the PmoC subunit highlighted. From left to right: *Mtm. alcaliphilum* comb. nov. 20Z (PDB code: 6CXH),[63] *Mcc. capsulatus* (Bath) (PDB code: 3RGB),[59] *Mc*. sp. str. Rockwell (PDB code: 4PHZ),[62] *Ms. trichosporium* OB3b (PDB code: 3CHX),[65] and *Mc*. sp. str. M (PDB code: 3RFR).[61] The mystery helix in structures of pMMO from alphaproteobacterial methanotrophs is shown in red. The disorder in PmoC is most pronounced in the *Mtm. alcaliphilum* comb. nov. 20Z pMMO structure. [Adapted from Sirajuddin *et al*.,[62] Lieberman and Rosenzweig,[59] and Ro *et al*.[63]]

An ~30 residue region of the PmoC subunit facing the interior of the trimer is missing in every pMMO structure (Fig. 1.2). This sequence, corresponding to residues 200-223 in *Methylocystis* species strain (*Mc.* sp. str.) Rockwell pMMO,[62] is not observed in the electron density maps and therefore cannot be modeled. Importantly, these residues correspond to the most highly conserved part of the PmoC sequence[66] and contain multiple potential metal-binding residues (Fig. 1.3). In the case of *Methylomicrobium (Mm.) alcaliphilum* comb. nov. 20Z pMMO, 60% of the PmoC subunit could not be modeled (Fig 1.2).[63] The disorder may be related to destabilization and loss of pMMO activity upon detergent solubilization and purification (~100-fold less than in vivo).[31,63] Activity of purified pMMO can be restored or improved by reconstitution into bicelles or nanodiscs,[63] suggesting that structural studies of pMMO in a native-like lipid environment could resolve the nature of this region.

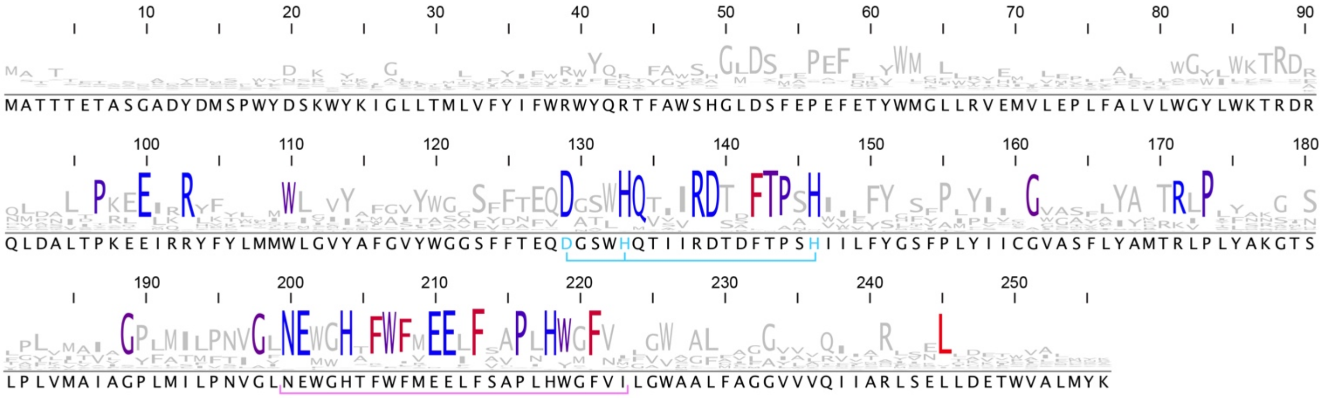

Figure 1.3. Sequence conservation logo for PmoC. The logo was generated from an alignment of 451 representative sequences >170 amino acids in length from PF04896 and TIGR03078 clustered at 100% identity against a hidden Markov model constructed from 132 representative nodes clustered at 50% identity using the EFI-EST webtool.[66] Residues that are conserved in 80% of sequences or more are colored from blue to red in increasing hydrophobicity. The conserved $\mathrm{Cu_C}$-coordinating residues are in cyan while the flexible loop is underlined in pink. The sequence is numbered using the *Mc.* sp. str. Rockwell PmoC numbering (Met49242_1455) and sequences were downloaded from the JGI/IMG database.

1.3.2. Metal binding sites

The pMMO crystal structures reveal up to three copper binding sites per protomer. These sites are referred to as the bis-His site, the Cu_B site, and the Cu_C site (Fig 1.4). The residues coordinating the Cu_B and Cu_C sites are conserved in almost all pMMOs as well as in the homologous enzyme ammonia monooxygenase (AMO) and related hydrocarbon monooxygenases.[67-69] X-ray absorption spectroscopy (XAS), advanced paramagnetic resonance spectroscopies, and mass spectrometry have also been used extensively to probe the pMMO copper centers, with a focus on correlating spectroscopic and crystallographic data.

The bis-His site is located in the soluble region of PmoB between the two cupredoxin domains and coordinated by two histidines, His 48 and His 72 in *Methylococcus (M.) capsulatus* (Bath) pMMO. This site is only occupied in the *M. capsulatus* (Bath) pMMO structure,[59] and His 48 is replaced with asparagine in pMMOs from type II methanotrophs. Notably, the site is also devoid of metal in the *Mm. alcaliphilum* comb. nov. 20Z pMMO structure despite the presence of both histidine ligands.[63] It remains unclear whether the bis-His site is a crystallographic artifact or is biologically relevant, but these observations suggest that it is not essential for methane oxidation. In *M. capsulatus* (Bath) whole-cell EPR studies, a single Cu(II) signal attributable to the Cu_B site is observed,[70,71] indicating that the bis-His site is either unoccupied by copper in vivo or contains Cu(I).

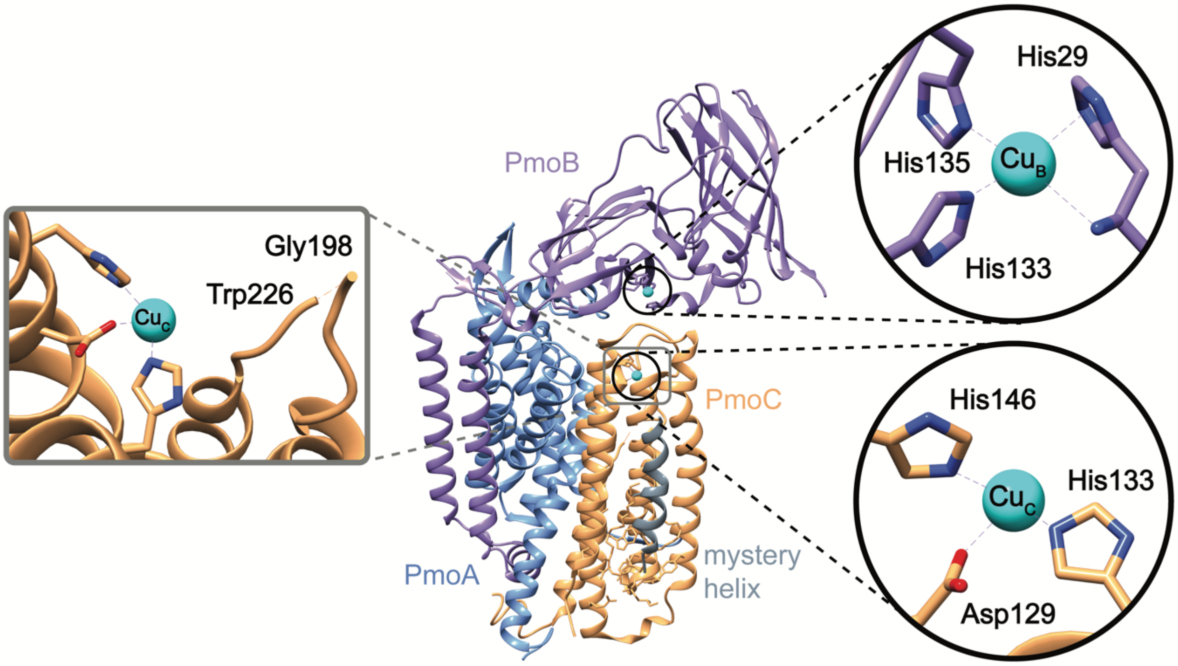

Figure 1.4. Metal-binding sites in *Mc*. sp. str. Rockwell pMMO (PDB code: 4PHZ).[62] Circular cutouts show the Cu$_B$ and Cu$_C$ ligands. Rectangular cutout shows the location of the 27 amino acid disordered region in PmoC and its proximity to Cu$_C$ [Sirajuddin *et al*.[62] Reproduced with permission of American Society for Biochemistry and Molecular Biology.]

The Cu_B site is located in the soluble region of the PmoB subunit, and is occupied by copper in all structurally characterized pMMOs (Fig 1.4).[59-63] Ligands include two histidine side chains derived from an HxH motif and the N-terminal histidine along with its amino group (His29, His 133, and His 135 in *Mc.* sp. Rockwell pMMO) (Fig. 1.5A). These residues are conserved in all pMMOs except those from *Verrucomicrobia*, in which the equivalent residues are methionine, proline, and glycine, which are unlikely to bind metal.[20,47,72] The Cu_B site has been suggested to be analogous to the histidine brace copper active site of lytic polysaccharide monooxygenases (LPMOs) (Fig. 1.5B). However, there are several important differences. First, Cu_B has an additional histidine ligand, of which the coordinating nitrogen occupies the axial bonding position that is open in LPMO.[73,74] Second, the non-amino-terminal histidine ligand in LPMOs coordinates copper with its ε nitrogen atom whereas all the histidines in Cu_B use their δ nitrogen atoms. Third, the LPMO site has a tyrosine side chain oxygen within 2.6 Å of the copper ion while the shortest tyrosine-to-Cu_B distance is 5 Å (Fig. 1.5B). Finally, the coordinating amino group is well ordered in the LPMO structures,[73] but may adopt fluctuating orientations in the Cu_B site as evidenced by poor electron density in every structure.

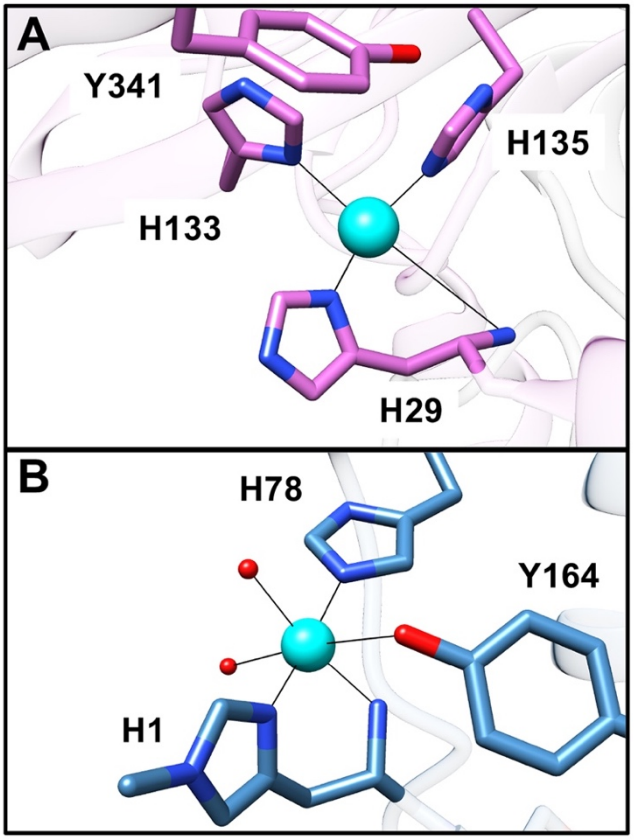

Figure 1.5. Comparison of the pMMO Cu$_B$ site to the active site of LPMO. (A) The *Mc.* sp. str. Rockwell pMMO Cu$_B$ site (PDB accession code 4PI0). The shortest distance from Tyr341 to the copper ion is 5 Å. (B) The *Lentinus similis* LPMO copper active site (PDB accession code 5ACG). Solvent ligands are shown as red spheres. Methylation of the amino-terminal histidine is not a universal feature of LPMO active sites.

The nuclearity of the Cu_B site has been discussed for more than a decade. In the original crystal structure of pMMO from *M. capsulatus* (Bath), it could be modeled with either one or two copper ions, sparking the debate over its nuclearity.[59] The dinuclear model was inspired by extended X-ray absorption fine structure (EXAFS) data indicating the presence of a 2.5-2.6 Å Cu-Cu scattering interaction.[75,76] However, a computational study using quantum methods to further refine the original structure indicated that monocopper is favored at this site,[77] consistent with later and higher quality crystal structures also showing a mononuclear Cu_B site.[61-63]

Additional strong support for this model comes from a recent electron paramagnetic resonance (EPR) study of *M. capsulatus* (Bath) whole cells.[71] A single signal was observed for $^{15}N/^{63}Cu$ labeled cells with ^{15}N hyperfine splitting indicative of four equatorial nitrogen ligands. These ligands were assigned by electron nuclear double resonance (ENDOR) measurements to three histidyl imidazole side chains, a ligand assemblage only possible in the Cu_B site. Thus, not only is Cu_B mononuclear, but these data confirm that the structures recapitulate pMMO in the cell and are biologically relevant. The EPR data indicate that Cu_B is unchanged upon purification, and ^{17}O ENDOR of samples incubated with $H_2{}^{17}O$ revealed the presence of an axial $H_x{}^{17}O$ ligand not resolved in the crystal structures, of which the highest resolution is 2.68 Å.[62] The Cu_B site is therefore best described as a mononuclear Cu(II) site with square pyramidal geometry. These results are corroborated by recent native top-down mass spectrometric (nTDMS) analysis of purified pMMO reconstituted into nanodiscs, which clearly showed the presence of a single copper ion in PmoB.[78] Nevertheless, the source of the EXAFS Fourier transform feature that was fit as a Cu-Cu interaction remains unclear and must be reinvestigated in order to fully reconcile all the data.

The Cu_C site, which is conserved in all pMMOs, is located within the transmembrane domain of the PmoC subunit and includes two histidines and an aspartic acid as ligands (Asp 129, His 133, and His 146 in *Mc.* sp. str. Rockwell pMMO[62]) (Fig. 1.6). If pMMO is crystallized in zinc-containing buffer or if zinc is soaked into the crystals, zinc is present in this site.[59,61,62] In the absence of zinc, the site is occupied by copper,[60,62] and the occupancy can be increased by soaking in extra copper.[62] An EPR signal observed in purified pMMO samples has been assigned to the Cu_C site on the basis of Cu-Cu distances obtained from double electron-electron resonance (DEER) measurements.[71] The signal is not observed in whole cells, presumably because the Cu_C site is Cu(I) in vivo. Since the EPR signal assigned to the Cu_C site overlaps with that of the Cu_B site, its coordination environment is less readily determined. However, ^{15}N ENDOR is consistent with histidine ligation and ^{1}H and ^{17}O ENDOR indicate the presence of a solvent ligand.[71] nTDMS analysis of pMMO in nanodiscs also indicates binding of a single copper ion to the PmoC subunit, and copper supplementation during nanodisc formation increases the copper occupancy of PmoC.[78] Fragmentation data localizing the bound copper ion to the crystallographically-observed Cu_C site could not be obtained, however.

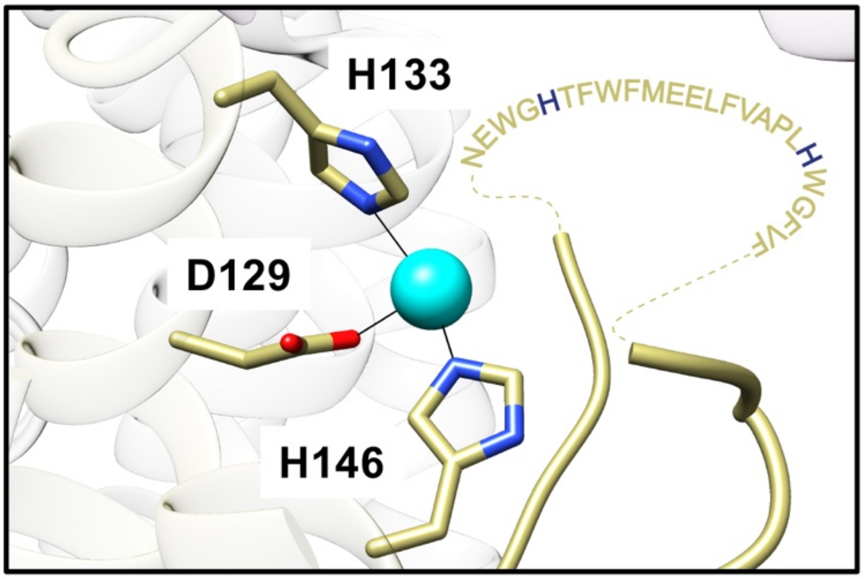

Figure 1.6. The *Mc.* sp. str. Rockwell pMMO Cu$_C$ site (PDB accession code 4PI0). The unmodeled highly conserved region spanning residues 200-223 is shown as amino acid one-letter codes connected to the model by dashed lines. Potential metal binding residues include two strictly conserved histidines highlighted in blue.

While the advanced paramagnetic resonance analysis is consistent with the crystallographic model for the Cu_C site, the coordination is not a foregone conclusion. This site directly abuts the unmodeled, highly conserved region of the PmoC subunit (Figs. 1.4, 1.6),[59-62] and is not even visible in the *Mm. alcaliphilum* comb. nov. 20Z pMMO structure (Fig 1.2).[63] Weak density suggestive of a fourth ligand has been modeled as a water molecule in the *Mc.* sp. str. M[61] and *Mc.* sp. str. Rockwell pMMO structures, while soaking *Mc.* sp. str. Rockwell pMMO crystals in zinc led to ordering of 10 additional residues and modeling of a glutamic acid ligand not observed in the structures with copper.[62] Given the striking conservation of this region and the presence of potential metal-binding residues, it is imperative to determine its structure. It remains possible that the Cu_C EPR signal derives from a copper site that has not yet been structurally unveiled.

1.3.3. Identity of the active site

The location and molecular details of the pMMO active site represent one of the most important outstanding questions in biological methane activation. Methane oxidation assays using samples of pMMO demetallated and inactivated by cyanide treatment indicate that 2-3 copper ions are required for activity. Addition of excess copper inhibits activity, albeit in a reversible fashion.[46,62] While a diiron center was once proposed to be the pMMO active site,[39] there is no iron in the structures and only copper has been linked to activity. Of the crystallographically-observed copper sites, the bis-His site has been discounted because the coordinating residues are not conserved and the site is only occupied in one crystal structure.[59]

Instead, the Cu_B site has been the focus of most discussion. Computational studies have suggested that both a dinuclear[79-81] and a mononuclear[77] copper site at this location would be capable of methane oxidation. The possibility of a Cu_B active site was investigated using recombinantly expressed proteins that contain the two PmoB cupredoxin domains, form a Cu_B site similar to that in native pMMO by EPR,[71] and convert methane to methanol.[46,71] However, extensive evaluation of these proteins revealed that the methanol is not produced by their Cu_B-like site, and likely involves adventitious chemistry from the reduction of dioxygen by duroquinol, which is used as a reductant in pMMO activity assays.[71] As such, the basis for recently reported enzymatic activity of pMMO mimetics utilizing the PmoB soluble domains tethered to apo ferritin[82] is unclear. The argument for a Cu_B active site is further diminished by the replacement of the three Cu_B-coordinating histidines in the verrucomicrobial PmoB sequences with methionine, proline, and glycine.[29,47,48]

In the absence of evidence for Cu_B being the site of methane activation, attention has turned toward the Cu_C site. Two recent experimental findings are consistent with a Cu_C active site. First, nitrite, a known inhibitor of methane oxidation,[83,84] perturbs the Cu_C EPR signal, and ^{15}N ENDOR upon the addition of ^{15}N-nitrite is consistent with NO_2^- binding to Cu(II) via the oxygen atom(s).[71] Second, an increase in the copper occupancy of PmoC detected by nTDMS was correlated with increased pMMO activity.[78] These combined data suggest that copper in PmoC, regardless of whether it is located at the crystallographic Cu_C site, is the site of methane oxidation. In support of this model, mutation of the Cu_C site in a homologous hydrocarbon monooxygenase completely abrogated activity whereas mutation of the Cu_B site reduced activity, but maintained affinity for alkane substrate.[68,85] Finally, the Cu_C ligands along with the neighboring disordered region of PmoC are conserved in all pMMOs, including those from *Verrucomicrobia*.[29,47,48] This observation underscores the potential importance of the Cu_C site, but characterization of the verrucomicrobial pMMOs is imperative. *Verrucomicrobia* grow at high temperatures and low pH, conditions that may affect the structure and metal binding properties of pMMO.

1.3.4. Protein partners

Another unresolved issue regarding pMMO is the potential existence of larger protein complexes containing pMMO or transient protein-protein interactions between pMMO and partners. Whereas catalysis by sMMO requires interaction of the hydroxylase component (MMOH) with a reductase (MMOR) and a regulatory protein (MMOB) (vide infra),[32] pMMO activity can be obtained in vitro by addition of the reductants NADH and duroquinol to membrane-bound and detergent-solubilized samples, respectively.[86,87] Duroquinol is believed to mimic a native quinol present in the membranes, presumably ubiquinol, which directly reduces pMMO. NADH is thought to reduce the native quinol via a type 2 NADH:quinone oxidoreductase (NDH-2) that has been observed to copurify with pMMO,[38,88,89] although there is no evidence for direct interactions between pMMO and NDH-2. Reduction of pMMO by quinols using this pathway has been referred to as the "redox-arm mode" of electron delivery.[90]

Electron delivery to pMMO has also been proposed to occur via methanol oxidation to formaldehyde by MDH.[91] In this "direct coupling mode," electrons are funneled to pMMO through the cytochrome *c* electron acceptor of MDH. Support for both the redox arm and direct coupling models as well as a combination thereof, "uphill electron transfer," has been obtained from genome-wide metabolic modeling for several methanotrophs.[90,92-96] Direct coupling would be facilitated by complexation with MDH, allowing direct transfer of methanol from pMMO to the MDH active site, and a pMMO-MDH complex has been proposed on the basis of low resolution cryoelectron microscopy studies.[97] While this complex has not been isolated biochemically, transient interactions between several pMMOs and their cognate MDHs have been detected.[98,99] How the MDH dimer (Fig. 1.7A) interacts with the pMMO trimer is not clear. Resolving the nature of pMMO's interaction with electron donor proteins is an important goal for future studies.

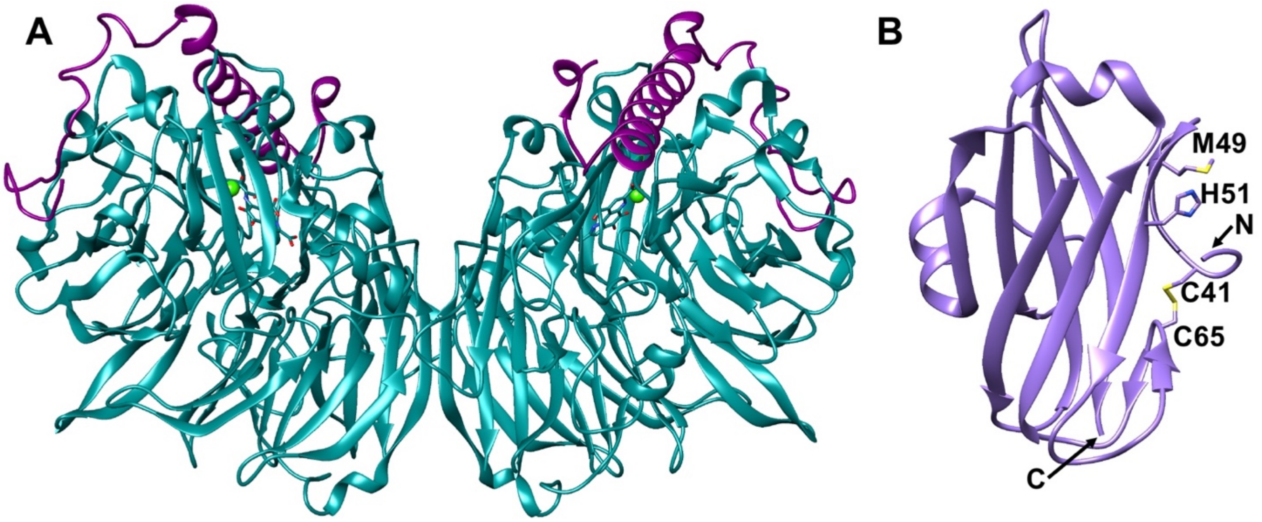

Figure 1.7. Potential protein interaction partners of pMMO. (A) *M. capsulatus* (Bath) MDH (PDB accession code 4TQO). The α subunits are shown in teal and the β subunits are shown in violet. The pyrroloquinoline quinone (PQQ)/calcium ion cofactor is shown as sticks and a green sphere. (B) The periplasmic domain of PmoD from *Mc.* sp. str. Rockwell (PDB accession code 6CPD). Conserved residues involved in formation of a Cu_A-like site between two monomers are highlighted. In this structure, the two conserved cysteines form a disulfide bond. A predicted transmembrane helix at the C-terminus is not present in this structure.

Finally, the loss of pMMO activity upon solubilization and purification may be due in part to separation from other protein components necessary for stabilization, copper loading, and delivery of electrons and/or protons. Recent work has suggested that the PmoD protein, found exclusively in methane- and ammonia-oxidizing bacteria and sometimes encoded within the same operon as the pMMO subunits, is one such component.[100] Genetic disruption experiments in *Methylosinus* (*Ms.*) *trichosporium* OB3b indicate that PmoD is important for growth under pMMO-utilizing conditions. PmoD consists of a cupredoxin-like periplasmic domain (Fig. 1.7B)

1.4. Soluble methane monooxygenase

1.4.1 Overall structure

While most methanotrophs rely solely on pMMO for methane oxidation, some have the ability to express sMMO under copper-starvation conditions.[11,37,40] sMMO consists of multiple proteins encoded within the *mmoXYBZDC* operon.[101] The *mmoX, mmoY, and mmoZ* genes encode the α, β, and γ subunits of the hydroxylase component (MMOH), which houses a nonheme diiron active site. The *mmoB* gene encodes the regulatory protein, MMOB, and *mmoC* encodes the reductase, MMOR, which reduces the diiron site via NADH and contains FAD and a [2Fe-2S] cluster as cofactors. MMOB increases the reaction rate of MMOH with dioxygen by 1000-fold.[102,103] MMOD is not necessary for sMMO function and instead has an inhibitory effect on activity.[104,105] Like pMMO, MMOH must be isolated from the native organism for biochemical studies, but MMOB, MMOR, and MMOD can be expressed in *E. coli*.

sMMO systems from *M. capsulatus* (Bath) and *Ms. trichosporium* OB3b have been structurally characterized. MMOH is a dimer comprising the three subunits in an $(\alpha\beta\gamma)_2$ arrangement (Fig. 1.8A).[106,107] The diiron active site, housed within a four-helix bundle, is coordinated by two histidine and four carboxylate ligands from the α subunit (Glu 114, His 147 to Fe1, Glu 209, Glu 243, His 246 to Fe2, Glu 144 bridging). In the resting Fe(III)Fe(III) state, the iron-ions are bridged by two hydroxo groups (Fig. 1.9A). Upon reduction to the Fe(II)Fe(II) state, Glu243 displaces a bridging hydroxo group, bridging the two irons, while coordinating Fe2 in a bidentate fashion (Fig. 1.9B).[108,109] A number of MMOH structures have been determined in the presence of hydrocarbon substrate and product analogs, xenon gas, and different metal ions.[31] The MMOB and MMOC structures have been determined by NMR, with the [2Fe-2S] and FAD/NADH domains of MMOC characterized separately.[110-113]

In addition, crystal structures of MMOH in complex with MMOB[109,114] and in complex with MMOD[115] have been reported. Both MMOB and MMOD bind symmetrically to MMOH, with one molecule interacting with each αβγ protomer (Figs. 1.8B,C). Upon binding to MMOH, primarily to the α subunit, MMOB's flexible N-terminal tail of ~35 residues forms a ring-like structure on the MMOH surface. The C-terminal region of MMOB becomes ordered as well. Several MMOH helices are reorganized, and the resultant side chain rearrangements directly affect the active site.[109,114] In the initial *M. capsulatus* (Bath) MMOH-MMOB structure, Glu 243 shifts to its reduced conformation,[114] but this change is not observed in a recent X-ray free electron laser (XFEL) structure of *Ms. trichosporium* MMOH-MMOB determined at room temperature, suggesting that photoreduction, rather than MMOB binding, caused the shift.[109] The binding site for MMOD, as observed in the *Ms. sporium* strain 5 MMOH-MMOD complex structure, overlaps with that of MMOB. MMOD disrupts the N-terminus of the β subunit, which wraps around the α subunit in each protomer, and affects Fe1, causing dissociation of His147 and a shift of Glu 114 to bidentate.[115]

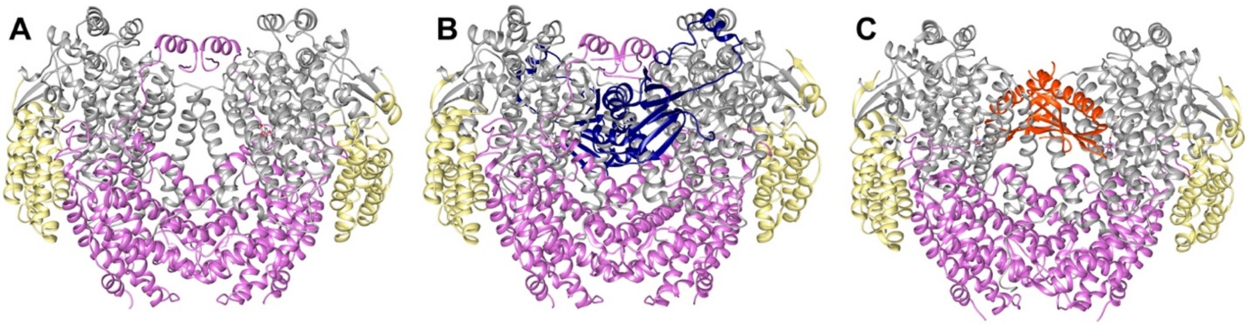

Figure 1.8. Structures of sMMO. (A) *M. capsulatus* (Bath) MMOH (PDB accession code 1MTY). The α subunits are shown in gray, the β subunits are shown in pink, and the γ subunits are shown in yellow. The iron ions are shown as orange spheres with the ligands shown as sticks. (B) *M. capsulatus* (Bath) MMOH-MMOB complex (PDB accession code 4GAM). MMOB is shown in dark blue. (C) *M. sporium* strain 5 MMOH-MMOD complex (PDB accession code 6D7K). MMOD is shown in orange.

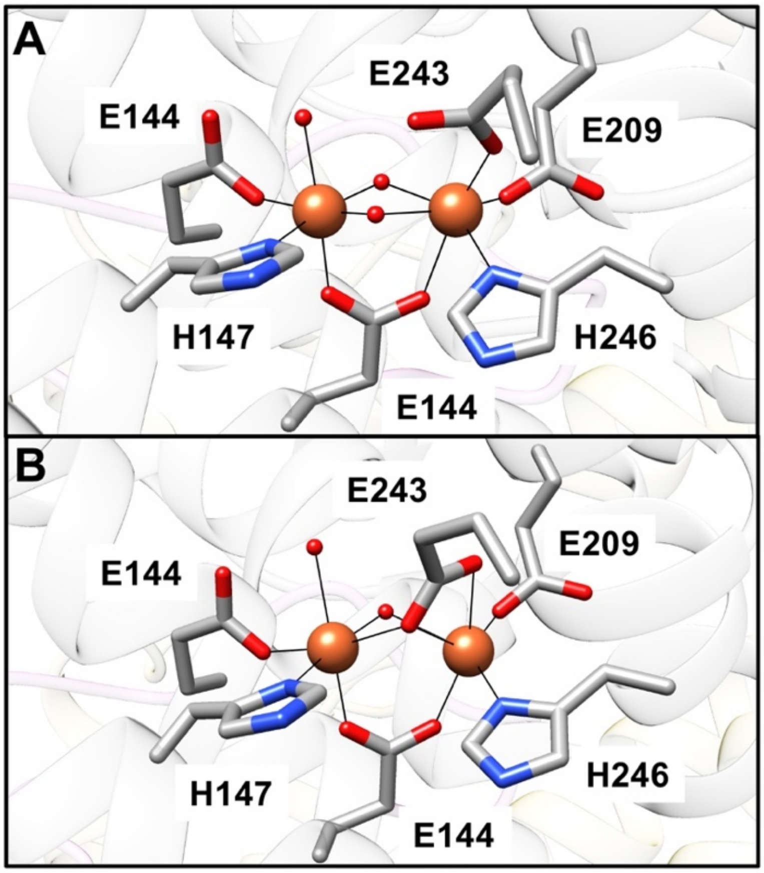

Figure 1.9. The sMMO active site. (A) The Fe(III)Fe(III) site in *M. capsulatus* (Bath) $\mathrm{MMOH_{ox}}$ (PDB accession code 1MTY). (B) The Fe(II)Fe(II) site in *M. capsulatus* (Bath) $\mathrm{MMOH_{red}}$ (PDB accession code 1FYZ). Iron ions are shown as orange spheres and solvent ligands are shown as red spheres.

There is no structure of the MMOH-MMOR complex, but the MMOR binding site mapped by hydrogen-deuterium exchange, chemical crosslinking, and computational docking[116-119] overlaps with that of MMOB. Overlapping sites are consistent with inhibition of MMOR binding by MMOB,[114,120] and suggest a model in which MMOR and MMOB compete for binding to MMOH, although an MMOH-MMOB-MMOR ternary complex has been detected.[118] In this model, MMOR binds first and reduces the diiron site, which causes MMOR to lose affinity for MMOH and be replaced by MMOB. Reduced MMOH ($\mathrm{MMOH_{red}}$) has higher affinity for MMOB and binding of MMOB allows formation of reactive intermediates and substrate oxidation. MMOB is then released followed by product egress from the active site. It is possible that MMOB dissociates entirely or remains tethered with its N-terminal ring region to allow the cycle to begin again with MMOR binding.[116] However, this model is not compatible with the observation that MMOB decreases the redox potential of MMOH,[121,122] necessitating that it bind oxidized MMOH ($\mathrm{MMOH_{ox}}$) with a higher affinity than $\mathrm{MMOH_{red}}$. In addition, fluorescence titrations using labeled MMOB indicate a higher affinity for $\mathrm{MMOH_{ox}}$ than $\mathrm{MMO_{red}}$.[123] These discrepancies have been suggested to derive from hysteretic effects on the redox potential.[32]

1.4.2. Pores and cavities

While the most intense discussions surrounding pMMO structure have focused on the metal centers and their possible roles in catalysis, the diiron active site of sMMO has been well established for >30 years.[124,125] Ongoing debate has instead focused on substrate specificity and access to the active site and the role of MMOB therein. Access to the active site has been considered in the context of three distinct cavities observed in the MMOH crystal structures. The first cavity contains the diiron active site, is ~12 Å from the bulk solvent, and is connected via a pore to the surface of the enzyme. This pore is gated by residues Thr 213, Asn 214, and Glu 240.[126] The second cavity is adjacent to the first, but blocked by residues Phe 188 and Leu 110 in structures of MMOH alone. This cavity is connected to a third large cavity, and all three cavities have been shown to bind halogenated alkanes and xenon gas, suggesting that they form routes for methane, dioxygen, and product access.[127,128]

Crystal structures of MMOH-MMOB revealed shifts in residues gating the pore and cavities. Upon MMOB binding, new interactions involving MMOH residues Ser 111, Asn 214, Thr 213, and Glu 240 close the pore. In the original *M. capsulatus* (Bath) MMOH-MMOB structure, shifts in residues Phe 188 and Leu 110 connect the first and second cavities, and were proposed to allow methane and dioxygen to access the reduced diiron site.[114] However, kinetic data are not consistent with methane traversing 35-40 Å in cavities prior to reaction at the active site.[32,129,130] Moreover, in recent high resolution structures of the *Ms. trichosporium* OB3b MMOH-MMOB complex, the shift in Phe 188 is only observed upon binding of bulky substrates. The cavities remain separated in $MMOH_{red}$ as well as in the XFEL structures of $MMOH_{ox}$-MMOB and $MMOH_{red}$-MMOB, suggesting that MMOB may actually serve to close, rather than open, this bottleneck.[131] An alternative path, designated the W308-tunnel, has been detected using a probe with solvent radius 1.1 Å instead of the previously used water solvent radius of 1.4 Å. This tunnel, gated by Trp 308 and Pro 215 (Fig. 1.10), is lined with highly conserved hydrophobic residues, and is open in the $MMOH_{red}$-MMOB structure. The use of this narrow tunnel is more consistent with the accumulated kinetic data, and variants of MMOB designed to block this tunnel significantly affect the rate of diiron active site oxidation, supporting its role in dioxygen access.[131]

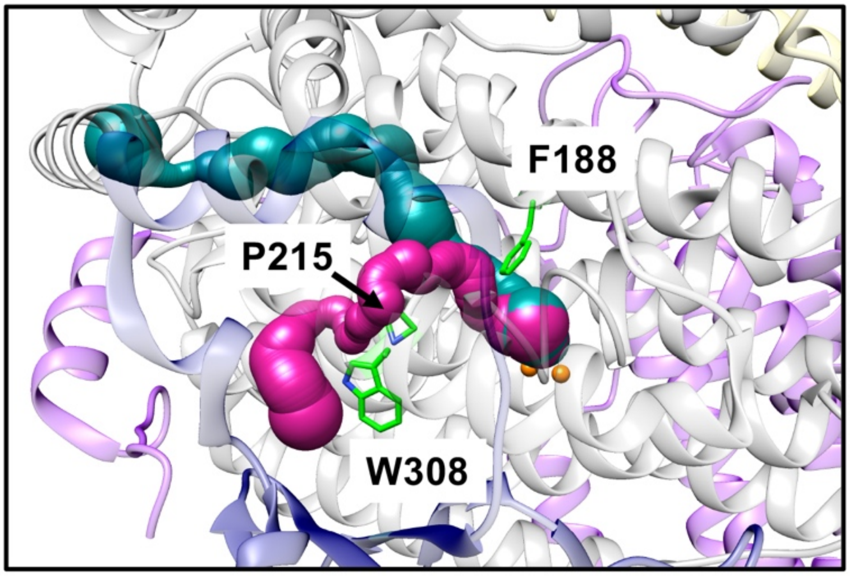

Figure 1.10. Cavities and tunnels in the *Ms. trichosporium* OB3b MMOH$_{\text{red}}$-MMOB XFEL structure (PDB accession code 6YDI). The α subunits are shown in gray, the β subunits are shown in pink, the γ subunits are shown in yellow, and MMOB is shown in dark blue. The W308 tunnel is shown in magenta and the previously identified chain of cavities is shown in teal. Key gating residues are highlighted in green sticks.

1.4.3. Dioxygen and methane activation

In contrast to pMMO, the mechanisms of dioxygen and methane activation by sMMO have been studied in detail. The catalytic cycle of MMOH in the presence of MMOB has been probed extensively by single-turnover kinetics and spectroscopy using chemical reductants, and has been recently reviewed elsewhere.[32,132] In brief, reaction of $MMOH_{red}$ with dioxygen yields intermediate O,[102,103,133] an Fe(II)Fe(II) species that converts sequentially to intermediates P*, P, and Q.[102,134-136] Intermediate P* is also an Fe(II)Fe(II) species,[136] while P is an Fe(III)Fe(III) peroxo species,[134,135] the exact structure of which remains unclear.[32] As the species that reacts with methane, intermediate Q has been the subject of much discussion. Two antiferromagnetically coupled high-spin Fe(IV) ions are present,[137-139] but the geometry remains under debate, with evidence supporting both diamond and open core geometries.[139-143] Once Q reacts with methane, intermediate T is formed, followed by methanol release and return to $MMOH_{ox}$.[139]

The mechanism of methane activation by Q has also been investigated extensively, both computationally[144,145] and experimentally. Experimental approaches have leveraged sMMO's wide substrate range (cyclic hydrocarbons and cubanes, linear alkanes C1-C8)[146-148] to assess reactions with chiral[149,150] and radical clock[151-154] substrates, which provide insight into the possible existence of radical intermediates. These studies are consistent with a hydrogen abstraction mechanism,[32] but are complicated by the use of nonnatural substrates. Notably, studies using deuterated methane revealed a remarkable kinetic isotope effect (KIE) of 50, which is not observed with other substrates[155,156] and is suggestive of hydrogen tunneling. Conformational changes upon MMOB binding have been proposed to selectively guide methane to the active site in such a way as to optimize tunneling.[32]

1.5. Protein engineering

Many of the unresolved questions surrounding both MMOs could be addressed by site-directed mutagenesis. For pMMO, mutation of the residues coordinating the crystallographically-observed metal centers would go a long way toward establishing functional relevance as would alteration of the highly conserved part of PmoC that is not observed crystallographically. Substrate specificity and mechanistic studies would also be facilitated. For sMMO, the ability to heterologously generate MMOB variants has helped detect intermediates[130] and has provided insight into control of substrate access to intermediate Q,[129,130,156] but the roles of the different cavities and channels can only be probed in a systematic fashion by using MMOH variants. Moreover, commercially viable biological methane activation may require engineering of either MMO to have increased methane oxidation rates,[8] which would be more feasible in a heterologous expression system.

However, attempts at heterologous expression of MMOH or pMMO have been largely unsuccessful. Recombinant versions of the PmoB subunit recapitulate some of the spectroscopic properties of pMMO, but are unstable in the absence of fusion proteins and are not catalytically active.[46,71] The N-terminal cupredoxin domain of the homologous AmoB subunit from *Nitrosocaldus yellowstonii*, which lacks the C-terminal cupredoxin domain, has been recombinantly expressed and crystallographically characterized, but does not exhibit methane oxidation activity.[69] Expression of intact pMMO has been reported in *Rhodococcus erythropolis* LSSE8-1, albeit with whole cell activity 340 times less than that of *Ms. trichosporium* OB3b.[8,45] Besides likely issues involving insertion of the pMMO subunits into the membrane and proper trimer assembly, an obstacle specific to expression of functional pMMO may be the lack of ICMs in heterologous hosts. In most methanotrophs, pMMO is localized to these intracellular structures,[17,37,40,157] which could play a role in structuring the enzyme or concentrating methane.[8] The presence of ICMs and the location of pMMO in the verrucomicrobial methanotrophs remain unclear, however.[22]

While enzymes related to MMOH such as toluene and phenol hydroxylases have been expressed in *E. coli*,[158,159] the only reported heterologous expression of MMOH is in *Pseudomonas,* although methane oxidation by these strains has not been reported.[43] Neither this system nor the pMMO *Rhodococcus erythropolis* LSSE8-1 expression system[45] resulted in the ability to generate variants or isolate recombinant MMOs for further study. As an alternative approach, *Ms. trichosporium* OB3b MMOH genes with mutations of interest have been reintroduced into a *Ms. trichosporium* OB3b strain with the *smmo* operon partially deleted. This strain can be grown using pMMO, with expression of the variant MMOHs occurring as copper levels decline.[160,161] Several variants have been studied using this method, primarily focusing on residues in the α subunit surrounding the diiron center.[161-163] However, this system requires optimization to be practical for generation of large numbers of variants for protein purification and characterization.

An analogous strategy for pMMO is more complicated because most methanotroph genomes contains multiple copies of the *pmo* operon. Genetic tools have been developed for the methanotroph *Methylotuvimicrobium buryatense* 5GB1C (formerly *Methylomicrobium buryatense* 5GB1C[164]),[165,166] which has been used for metabolic engineering[16] and only contains one copy of the pMMO genes. In principle, it should be possible to obtain point mutants of pMMO using these tools and growing under sMMO-producing conditions to mitigate any growth defects from an impaired pMMO. However, such attempts have not been successful, perhaps because for unknown reasons, pMMO remains important for cell growth under sMMO-producing conditions.

This notion is consistent with the observation that pMMO is still expressed under conditions of copper starvation and only mildly upregulated when copper is available.[42] CRISPR-Cas9, which has been developed for methanotrophs, presents another potential route to variants, but the current method has very low editing efficiency and has not yet been demonstrated to be effective for this purpose.[167]

1.6. Conclusions

The unique lifestyle of methanotrophs presents intriguing possibilities for methane utilization and bioremediation. Their wide variety of habitats highlights the effectiveness of the MMO-based carbon assimilation strategy. For pMMO, progress has been made in understanding the nuclearity of the Cu_B site and the importance of the Cu_C site. Further studies of pMMO in a lipid environment and of the verrucomicrobial pMMOs promise to shed light on the active site location and structure, bringing the field closer to determining the reaction mechanism. Beyond the pMMO trimer itself, the possibilities of PmoD and MDH as interaction partners represent an important future direction. For sMMO, new structures of MMOH complexes, some determined using an XFEL, have revealed in detail the effects of MMOB and MMOD on MMOH structure and have delineated new pathways for substrate access to the diiron active site. The geometry of intermediate Q, the relative importance of different cavities in the MMOH structures, and the sequence of events involving MMOB and MMOR binding require additional studies. Studies of both MMOs await development of effective heterologous expression systems, which could be used to generate variants and as a platform for protein engineering. The combination of detailed chemical understanding and protein engineering could finally realize the potential of methanotrophs to add value[14] and even help save the planet.

CHAPTER 2: Recovery of particulate methane monooxygenase structure and activity in a lipid bilayer

A previous version of this chapter was published as:

C. W. Koo, F. J. Tucci, Y. He, A. C. Rosenzweig, *Science* (2022)

2.1. Abstract

Bacterial methane oxidation using the enzyme particulate methane monooxygenase (pMMO) contributes to removal of environmental methane, a potent greenhouse gas. Crystal structures determined using inactive, detergent-solubilized pMMO lack several highly conserved regions neighboring the proposed active site. We show that reconstituting pMMO in nanodiscs with lipids extracted from the native organism restores methane oxidation activity. Multiple nanodisc-embedded pMMO structures determined by cryoelectron microscopy to 2.14-2.46 Å resolution reveal the structure of pMMO in a lipid environment. The resulting model includes stabilizing lipids, regions of the PmoA and PmoC subunits not observed in prior structures, and a previously undetected copper binding site in the PmoC subunit with an adjacent hydrophobic cavity. These structures provide a revised framework for understanding and engineering pMMO function.

2.2. Introduction

Methane, a potent greenhouse gas, is a major contributor to the current climate crisis.[168,169] Methane-oxidizing (methanotrophic) bacteria not only consume ~30 million tons of atmospheric methane per year,[170] but also have biotechnological potential to convert this cheap and abundant feedstock to fuels and value-added chemicals.[171] Although methanotrophs have been engineered to produce a range of products, low yields and conversion efficiencies have precluded economic viability.[172] For methane bioconversion to be transformative, the initial step, oxidation of methane to methanol, must be optimized, which requires molecular-level understanding of the main enzyme responsible, particulate methane monooxygenase (pMMO).[30,173]

pMMO is a membrane-bound, copper-dependent enzyme comprising three subunits, PmoA (β), PmoB (α) and PmoC (γ), arranged as a trimer of αβγ protomers. The crystal structures of detergent-solubilized pMMO from multiple methanotrophic species[59,61-63,65] have revealed the presence of three copper-binding sites. The ligands to two monocopper sites located in PmoB, the bis-His site and the Cu_B site, are not conserved, with the bis-His site only present in pMMOs of Gammaproteobacteria and the Cu_B site missing in pMMOs of Verrucomicrobia.[72] By contrast, one aspartic acid and two histidine ligands to the third site, Cu_C, located in PmoC, are strictly conserved. This observation, along with the saturated coordination geometry of the Cu_B site and the correlation of increased methane oxidation activity with copper occupancy of PmoC,[78] suggests that the copper active site is located in PmoC.

However, it remains unclear whether the crystallographic Cu_C site is an appropriate active site model due to several major caveats with the crystal structures. First, pMMO activity decreases upon solubilization in detergent,[31,63] and purified samples exhibit zero methane oxidation activity (Table S2.1), meaning that the structures do not represent the active enzyme. Second, ~25 residues within PmoC are not observed in the electron density maps for any pMMO crystal structure. These residues, which correspond to the most highly conserved part of the PmoC sequence, are predicted to reside adjacent to the Cu_C site facing the interior of the pMMO trimer.[173] The ambiguity in this region has precluded the identification of any potential cavities for methane and oxygen binding. It is likely that both of these limitations, the loss of activity and the disorder in PmoC, are attributable to removal of pMMO from its native membrane environment. Disruption of the lipid bilayer followed by detergent solubilization and multiple purification steps may cause conformational changes and the separation of bound metal and/or lipid cofactors.[174,175]

2.3. Results

2.3.1. Native lipid nanodisc reconstitution

We recently demonstrated that reconstitution of detergent-solubilized pMMO into synthetic lipid bicelles[63] and nanodiscs[78] restores methane oxidation activity (Table S2.1). To prepare enzymatically active samples for structure determination by cryoelectron microscopy (cryoEM), *Methylococcus* (*M.*) *capsulatus* (Bath) pMMO was solubilized in n-dodecyl-β-D-maltoside (DDM) and embedded into nanodiscs using the membrane scaffold protein MSP1E3D1 and the commonly used lipids 1,2-dimyristoyl-sn-glycero-3-phosphocholine (DMPC) and 1-palmitoyl-2-oleoylphosphatidylcholine (POPC).[176] To more closely mimic the cellular environment of pMMO, native lipids were extracted from *M. capsulatus* (Bath).[177,178] and also used for nanodisc reconstitution. Nanodisc formation and pMMO incorporation were confirmed by negative stain EM and cryoEM (Fig. 2.1).

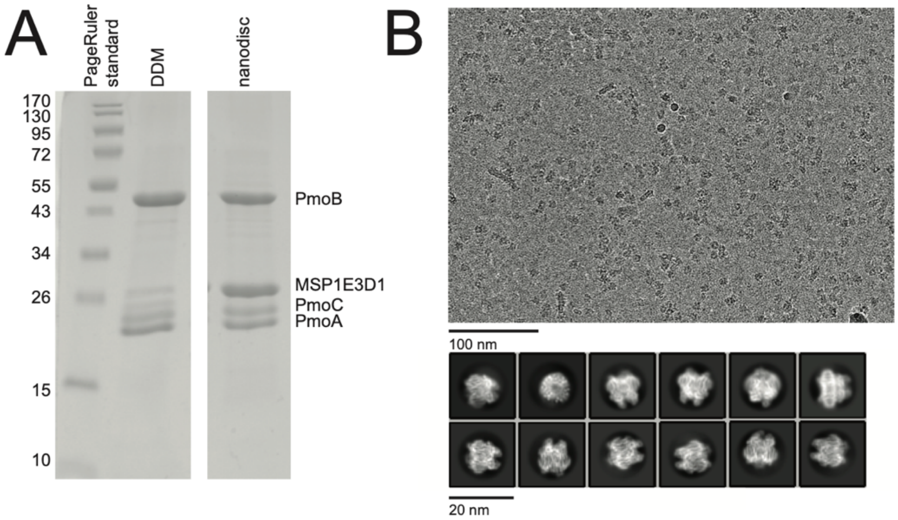

Figure 2.1. Reconstitution of pMMO into lipid nanodiscs. (**A**) SDS-PAGE gel with bands corresponding to subunits PmoA, PmoB, PmoC, and the membrane scaffold protein MSP1E3D1. The lane labeled DDM contains DDM-solubilized pMMO before mixing with MSP1E3D1. Lanes are from the same gel with intermediate lanes removed for simplicity. (**B**) CryoEM micrograph showing pMMO nanodiscs and the corresponding 2D class averages.

As observed previously for *Methylocystis* (*Mc.*) species (sp.) strain (str.) Rockwell pMMO,[78] addition of copper during nanodisc reconstitution was necessary to recover methane oxidation activity. Nanodiscs formed with 3 molar equivalents of $CuSO_4$ and the native lipids exhibited the most activity, followed by POPC and DMPC nanodiscs (Fig. 2.2A, fig. S2.1). The copper content also increases slightly in the native and POPC nanodiscs (fig. S2.2). The looser packing afforded by the unsaturated bond in the acyl tails of POPC[63] and the native lipids (vide infra) may facilitate loading of individual copper sites as well as access of the reductant used in the activity assays, duroquinol, to the active site. The observed turnover frequency of 0.012 s^{-1} represents a substantial improvement over the zero activity DDM/Cymal-5 samples used for previous structural studies and is comparable to *M. capsulatus* (Bath) membrane-bound pMMO activity measured with duroquinol (0.026-0.042 s^{-1}) (Table S2.1). Importantly, duroquinol is a synthetic analog of endogenous quinols[89] and is not the physiological reductant as claimed recently.[179] In vivo electron delivery has been proposed to occur via ubiquinol reduced by a type 2 NADH:oxidoreductase and/or by coupling to methanol oxidation by methanol dehydrogenase (MDH).[173] The absence of these potential redox partners may be what precludes attaining whole-cell activity using isolated pMMO. Moreover, negative-stain images of *M. capsulatus* (Bath) membranes show dense packing of pMMO trimers (fig. S2.3), an environment that may contribute to increased activity in the membrane and that cannot be recapitulated in a single particle study.

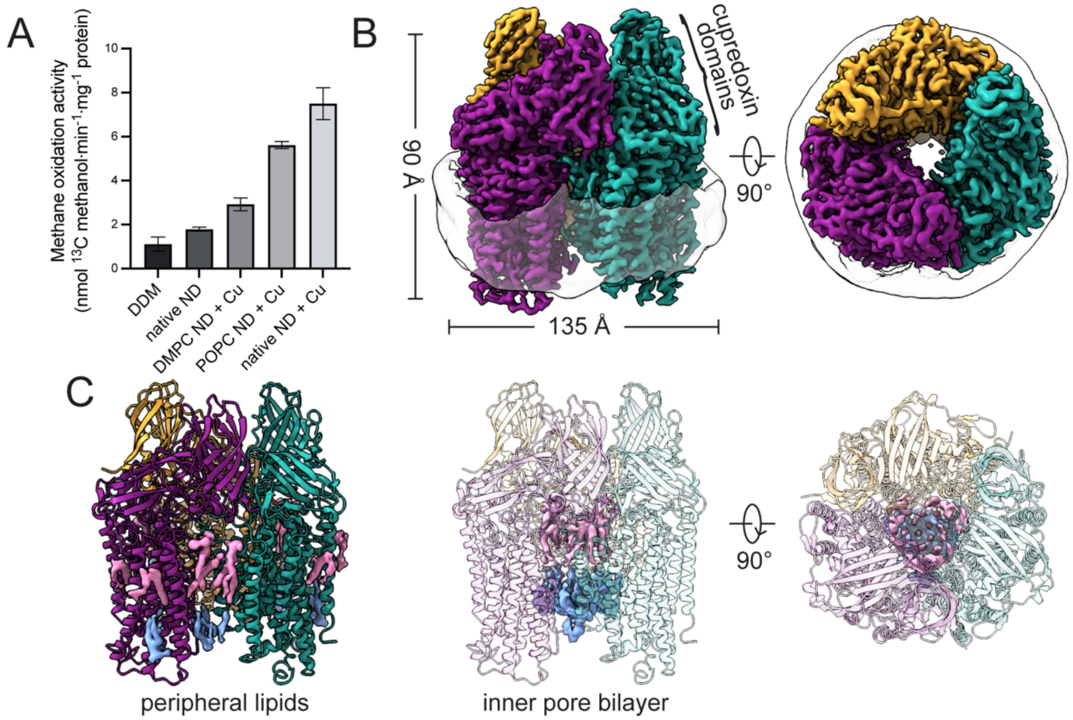

Figure 2.2. Structural characterization of *M. capsulatus* (Bath) pMMO in a native lipid nanodisc. (**A**) Methane oxidation activity of cryoEM samples. Addition of 3 equivalents of $CuSO_4$ during nanodisc (ND) reconstitution (+ Cu) improved activity. Error bars represent standard deviation of $n \geq 3$ biological replicates, each measured in triplicate. (**B**) CryoEM map (dataset MC01) showing the trimer and the encircling nanodisc. Symmetrical αβγ protomers are colored in purple, teal, and gold. (**C**) Model of pMMO showing the map for lipids on the periphery and in the inner pore of the enzyme. The periplasmic and cytoplasmic leaflets are colored in pink and blue, respectively.

2.3.2. Overall cryoEM structures of pMMO in a lipid bilayer

Six cryoEM maps of nanodisc-embedded pMMO from three different methanotrophs were obtained to 2.14-2.46 Å resolution (figs. S2.4 and S2.5, Table S2.2), providing the first structures of pMMO in a lipid environment. The highest resolution map is that of enzymatically active *M. capsulatus* (Bath) pMMO in native lipid nanodiscs, resolved to 2.14 Å (MC01, Table S2.2, Fig. 2.2B), considerably higher resolution than the *M. capsulatus* (Bath) (2.8 Å),[59] *Mc.* sp. str. Rockwell (2.6 Å),[62] and *Methylotuvimicrobium (Mt.) alcaliphilum* comb. nov. 20Z (2.7 Å)[63] pMMO crystal structures. The overall architecture agrees with the crystal structures, consisting of a trimer of αβγ protomers within the nanodisc belt (Fig. 2.2B). Densities corresponding to solvent molecules and phospholipids (Fig. 2.2C, Fig. 2.3) are clearly defined at this resolution.

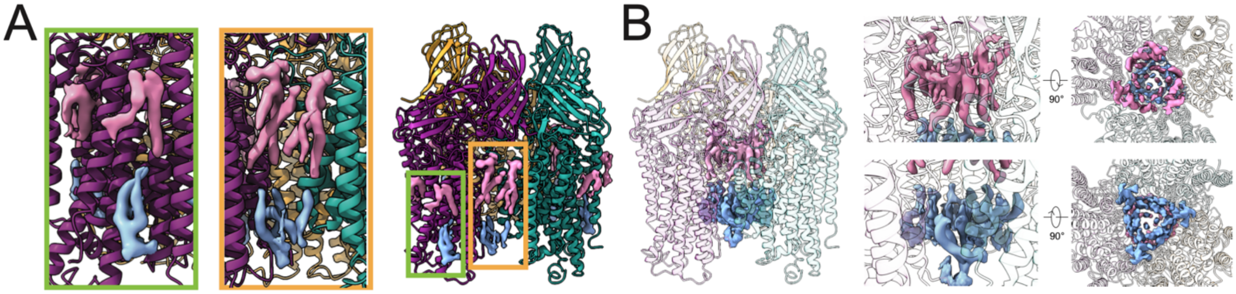

Figure 2.3. Lipid densities in *M. capsulatus* (Bath) cryoEM map (MC01). The three symmetric protomers are shown in purple, teal, and gold. Lipids in the periplasmic leaflet of the bilayer are shown in pink, and cytoplasmic leaflet lipids are shown in blue. (**A**) Lipids on the periphery of pMMO. (**B**) Lipids on the interior pore of pMMO with side-on views of each leaflet and views from top-down and bottom-up showing the packing of lipids within the bilayer.

2.3.3. CuB site and bis-His site

The two periplasmic cupredoxin domains of PmoB extend out of the nanodisc (Fig. 2.2B) and exhibit the same folds as observed crystallographically, with two copper sites readily apparent in each cryoEM map. The Cu_B site is coordinated by His33, His137, His139, and the amino terminus of PmoB in a square planar geometry (Fig. 2.4). In addition, two water molecules, located 3.6-3.7 Å from the copper ion, stabilize the site via hydrogen bonding interactions. Although axial water ligands were identified in crystallographic and spectroscopic studies of Cu_B (*10, 23-25*), the observed water molecules are too distant for coordination. As in the crystal structures, the density for His33 and the amino terminus is less clear, suggesting that it is somewhat flexible. The Cu_B site is unequivocally mononuclear (fig. S2.6), in contrast to a recent cryoEM structure of *M. capsulatus* (Bath) pMMO in DDM (*26*), but consistent with recent spectroscopic[71,180,181] and computational studies.[77] The corresponding Cu_B sites in the cryoEM structures of pMMO from *Mc.* sp. str. Rockwell and *Mt. alcaliphilum* comb. nov. 20Z exhibit the same mononuclear structure (RW01 and 20Z01, Table S2.2, fig. S2.6).

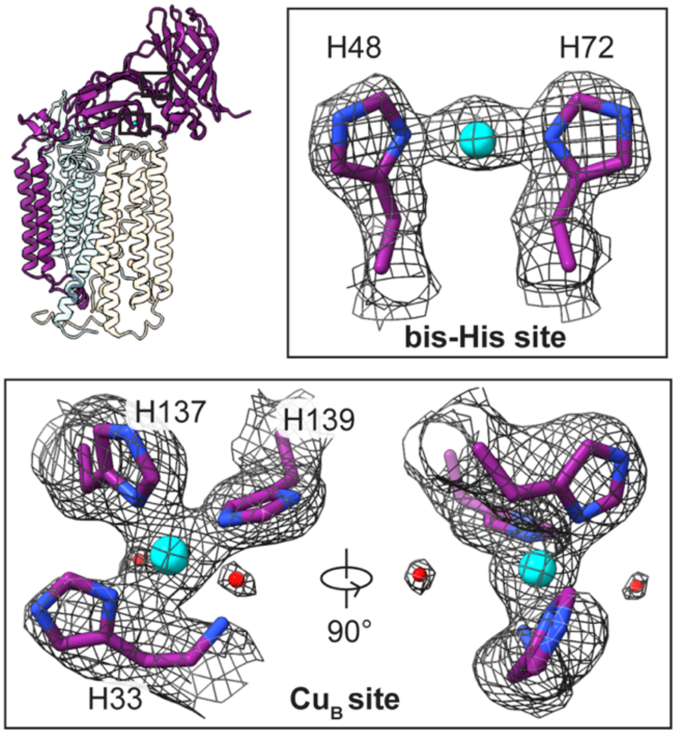

Figure 2.4. Copper sites in the PmoB subunit of *M. capsulatus* (Bath) pMMO. The protomer model is shown with the PmoB subunit highlighted and the regions housing the copper sites boxed. Copper ions and water molecules are shown as cyan and red spheres, respectively. The cryoEM map (MC01) shown as a gray mesh.

The bis-His site, coordinated by residues His48 and His72 (Fig. 2.4), is also present consistent with the *M. capsulatus* (Bath) pMMO crystal structure.[59] This site is occupied in the *Mt. alcaliphilum* comb. nov. 20Z pMMO cryoEM map (fig. S2.6), despite being unoccupied in the crystal structure.[63] The ligand corresponding to His48 is replaced with asparagine in *Mc.* sp. str. Rockwell pMMO, and the bis-His site is unoccupied (fig. S2.6). Whereas a recent cryoEM study of *M. capsulatus* (Bath) pMMO in DDM suggested the presence of three additional copper ions in PmoB,[182] no density at these specific locations is apparent in any of the maps of active pMMO in nanodiscs (fig. S2.7). There is no support in any of the structures for prior claims that a "Cu(I) sponge" in PmoB mediates electron transfer.[182,183]

2.3.4. Lipids and PmoA

In the transmembrane region, lipids coat the exterior of pMMO (Fig. 2.2C), with a total of 36 lipids modeled into the map as phosphatidylcholines along with 18 acyl chains of which the head groups are not visible (Fig. 2.3). A bilayer is observed in the interior of the pMMO trimer, showing that what appears to be a pore in the crystal structures is filled by phospholipids when embedded in a membrane-like environment (Fig. 2.2C). The longest acyl chain could be resolved to 12 carbons, with the density becoming less clear as the tails extend toward the middle of the bilayer. To investigate the possible identities of these native phospholipids, both *M. capsulatus* (Bath) whole cells and the native lipid pMMO-nanodisc complex were subjected to lipidomics analysis by liquid chromatography-tandem mass spectrometry (LC-MS/MS). A mixture of phosphatidylethanolamine (PE), phosphatidylcholine (PC), phosphatidylglycerol (PG), and cardiolipin (CL) was identified (fig. S2.8). For comparison, the structure of *M. capsulatus* (Bath) pMMO in a POPC nanodisc was determined to 2.26 Å resolution (MC02, Table S2). The lipid densities appear very similar between the two maps, suggesting that the majority of observed lipids are PC lipids (fig. S2.9), although other native lipids may remain associated with pMMO through the nanodisc reconstitution process. One exterior lipid density exhibits an unusual shape, suggesting that it may have a different identity, such as a native quinol that remains bound during purification and nanodisc reconstitution (fig. S2.9). This density occupies the position filled by an unidentified helix in the *Mc.* sp. str. Rockwell pMMO crystal structure[62] and in the cryoEM structure (RW01).

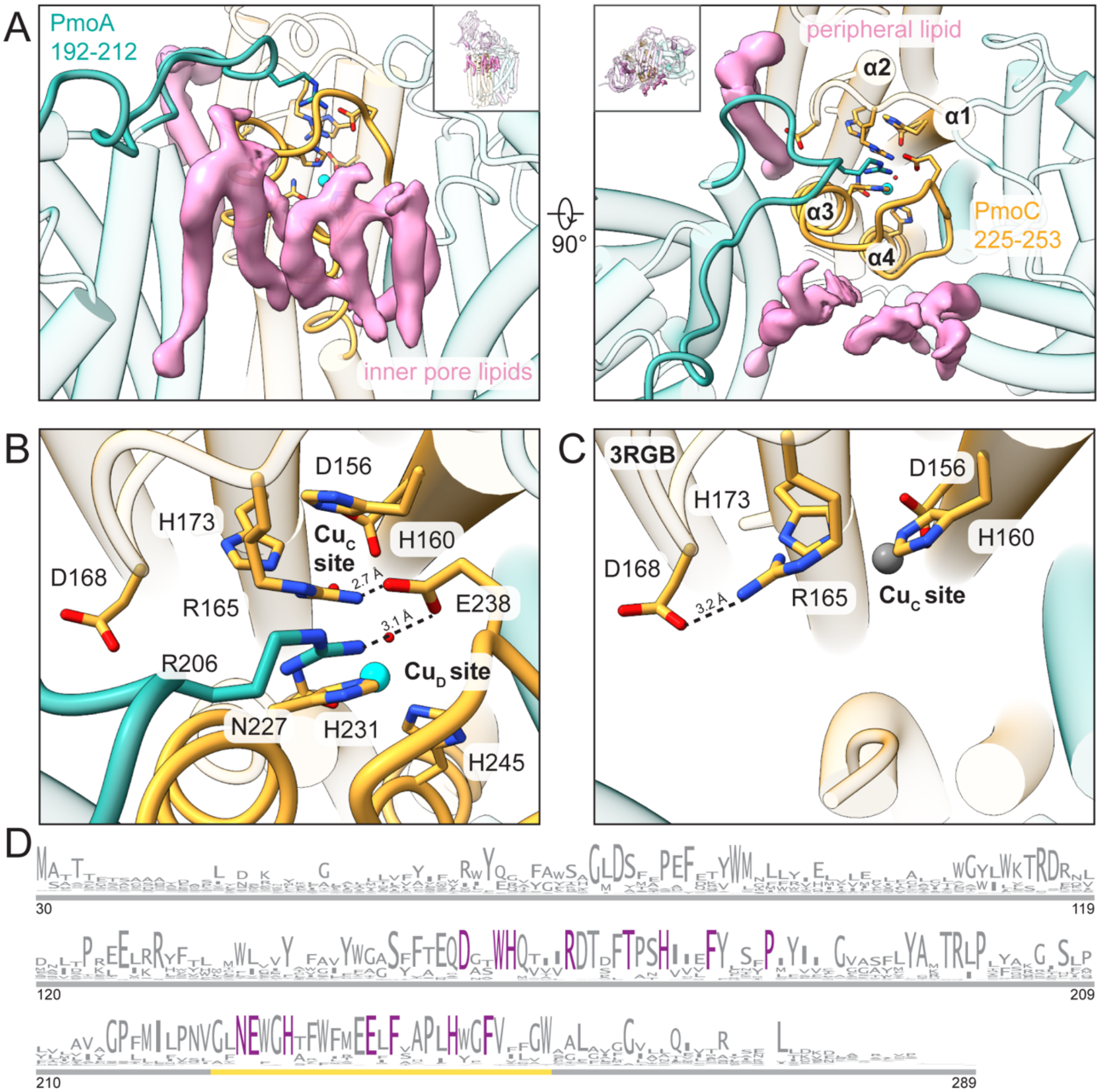

Figure 2.5. Regions of *M. capsulatus* (Bath) pMMO newly observed in the cryoEM structures. (**A**) Newly modeled residues in PmoA (192-212) and PmoC (225-253) are highlighted in teal and gold, respectively. CryoEM densities corresponding to lipids that interact with these regions are in pink. (**B**) Magnified view of the completed four-helix bundle from the cryoEM structure (MC01). Key residues are labeled and the hydrogen-bonding network involving Arg206 (PmoA), Glu238 (PmoC), and Arg165 (PmoC) is marked with dashed lines. The $\mathrm{Cu_D}$ site copper ion is shown as a cyan sphere. (**C**) Magnified view of the same region shown in (B) in the crystal structure (PDB ID: 3RGB) (*9*) with the hydrogen bond between Asp168 and Arg 165 shown as a dashed line. The zinc ion occupying the $\mathrm{Cu_C}$ site is shown as a gray sphere. (**D**) Sequence logo for the PmoC subunit (PF04896). Only sequences found in pMMO or ammonia monooxygenase operons are included. Residues conserved at 100% are colored in purple. The gold line demarcates the newly-stabilized region in the cryoEM structures.

Several regions of *M. capsulatus* (Bath) pMMO that were not observed in the crystal structures are ordered in the cryoEM maps. PmoA residues 192-212 are stabilized by phospholipids on the interior and exterior of the enzyme (Fig. 2.5A). This part of PmoA extends into PmoC, with PmoA residue Arg206 forming a hydrogen bond with PmoC residue Glu238 (Fig. 2.5B), a strictly conserved residue not observed in the crystal structures (Fig. 2.5C, D). There is no evidence for a tricopper "D" site proposed to be depleted from the inactive pMMO.[184] Although two of the three copper ions in this putative site were recently modeled in the cryoEM structure of *M. capsulatus* (Bath) pMMO in DDM,[182] our high resolution maps instead show Glu154 and a water molecule in the region (fig. S2.10). This water molecule forms hydrogen bonds with putative tricopper ligands Glu100 from PmoA and Glu154 from PmoC, which in turn is hydrogen bonded to Asn103 from PmoA, also claimed to be a ligand.[182] The other hypothetical ligands, His38 and Met42, do not interact with any additional densities that could be attributed to copper ions (fig. S2.10). Moreover, a suggested hydrophobic pocket for substrate binding involving Trp48, Phe50, Trp51, and Trp54[185] is occupied by Asp47 from PmoA.

2.3.5. PmoC and Cu$_D$

The highly conserved region of PmoC (Fig. 2.5D) that was unmodeled in the crystal structures (Fig. 2.5C, fig. S2.11) and the recent cryoEM structure of pMMO in DDM[182] is observed in all the cryoEM maps (figs. S2.11 and S2.12). This region corresponds to residues 225-253 in *M. capsulatus* (Bath) pMMO. Hydrophobic residues from this sequence interact with phospholipid tails in the trimer interior, including close interactions between phospholipids and previously unmodeled residues (fig. S2.12). These interactions stabilize a four-helix bundle comprising residues 123-163 (α1), 170-199 (α2), 220-233 (α3), and 244-270 (α4) (Fig. 2.5A). The Cu_C ligands, Asp156, His160, His173, derive from the helices α1 and α2. This structure is observed in each of the *M. capsulatus* (Bath) pMMO maps, including the POPC nanodisc (MC02, Table S2.2), suggesting that the stabilizing effect is imparted by the bilayer rather than a particular native lipid. The nanodisc and lipid environment may restore activity to pMMO (Fig. 2.2A) by stabilizing catalytically-important features of this highly conserved region.

The environment of the crystallographically-modeled Cu_C site is drastically altered in the cryoEM structure. Newly-observed helices α3 and α4 house three strictly conserved residues, Asn227, His231, and His245, which extend toward the crystallographic Cu_C ligands Asp156, His160, and His173 (Fig. 2.5B). Residue Arg165, which was hydrogen-bonded to Asp168 in the crystal structure (Fig. 2.5C), is now positioned near the Cu_C site via a hydrogen bonding network to Glu 238 and PmoA Arg 206 (Fig. 2.5B, 2.6A). Arginine residues in hydrophobic environments play a variety of functional roles in enzymes, including regulating redox potentials and substrate binding.[186,187] Unexpectedly, Asn227, His231, and His245 are connected to a strong density that distinctly resembles a metal ion (Fig. 2.6B). This metal ion is ligated by the side chain ε nitrogens of the two histidine residues (Cu-N, 2.0 Å) and the side chain of Asn227 (2.35 Å) in a trigonal planar geometry (Fig. 2.6B). The metal ion density is more persistent than the surrounding protein density at higher thresholds and is present in the cryoEM maps of three independent samples of *M. capsulatus* (Bath) pMMO in both native (Table S2.2, MC01, MC04) and POPC (Table S2.2, MC02) nanodiscs (Fig. 2.6B, Fig. 2.7). Given that copper restores activity to metal-depleted membranes[62] and to nanodisc samples,[78] it is likely that the density corresponds to a previously unknown copper site, denoted here as Cu_D (not to be confused with the proposed "D" site in PmoA[182]). The Glu228 carboxylate group is within hydrogen bonding distance of the Asn227 side chain, consistent with hydrogen bonding via its side chain amide group and coordination of copper by its side chain oxygen atom (Fig. 2.8). Copper coordination by the side chain oxygen of asparagine or glutamine is unusual, but not unprecedented.[188-191] Recent X-band electron paramagnetic resonance (EPR) and electron nuclear double resonance (ENDOR) spectroscopic studies of *M. capsulatus* (Bath) pMMO in POPC nanodiscs indicate the presence of two histidine ligands to the copper ion spectroscopically assigned as $\mathrm{Cu_C}$,[181] a finding that would be consistent with either the structural $\mathrm{Cu_C}$ or $\mathrm{Cu_D}$ site.

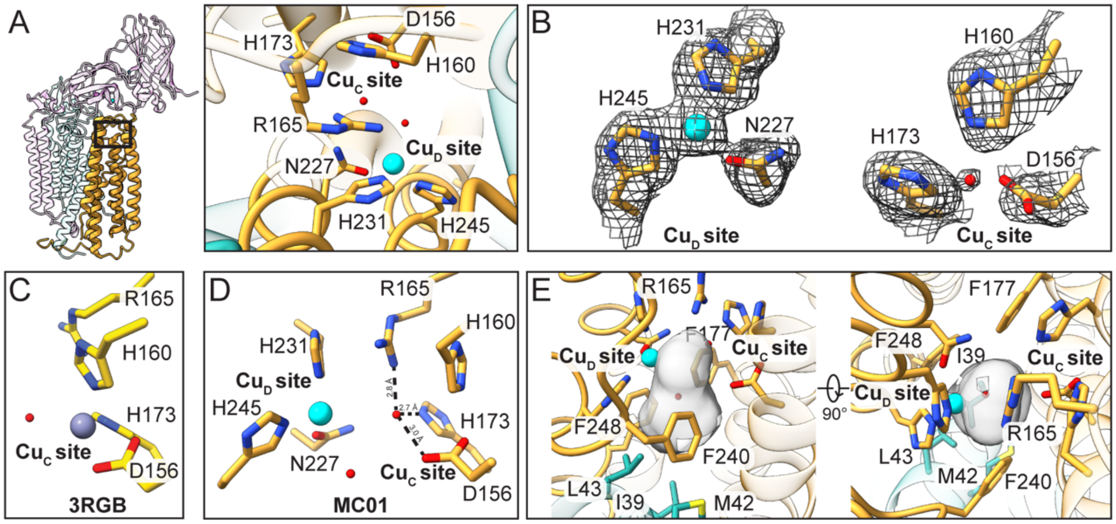

Figure 2.6. Active site architecture in the PmoC subunit of *M. capsulatus* (Bath) pMMO. (**A**) The protomer is shown with the PmoC subunit highlighted and the region housing the metal binding sites boxed and as a magnified top-down view. (**B**) The map (MC01) at the $\mathrm{Cu_D}$ and $\mathrm{Cu_C}$ sites. (**C**) The corresponding model for the crystal structure (PDB ID: 3RGB)[61] in which the $\mathrm{Cu_C}$ site is occupied by zinc. The model lacks residues 225-253, which include the $\mathrm{Cu_D}$ site residues. (**D**) Overall model of $\mathrm{Cu_C}$ and $\mathrm{Cu_D}$ sites with hydrogen bonds involving the water molecule in the $\mathrm{Cu_C}$ site shown as dashed lines. (**E**) Cavity located between and below the two sites shown in gray, generated using CASTp.[192] Residues lining the cavity are labeled.

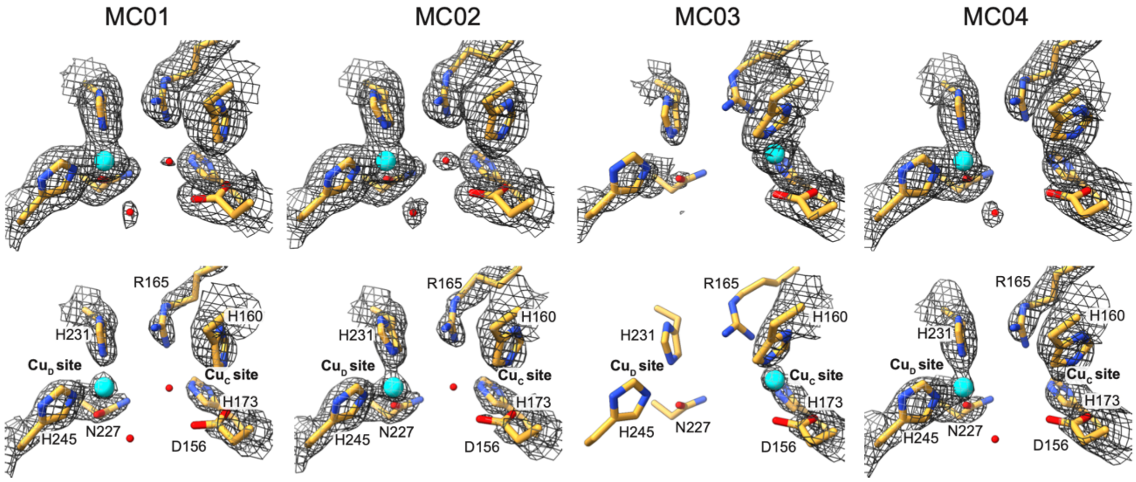

Figure 2.7. CryoEM density for copper ions at $\mathrm{Cu_C}$ and $\mathrm{Cu_D}$ in native lipid (MC01, MC03, MC04) and POPC (MC02) nanodiscs. Each map is shown at two thresholds, showing mononuclear density for $\mathrm{Cu_D}$ in MC01, MC02 and MC04 and mononuclear density for $\mathrm{Cu_C}$ in MC03 at the higher threshold.

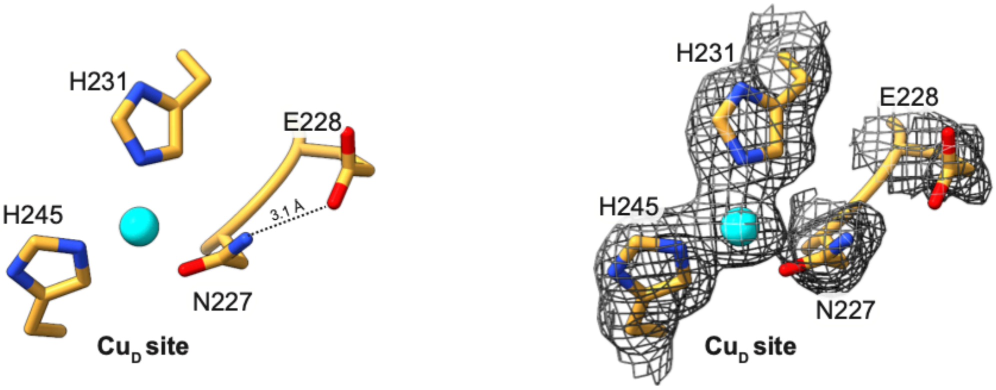

Figure 2.8. Coordination of Asn227 to $\mathrm{Cu_D}$ site. A hydrogen bond between Glu228 and Asn227 positions the side chain oxygen of Asn227 to coordinate copper.

In contrast to the $\mathrm{Cu_D}$ site, the $\mathrm{Cu_C}$ site is only apparent in one map of *M. capsulatus* (Bath) pMMO (Table S2.2, MC03, Fig. 2.7), with strong density connected to that of the three $\mathrm{Cu_C}$ ligands, Asp156 (2.7 Å), His160 (2.1 Å), and His173 (2.2 Å). The presence of $\mathrm{Cu_C}$ correlates with increased disorder in the loop (residues 233-240) connecting newly visible helices α3 and α4 in PmoC. Although density for the $\mathrm{Cu_D}$ ligands is still observed, there is no density attributable to a metal ion (Fig. 2.7). Similarly, the *Mt. alcaliphilum* comb. nov. 20Z pMMO map (Table S2.2, 20Z01) exhibits a clear $\mathrm{Cu_C}$ site (fig. S2.13A), but the density for the region corresponding to *M. capsulatus* (Bath) PmoC residues 233-240 (residues 206-213 in *Mt. alcaliphilum* comb. nov. 20Z PmoC) is poorly defined (fig. S2.12A), and completely lacks side chain density for Arg 165 (Arg 137 in *Mt. alcaliphilum* comb. nov. 20Z PmoC, fig. S2.13A). There is no obvious density for $\mathrm{Cu_D}$, and nanodisc samples of *Mt. alcaliphilum* comb. nov. 20Z pMMO exhibit no methane oxidation activity (Table S2.1). The $\mathrm{Cu_C}$ site is again observed in the *Mc.* sp. str. Rockwell pMMO map, and the region containing the $\mathrm{Cu_D}$ ligands (residues 200-221), although ordered (fig. S2.12A), lacks side chain density (fig. S2.13B). Upon further processing of this map using deepEMhancer,[193] the $\mathrm{Cu_D}$ site ligands were resolved (fig. S2.13B). In all six maps, the density at the $\mathrm{Cu_C}$ or $\mathrm{Cu_D}$ sites is not as strong as that observed at $\mathrm{Cu_B}$, which is consistent with the full $\mathrm{Cu_B}$ occupancy observed by crystallography and nTDMS.[78]

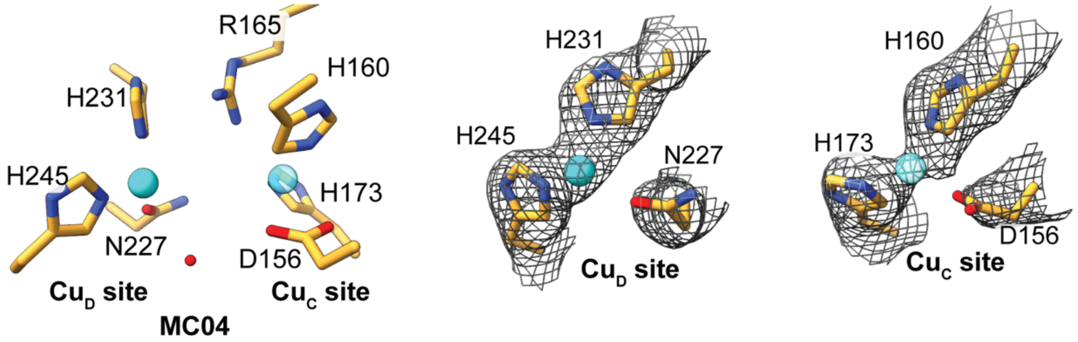

Figure 2.9. Alternate views of MC04 model and density showing density possibly corresponding to a copper ion at the Cu_C site. The water molecule present in Cu_C in MC01 and MC02 is missing while the density is continuous, suggesting that there may be copper in this site at low occupancy.

In two of the three *M. capsulatus* (Bath) pMMO maps that show density for $\mathrm{Cu_D}$ (Table S2.2, MC01, MC02), there is no density between the $\mathrm{Cu_C}$ ligands. In contrast, the crystal structure contains zinc derived from the crystallization buffer at the $\mathrm{Cu_C}$ site (Fig. 2.6C), and crystal structures of pMMO isolated from *Mc.* sp. str. Rockwell contain copper in this site.[62] In the cryoEM maps lacking density for $\mathrm{Cu_C}$, residue His160 adopts a slightly different conformation, presumably because it is no longer stabilized by copper coordination. Instead of $\mathrm{Cu_C}$, a spherical density ~2 Å from the location of $\mathrm{Cu_C}$ is observed (Fig. 2.6B). This density was modeled as a water molecule because it is within hydrogen bonding, rather than coordinating, distance of $\mathrm{Cu_C}$ ligands Asp156 and His173 as well as Arg165 (Fig. 2.6D). This water molecule is not present in the third map (Table S2.2, MC04). Instead, the density corresponding to $\mathrm{Cu_C}$ ligands His160 and His173 is weakly connected (Fig. S2.9), opening the possibility that the $\mathrm{Cu_C}$ and $\mathrm{Cu_D}$ sites, separated by ~5.7 Å, might be occupied simultaneously.

2.3.6. *Cavity and $\mathrm{Cu_D}$ identity*

Strikingly, the cryoEM model of active *M. capsulatus* (Bath) pMMO reveals a hydrophobic cavity adjacent to the $\mathrm{Cu_D}$ site (Fig. 2.6E), extending away from the periplasmic side of pMMO. This cavity is lined by PmoA residues Ile39, Met42, Leu43 and PmoC residues Phe177, Phe240, and Phe248. These three PmoC residues are invariant (Fig. 2.5D), and the latter two derive from the newly observed region of PmoC. This cavity houses the aforementioned water molecule and abuts the location of the $\mathrm{Cu_D}$ ligands (Fig. 2.6D). Its existence supports assignment of the pMMO active site as one or both of the two copper sites, $\mathrm{Cu_C}$ and $\mathrm{Cu_D}$.

All four *M. capsulatus* (Bath) pMMO samples had similar activities and copper contents (Fig. 2.2A, fig. S2.2), precluding correlation of the Cu_C and Cu_D occupancies with methane oxidation. Treating the nanodiscs with excess copper after reconstitution did not increase the apparent occupancy of either site and was found to inhibit activity, consistent with previous studies showing the inhibitory effect of excess copper.[62] Although we assigned Cu_D as copper on the basis of extensive data linking copper addition to restored activity,[62,78] cryoEM data, unlike X-ray diffraction data,[194] (*39*), do not allow for unambiguous metal identification. Other possibilities include iron and zinc, but iron does not restore activity to metal-depleted membranes,[46] and zinc inhibits activity.[62] In addition, only heme iron, attributed to cytochrome impurities, has been detected spectroscopically in pMMO.[76]

2.3.7. Cyanide treatment of pMMO

To further probe the identity of the metal ion at Cu_D and its role in methane oxidation, metals were chelated from *M. capsulatus* (Bath) membranes using potassium cyanide,[62,195] and the sample was split into two batches, of which one was treated with 10 equivalents of $CuSO_4$. pMMO was solubilized from both batches, reconstituted into nanodiscs, and investigated by cryoEM. A cryoEM map of the metal-depleted sample, which contained 0.1 equivalent of Cu (fig. S2.14), was resolved to 3.65 Å (fig. S2.15A, Table S2.2, MC05). Some density is still observed at Cu_B, but the occupancy of the bis-His site is reduced significantly (Fig. 2.10A). Whereas the PmoB and PmoA subunits remain intact, the PmoC subunit is completely disrupted (Fig. 2.10A) and the sample exhibits no methane oxidation activity (fig. S2.16). There is no density for residues 54-97, comprising the first helix, residues 160-178, including the Cu_C site, and residues 221-246, including the Cu_D site. The disordered regions are bracketed by coordinating histidines (Cu_C His160 and Cu_D His245), indicating that PmoC requires copper for structural stability. In addition, all of the stabilized lipids are disrupted in this structure.

The cryoEM map of the metal-depleted, copper-reloaded sample, which contained ~0.6 equivalents of copper (fig. S2.14), was resolved to 3.39 Å (fig S2.15B, Table S2.2, MC06). Despite the lower resolution, lipids on the inner pore and periphery of pMMO are clearly visible and the backbone could be traced through the entire PmoC subunit (Fig. 2.10B). Thus, the destabilizing effects of copper removal on structure can be reversed upon copper addition. The Cu_B and bis-His sites are more fully occupied (Fig. 2.10B) as well. Although residues at the Cu_D site are less well defined, there is density near His245 and Asn227 that could correspond to a metal ion (Fig. 2.10C), supporting the assignment of Cu_D as a copper binding site. The Cu_C site residues are well defined and oriented towards one another, but the site appears unoccupied (Fig. 2.10C). Importantly, this sample also exhibits methane oxidation activity (fig. S2.16), on par with pMMO reconstituted into native nanodiscs with no additional copper added (Fig. 2.2A), and consistent with previous studies showing that ~50% of activity can be regained after cyanide treatment and copper reloading.[62] This result links reloading of Cu_D to recovery of some methane oxidation activity.

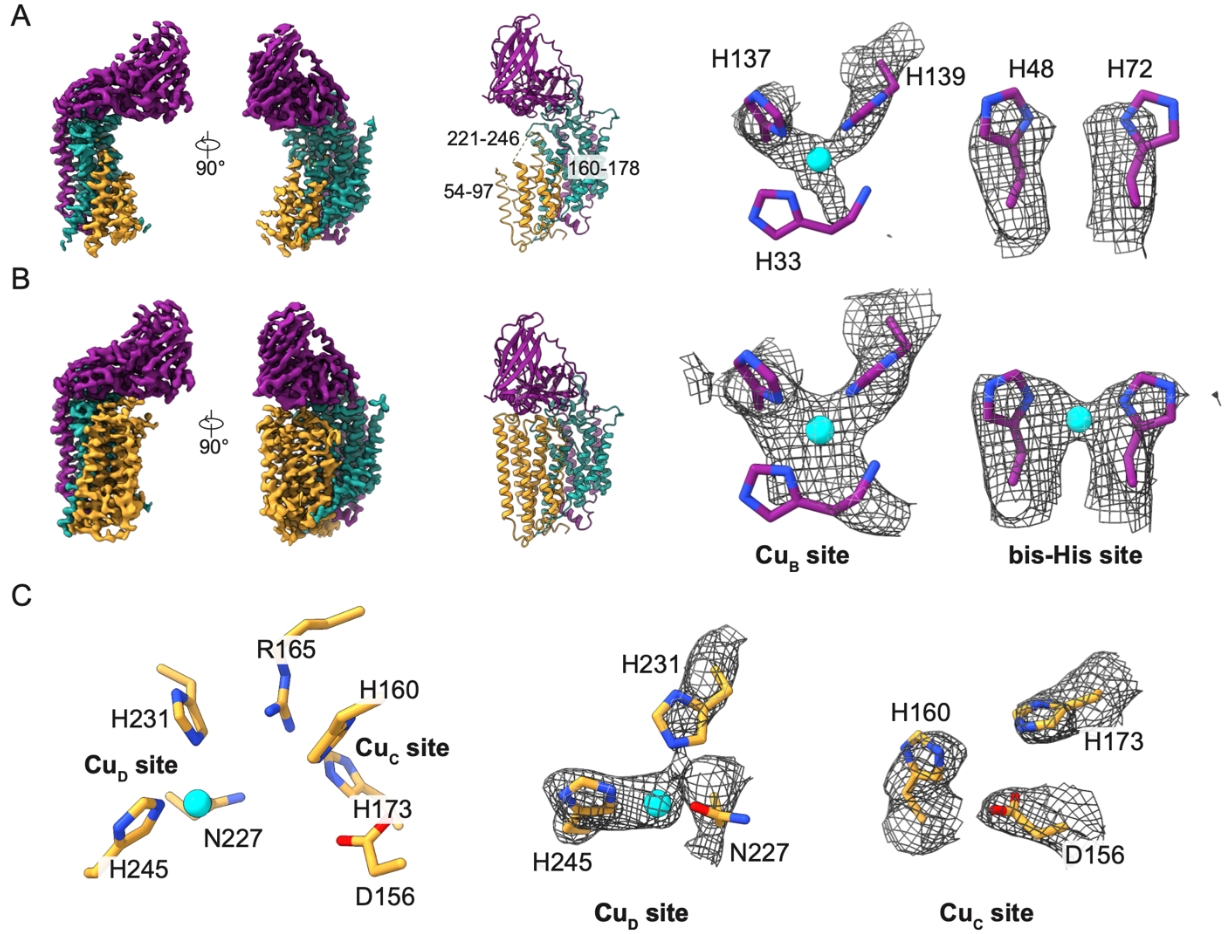

Figure 2.10. Structure of potassium cyanide (KCN)-treated pMMO from *M. capsulatus* (Bath) reconstituted into nanodiscs. (**A**) A single protomer from the 3.65 Å resolution map of KCN-treated pMMO in a native lipid nanodisc with no added copper (MC05) and the model with missing residues labeled. The $\mathrm{Cu_B}$ and bis-His sites are shown at the same threshold level. (**B**) A single protomer from the 3.39 Å map of KCN-treated pMMO with copper added back before pMMO isolation and during reconstitution into native lipid nanodiscs (MC06). The complete model is shown along with the $\mathrm{Cu_B}$ and bis-His sites at the same threshold. (**C**) PmoC metal-binding sites in MC06. $\mathrm{Cu_C}$ and $\mathrm{Cu_D}$ are shown at the same threshold level. Residues in the $\mathrm{Cu_D}$ site are not as well defined, although there is a strong density near the location of the $\mathrm{Cu_D}$ metal ion in the other, high resolution maps (MC01, MC02, MC04). The $\mathrm{Cu_C}$ residues fit well into the density, although there is no evidence for metal occupancy.

2.4. Conclusion

These first structures of active pMMO, obtained by embedding the enzyme in a native lipid bilayer, provide critical insight into pMMO structure and function. The combined results indicate that an intact PmoC scaffold, including Cu_C and Cu_D ligands supported by a hydrogen bonding network and interior lipid bilayer, is associated with enzymatic activity. The presence of Cu_D in the majority of *M. capsulatus* (Bath) cryoEM structures suggests a role in activity, but the occupancy of the Cu_C and Cu_D sites in vivo remains to be determined. The structure of the highly-conserved region of PmoC, along with the unexpected discovery of the Cu_D site and adjacent hydrophobic cavity, provide a much more complete picture of the pMMO active site architecture. This dramatically revised view of pMMO, obtained after >15 years of crystallographic characterization, underscores the importance of studying membrane proteins in their native environments and the potential of high resolution cryoEM combined with membrane mimetic technology.

2.5 Methods

2.5.1 Methanotroph growth

Methanotrophs were cultured in 12 L of media using a BioFlo 4500 fermentor (New Brunswick Scientific) following established protocols.[59,62,196] *M. capsulatus* (Bath) was cultured in 1 X nitrate mineral salts media, 3.9 mM phosphate buffer, pH 6.8, supplemented with 80 μM NaFeEDTA, 50 μM $CuSO_4 \cdot 5H_2O$, and trace element solution at 45 °C and a continuous flow of 1 L/min at a 1:3 ratio of methane:air. Cells were harvested at an OD_{600} of 8-10, pelleted, and flash frozen in liquid nitrogen. *Mc.* sp. str. Rockwell was cultured in salt solution, 3.9 mM phosphate buffer, pH 6.8, supplemented with 40 μM $FeSO_4$, 50 μM $CuSO_4 \cdot 5H_2O$, and trace elements solution at 30 °C and a continuous flow of a 1:4 ratio of methane:air. *Mt. alcaliphilum* comb. nov. 20Z was grown in 1 X nitrate mineral salts media, 0.5 M NaCl, 2.3 mM phosphate buffer, pH 6.8, 50 mM carbonate buffer, pH 9.5, 40 μM $CuSO_4 \cdot 5H_2O$, and trace element solution at 30 °C and a continuous flow of a 1:3 ratio of methane:air.

2.5.2. pMMO isolation

Membranes were isolated according to previous methods.[63] *M. capsulatus* (Bath) and *Mt. alcaliphilum* comb. nov. 20Z cell pellets were thawed in 25 mM PIPES, pH 7.3, 250 mM NaCl. For *Mc.* sp. str. Rockwell cell pellets, $CuSO_4 \cdot 5H_2O$ was added to a concentration of 500 μM.[62] Cells were lysed by sonication on ice at 35% amplitude with 1 s alternating pulses for 9 min (Qsonica Q700). Lysed cells were subjected to two rounds of centrifugation at 10,000 x g for 45 and 25 min, discarding the pellet after each cycle. The supernatant was then centrifuged at 150,000 x g for 1 h to pellet the membranes. The supernatant was discarded, and the membrane fraction was subjected to 2 rounds of homogenization using a Dounce homogenizer in 25 mM PIPES, pH 7.3, 250 mM NaCl followed by centrifugation to re-pellet the membranes at 150,000 x g for 30 min. Following the last round of centrifugation, the membranes were homogenized in 7 ml of the same buffer, aliquoted, flash frozen, and stored at -80°C. The concentration of protein in the membranes was measured using the DC Lowry assay (Bio-Rad) with BSA as a standard.

pMMO was solubilized from the membranes using n-dodecyl-β-D-maltopyranoside (DDM). Membranes were thawed on ice, and DDM was added at a ratio of 1.2 mg DDM:1 mg pMMO, followed by mixing end-over-end at 15 rpm for 1 h at 4 °C. To remove remaining membranes and aggregated protein, the mixture was centrifuged for 1 h at 150,000 x g, and the pellet was discarded. Solubilized pMMO was then exchanged into buffer containing 25 mM PIPES pH 7.3, 250 mM NaCl, and 0.02% DDM using Amicon concentrators (MilliporeSigma) with a molecular weight cutoff of 100 kDa. The concentration was measured using the DC Lowry (Bio-Rad) assay with BSA as a standard, pMMO was diluted to a concentration of 10 mg/ml, and aliquots were flash frozen and stored at -80°C.

2.5.3. Membrane scaffold protein expression and purification

Plasmid pMSP1E3D1 (Addgene) was transformed into *E. coli* BL21 Star (DE3) cells and grown on LB-agar plates containing 30 µg/ml kanamycin. Cultures were grown in 5 ml LB for 18 h and then in 200 ml LB for 18 h. The 200 ml culture was used to inoculate 12 L TB media at an optical density at 600 nm (OD_{600}) of ~0.1 and shaken at 180 rpm at 37 °C. Expression of MSP1E3D1 was induced at an OD_{600} of ~2.4 (~4 h) by adding 1 mM IPTG. Cells were then grown for 4 h at 37 °C, harvested by centrifugation at 8000 x g for 15 min, flash frozen, and stored at -80 °C. Each 12 L TB culture yielded ~60 g of cells.

Cell pellets were thawed in Tris buffer containing 40 mM Tris, pH 7.3, 250 mM NaCl, and 10 mM imidazole with 1% Triton X-100, DNase (Sigma), and Protease Inhibitor Cocktail (Roche). Cells were lysed by sonication on ice with 1 s pulse on 2 s pulse off for 10 min (Qsonica Q700). The lysate was centrifuged for 30 min at 10,000 x g to remove insoluble aggregates. The soluble fraction was then applied to a gravity column containing 10 ml NiNTA beads. The column was washed with 5 column volumes (cv) Tris buffer with 50 mM sodium cholate, followed by 15 cv Tris buffer. The protein was eluted with 5 cv Tris buffer containing 250 mM imidazole. TEV protease was added to the eluted protein at a ratio of 1:20 protease:protein and dialyzed overnight at 4 °C against Tris buffer containing 1 mM EDTA. TEV protease and uncleaved protein were then removed by flowing over the NiNTA column and collecting the flow-through. MSPs were concentrated and buffer-exchanged into 25 mM PIPES, pH 7.3, 250 mM NaCl in an Amicon concentrator (MilliporeSigma) with a 10 kDa molecular weight cutoff to ~4 mg/ml, measured by nanodrop A280 using a molecular weight of 30,110 kDa and an extinction coefficient of 26,930 M^{-1} cm^{-1}. Aliquots were flash frozen and stored at -80 °C.

2.5.4. Lipid preparation

DMPC and POPC solubilized in chloroform (Avanti) were dried down to a thin layer in a glass vial at room temperature under a stream of nitrogen gas and then stored overnight in a vacuum desiccator to remove remaining trace amounts of chloroform. These dried lipids (25 mg per vial) were resolubilized in 25 mM PIPES, pH 7.3, 250 mM NaCl, and 100 mM sodium cholate to a final lipid concentration of 50 mM.

For native lipids, *M. capsulatus* (Bath) cell pellets were thawed and resuspended in 20 ml methanol per 1 g cells. The suspension was homogenized in a Dounce homogenizer with an additional 10 ml dichloromethane and 5 ml 40 mM phosphate buffer, pH 7.4. The organic and aqueous layers were allowed to separate overnight, and the organic layer was then removed by aspiration. The organic layer was dried under a stream of nitrogen to form an oily layer, which was dried further in a vacuum desiccator overnight.

The weight of dried lipids was measured, and an approximately 50 mM stock solution of solubilized lipids was prepared by assuming an average molecular mass of 700 g/mol for extracted native lipids. The lipids were solubilized in 25 mM PIPES, pH 7.3, 250 mM NaCl, and 100 mM sodium cholate. To fully resuspend, the solubilized lipids were alternately heated at 50 °C, vortexed, and soaked in an ultrasonic bath for 20 s each until the lipids were fully dissolved. This stock was then aliquoted and frozen at -20 °C for later use. Typically, one gram of cells yielded ~20-40 mg of dry lipids from *M. capsulatus* (Bath).

2.5.5. Lipidomics

Lipidomics analysis was performed by Cayman Chemical (Ann Arbor, MI). Internal standards, including TG (16:0-d9/16:0/16:0), SM (d18:1/16:0-d9), DG (16:0-d9/16:0), CE (16:0-d9), PC (16:0-d9/16:0), PE (16:0-d9/16:0), PI (16:0-d9/16:0), PS (16:0-d9/16:0), and LysoPC (16:0-d9/0:0) were added to *M. capsulatus* (Bath) whole cells and native lipid nanodiscs along with 1 ml phosphate buffered saline:methanol 1:1 (v/v). This mixture was homogenized using a Precellys homogenizer using three 30 s cycles at 8000 rpm, with a 3 min rest interval on ice between cycles.

A methyl-tert-butyl ether (MTBE)-based liquid-liquid extraction procedure was then used. After adding 4 mL MTBE to each sample and vortexing vigorously, the mixture was incubated on a tabletop shaker at 500 rpm at room temperature for 1 h. Phase separation was induced by the addition of 1 ml water. The samples were shaken for 10 min, and then centrifuged at 2000 x g for 15 min. The upper organic phase of each sample was carefully removed using a Pasteur pipette and transferred into a fresh glass tube. The remaining aqueous phase was reextracted with 2.5 mL of MTBE:methanol:water 10:3:2.5 (v/v/v). After vortexing and centrifuging as above, the organic phase was collected and combined with the initial organic phase. The extracted lipids were dried in a SpeedVac vacuum concentrator. The dried lipid extracts were reconstituted in 200 µl n-butanol:methanol 1:1 (v/v) and transferred into autosampler vials for lipidomic analysis by LC-MS/MS.

Lipostar (Version1.3.1b18; Molecular Discovery) software was used for feature detection, noise and artifact reduction, alignment, normalization, and lipid identification. Peak picking, smoothing, and retention time alignment were performed to identify unique *m/z* and retention time features. A retention time window filter of 1-32 min was used. Background peaks that appeared in blank solvent were removed along with peaks that did not contain MS/MS spectra, peaks that did not present any isotope pattern, and background noise.

Automated lipid identification was performed using the Lipid Maps database. This database includes major lipid classes (phospholipids, sphingolipids, DAGs, TAGs, and sterols) for both positive- and negative-ion modes and has been modified by Cayman to include extra lipids (e.g. many additional cardiolipins and some internal standards). The identification algorithm uses the detected accurate-mass m/z with a 5-ppm mass tolerance filter, as well as the corresponding MS/MS spectrum to identify lipids and ranks the identifications via a 1-to-4-star scale of increasing confidence. One-star ranked identifications were excluded. The integrated areas of all identified lipids were normalized to the integrated area of their corresponding class- specific internal standard. Identifications of the five most abundant molecular species in each class (sorted by their peak area ratio) were manually reviewed using MS/MS spectra and peak integration.

2.5.6. Nanodisc reconstitution

pMMO was reconstituted into nanodiscs following established protocols.[176,197] The following procedures were all conducted at 4 °C. pMMO in 0.02% DDM was mixed with lipids, MSP, and $CuSO_4$ at specific ratios and mixed end-over-end at 15 rpm for 30 min. For DMPC, a molar ratio of 1:75:240 pMMO:lipid:MSP was used. For POPC and native lipids, a molar ratio of 1:60:240 was used. Since pMMO is isolated from the native organism and has no affinity tag, a ratio of MSP:pMMO was chosen at one pMMO particle per disc to minimize the amount of empty nanodiscs present. SM-2 Bio-Beads (Bio-Rad) were added at 0.8 mg/ml and mixed end- over-end at 15 rpm for 2 h. Washed Bio-Beads were prepared by soaking in buffer containing 25 mM PIPES, pH 7.3 and 250 mM NaCl and decanting the mixture over a dry weigh boat. The weight of wet Bio-Beads was measured by removing liquid using a Pasteur pipette until no more could be removed. Bio-Beads were removed from the nanodisc mixture by passing through a 0.22 μm syringe filter. The formed nanodiscs were then concentrated using an Amicon concentrator (MilliporeSigma) with a molecular weight cutoff of 100 kDa and purified by size exclusion chromatography on a Superose 6 Increase 10/300 GL column (Cytiva) in buffer containing 25 mM PIPES pH 7.3 and 250 mM sodium chloride. Peak fractions were collected and concentrated. The concentration was measured using established methods to isolate empty nanodiscs from nanodiscs containing pMMO.[78] Solubilized pMMO of known concentration was loaded onto a 15% SDS-PAGE gel at concentrations 4, 2, and 1 mg/mL alongside a sample of nanodisc-embedded pMMO. ImageJ was used to generate a standard curve, correlating the band intensity of the PmoB subunit to protein concentration. The concentration of the nanodisc- embedded pMMO sample was then determined by comparing the intensity of the PmoB band to the standard curve.

2.5.7. Activity assay and ICP-MS

The methane oxidation activity assay was conducted according to established methods.[63,71] For each assay, 100 μl pMMO, diluted to 1-5 mg ml^{-1}, either membrane-bound, DDM- solubilized or embedded in nanodiscs, was mixed with reductant (excess duroquinol) in 2-ml screw-top vials with septa tops (Agilent). 1 ml of air was removed from the vial and 1.5 ml of [^{13}C]methane was added. The mixture was shaken at 200 rpm in a water bath (45 °C for *M. capsulatus* (Bath) or 30

°C for *Mc.* sp. str. Rockwell and *Mt. alcaliphilum* comb. nov. 20Z) for 5 min followed by incubation on ice for 10 min. Negative controls were performed in the absence of [^{13}C]methane, duroquinol, or pMMO.

Samples were then prepared for GC/MS analysis. Chloroform (500 µl) containing 1 mM dicholoromethane was added to each sample. The samples were mixed at 2000 rpm for 10 min at 4 °C and centrifuged at 2000 x g for 10 min. 2.5 µl of sample was applied to a PoraBOND Q column (25 m x 250 µm x 3 µm) on an Agilent 7890B/5977A MSD GC/MS instrument with a split ratio of 10:1. The GC was maintained under a constant helium gas flow of 1.2 ml min^{-1}. The initial oven temperature was maintained at 80 °C for 3.5 min, increased at 50 °C min^{-1} to 150 °C, and held for 1.5 min. A second ramp rate of 15 °C min^{-1} was maintained until a final temperature of 300 °C was reached and held for 1 min. The mass spectrometer was maintained at a temperature of 230 °C, quad temperature of 150 °C, 70 eV, and a detector voltage of 2,999 V. Masses 31, 33, and 49 were monitored for the detection of [^{12}C]methanol, [^{13}C]methanol, and dichloromethane. The [^{13}C]methanol peak was integrated, quantified from a standard curve, and normalized to the concentration of dichloromethane.

Samples were prepared by mixing 5-50 µl of analyte with 180 µl of 100% nitric acid and heating at 60 °C for 4 h. The sample was then diluted to 6 ml with metal-free water. The samples were analyzed using an iCAP Q ICP-MS instrument (Thermo) in the Quantitative Bioelemental Imaging Facility (QBIC) at Northwestern University.

2.5.8. Bioinformatics

The PmoC sequence logo was generated from 318 representative sequences from PF04896 and TIGR03078, manually selected from 451 sequences for those located in a pMMO or AMO operon, excluding “rogue” *pmoC* and *amoC* sequences. These representative sequences were clustered at 100% identity against a hidden Markov model constructed from 132 representative nodes clustered at 50% identity using the EFI-EST webtool. Sequences were aligned using MAFFT[198] in L-INS-I mode and gaps were removed using the *M. capsulatus* (Bath) PmoC sequence as a reference. The logo visualization was generated in Jalview.[199]

2.5.9. Negative stain sample preparation and data processing

Negative stain samples were prepared at ~0.01 mg/ml protein concentration for nanodisc-embedded pMMO. 3 µl samples were applied to 400-mesh carbon-coated copper grids (Electron Microscopy Sciences) plasma cleaned at 30 W for 10 s with a Solarus plasma cleaner (Gatan). Grids were allowed to incubate in open air at room temperature for 1 min before blotting with filter paper. Grids were then washed in two successive 50 µl drops of water for 15 s each followed by two successive 50 µl drops of 0.75% uranyl formate for 15 s each with manual agitation. Grids were blotted with filter paper and allowed to dry before storage in a grid box.

Images of the grids were collected using a JEM-1400 transmission electron microscope (JEOL) at 30,000x magnification and a pixel size of 3.71 Å. Images were collected using Leginon[200] at defocus values of 3-6 µm, and 2D class averages were determined using Appion.[201]

2.5.10. CryoEM sample preparation and data collection

Samples were prepared by plunge freezing in liquid ethane using a Vitrobot Mark IV (Thermo Fisher). 3 µl of 1 mg/ml sample was applied to either 300- or 400-mesh C-flat holey carbon copper grids with 1.2 µm diameter and 1.3 µm spacing. Both 300- and 400-mesh grids yielded similar results, except that 300-mesh grids occasionally had more broken squares. Grids were prepared by plasma cleaning with a Solarus plasma cleaner (Gatan) for 10 s at a voltage of 10 W. The sample was incubated on the grid for 30 s in 100% humidity at 4 °C before dual-sided blotting for 4 s with a blot force of 7 and plunging into liquid ethane and storage under liquid nitrogen.

CryoEM screening was performed using a JEM-3200FS transmission electron microscope (JEOL) with a K2 Summit Direct Detector (Gatan) at 300 kV. Data were collected at a magnification of 30,000x and a pixel size of 1.06 Å. Movie series with defocus values of 1.5- 4.5 μm were collected using Leginon.[200] Forty-frame exposures were taken at 0.3 s per frame using a dose rate of 8 e^{-} A^{-2} per movie series. Full cryoEM datasets were collected at three national facilities (Stanford-SLAC CryoEM Center (S^2C^2), National Center for CryoEM Access and Training (NCCAT), Pacific Northwest Center for CryoEM (PNCC)) using a Titan Krios (Thermo-Fisher) electron microscope at 300 kV with calibrated magnifications of 40,000 x and 30,000 x and pixel sizes of 0.86 Å and 1.06 Å. Movie series with varying numbers of frames, dosages, and defocus values were collected as detailed in Table S2.2.

2.5.11. Structure building

Models were built using Coot[202] and Phenix[203] software. The crystal structures were used as starting models (*M. capsulatus* (Bath) pMMO, PDB 3RGB; *Mt. alcaliphilum* comb. nov. 20Z pMMO, PDB 6CXH; *Mc.* sp. str. Rockwell pMMO, PDB 4PHZ), and new residues and ligands were built manually in Coot. The models were refined using the cryoEM real space refine tool in Phenix. Residues were then manually inspected in Coot, and adjusted using the refine range tool. The douse program in the Phenix cryoEM suite[203] was used to identify water molecules in maps MC01-04, 20Z01, and RW01. The maps were inspected at multiple B-factor values in each region using the sharpen/blur tool on maps produced from the postprocess step in Relion at a manually inputted B-factor of zero. In some cases, the maps were also resampled at a higher rate using Coot in order to generate smooth densities, especially for waters and metal ions. ChimeraX was used to fit structures into density and to generate figures.[204,205]

2.5.12. Potassium cyanide treatment

Membranes from *M. capsulatus* (Bath) were treated with 50 mM potassium cyanide (KCN) according to established methods.[62,195] The membranes were first resuspended in 50 mM MOPS, pH 8.0, 250 mM NaCl, and 50 mM ascorbate using a Dounce homogenizer. Solid KCN was added to 50 mM, and the sample was incubated for 30 min at 4 °C with stirring in a fume hood, noting when the color changed from brown to pale. Membranes were recovered by ultracentrifugation at 150,000 x g for 45 min, taking care to add and remove tubes to and from the rotor in a fume hood. Membranes were washed by resuspending in MOPS buffer using a Dounce homogenizer and centrifuged again at 150,000 x g for 45 min. This procedure was repeated twice for a total of three washes before a final resuspension in MOPS buffer. The concentration was measured using the DC Lowry assay (Bio-Rad), and metal removal was confirmed by ICP-MS (fig. S19). Aliquots were stored at 4 °C for up to two weeks.

To reconstitute KCN-treated pMMO into nanodiscs, pMMO was solubilized from KCN-treated membranes with DDM as described above. For KCN-treated, copper reloaded samples,10 equivalents $CuSO_4$ (based on crude membrane protein concentration) was incubated with the membranes for 2 h at 4 °C prior to solubilization of pMMO. Nanodisc reconstitution was performed as above, and ICP-MS was used to measure the amount of $CuSO_4$ retained in the final nanodisc samples (fig. S2.14).

CHAPTER 3: Structure and assembly of particulate methane monooxygenase in intracytoplasmic membranes of methanotrophs

This work has been submitted for publication as:

Yanan Zhu[†], Christopher W. Koo[†], C. Keith Cassidy, Matthew C. Spink, Tao Ni, Laura C. Zanetti-Domingues, Benji Bateman, Marisa L. Martin-Fernandez, Juan Shen, Yuewen Sheng, Yun Song, Zhengyi Yang, Amy C. Rosenzweig and Peijun Zhang

[†]Equal contributions.

3.1. Abstract

Methane-oxidizing bacteria play a central role in greenhouse gas mitigation and have potential applications in biomanufacturing. Their primary metabolic enzyme, particulate methane monooxygenase (pMMO), is housed in copper-induced intracytoplasmic membranes (ICMs), of which the function and biogenesis are not known. We show by serial cryo-focused ion beam (cryoFIB) milling/scanning electron microscope (SEM) volume imaging and lamellae-based cellular cryo-electron tomography (cryoET) that these ICMs are derived from the inner cell membrane. The pMMO trimer, resolved by cryoET and subtomogram averaging to 4.8 Å in the ICM, forms higher-order hexagonal arrays in intact cells. Array formation correlated with increased enzymatic activity, providing a new perspective for understanding pMMO function. These findings also demonstrate the power of cryoET to structurally characterize native membrane enzymes in the cellular context.

3.2. Introduction

Methanotrophs, microbes that utilize methane from the environment as a carbon source,[10] substantially reduce atmospheric methane concentrations and represent a promising platform for biomanufacturing.[171,172] Activation of the 105 kcal/mol methane C-H bond and oxidation to methanol is accomplished by methane monooxygenase (MMO) enzymes. Some methanotrophs switch between using the iron-dependent soluble MMO (sMMO)[32] and the copper-dependent particulate (membrane-bound) MMO (pMMO)[173] as a function of copper availability.[40,42] MMOs are so critical to the methanotroph lifestyle that they are naturally overexpressed: sMMO constitutes ~10% of the total cellular protein[160] under copper-starvation conditions, and pMMO represents ~20% of the total cellular protein[39] and 80% of the total protein in the membranes[206] under copper-replete conditions.

To accommodate such large quantities of pMMO, copper triggers the formation of intracytoplasmic membranes (ICMs) that fill the cell.[37] These methanotrophic ICMs, first detected more than 50 years ago,[17] have been imaged using electron[37,42,207,208] and fluorescence[209] microscopies, but their mechanism of biogenesis is not known. In addition, the arrangement of pMMO within the ICMs and the relationship between this environment and pMMO function remain unclear. Although negative-stain electron microscopy (EM) images of *Methylococcus capsulatus* (Bath) membrane preparations show tight packing of pMMO molecules,[210,211] pMMO has never been directly observed in ICMs within an intact cell.

Structural studies of pMMO have focused on a single biological assembly: a 300 kDa trimer comprising three copies each of subunits PmoA, PmoB, and PmoC. Crystal structures of detergent-solubilized pMMO from five different methanotrophs revealed the overall subunit folds and possible locations for the copper active site, but several transmembrane regions, including a highly conserved part of the PmoC sequence, were not observed.[59-63] This region was finally unveiled in recent single-particle cryo-electron microscopy (cryoEM) structures of pMMO embedded in native lipid nanodiscs, along with a previously-undetected copper site and new structural elements stabilized by lipids.[211] The methane oxidation activity of pMMO is also sensitive to solubilization from the ICMs. From whole cells to isolated membranes, catalytic activity decreases by 5-10 fold,[38] and upon solubilization in detergent, there is a further 10-fold reduction in activity[31] with no measurable activity for crystallized samples.[59] Some activity is recovered in lipid nanodiscs, allowing the cryoEM structure determination of enzymatically-active pMMO, but this recovered activity is less than that of isolated membranes and far below whole cell levels.[63,211] The inability to fully recover methane oxidation activity is potentially attributable to pMMO removal from the unique ICM environment.

In contrast to x-ray crystallography and single-particle cryoEM, cryo-electron tomography (cryoET) offers the opportunity to study pMMO in its most active state in the cell and in isolated ICMs, without perturbation by detergent solubilization or non-native environments. CryoET with subtomogram averaging (STA) combined with cryo-focused ion beam (cryoFIB) milling provides a powerful approach for studying molecular complexes *in situ*,[212,213] and has been applied successfully to a variety of intact bacterial cells and reconstituted bacterial systems,[214] achieving subnanometer resolution at best for integral membrane proteins.[215] In addition, the entire volume of a vitrified cell can be reconstructed at tens of nanometer resolution through Serial cryoFIB/SEM imaging.[216,217] Here we have used these techniques to investigate pMMO assembly and structure in intact *M. capsulatus* (Bath) methanotroph cells and isolated native membranes, as well as ICM biogenesis. The data indicate that the ICMs derive directly from the inner cell membrane, where pMMO assembles into an ordered hexagonal array. The cryoET STA structure of the pMMO trimer embedded in the ICM was determined to an unprecedented resolution of 4.8 Å resolution, and is consistent with the structure in native nanodiscs.[211] The observed higher-order assembly of pMMO trimers provides new insights into the high enzymatic activity of pMMO in native cells.

3.3. Results

3.3.1. Intracytoplasmic membrane formation in methanotrophs

To investigate ICM biogenesis, we vitrified *M. capsulatus* (Bath) cells grown in the presence and absence of copper and imaged them by serial cryoFIB/SEM for whole bacterial cell volumes. The reconstructed 3D volumes of intact cells show abundant ICM stacks in cells cultured in copper-containing media, but not in cells cultured without copper (Fig. 3.1A-C), consistent with previous observations[37,42,207-209]. We then used cryoFIB to create thin cell lamellae (< 200 nm) from plunge-frozen cells cultured in the presence of copper (Fig. 3.1D-G). Projection images of thin cell lamellae show extensive ICM stacks filled with pMMO particles, which appear like fine tooth combs when viewed along the membrane surface with the soluble domain facing the lumen (Fig. 3.1D and inset). In the reconstructed cryo-tomogram of the cell lamella, the outer membrane, peptidoglycan cell wall, and cytoplasmic membrane are distinct (Fig. 3.1E-F). The ICM vesicles appear separated from each other (Fig. 3.1E inset). There is a clear continuity from the cytoplasmic membrane to the ICM (Fig. 3.1E black arrows), indicating that the ICMs are derived from the cytoplasmic membrane. Moreover, a transition point where the membrane (with a rough periplasmic side) differentiates from the cytoplasmic membrane (displaying two leaflets of the bilayer) can be identified (Fig. 3.1E white arrowhead). These observations strongly support suggestions that ICMs form by invagination of the cytoplasmic membrane under copper-replete conditions.[157,209,218]

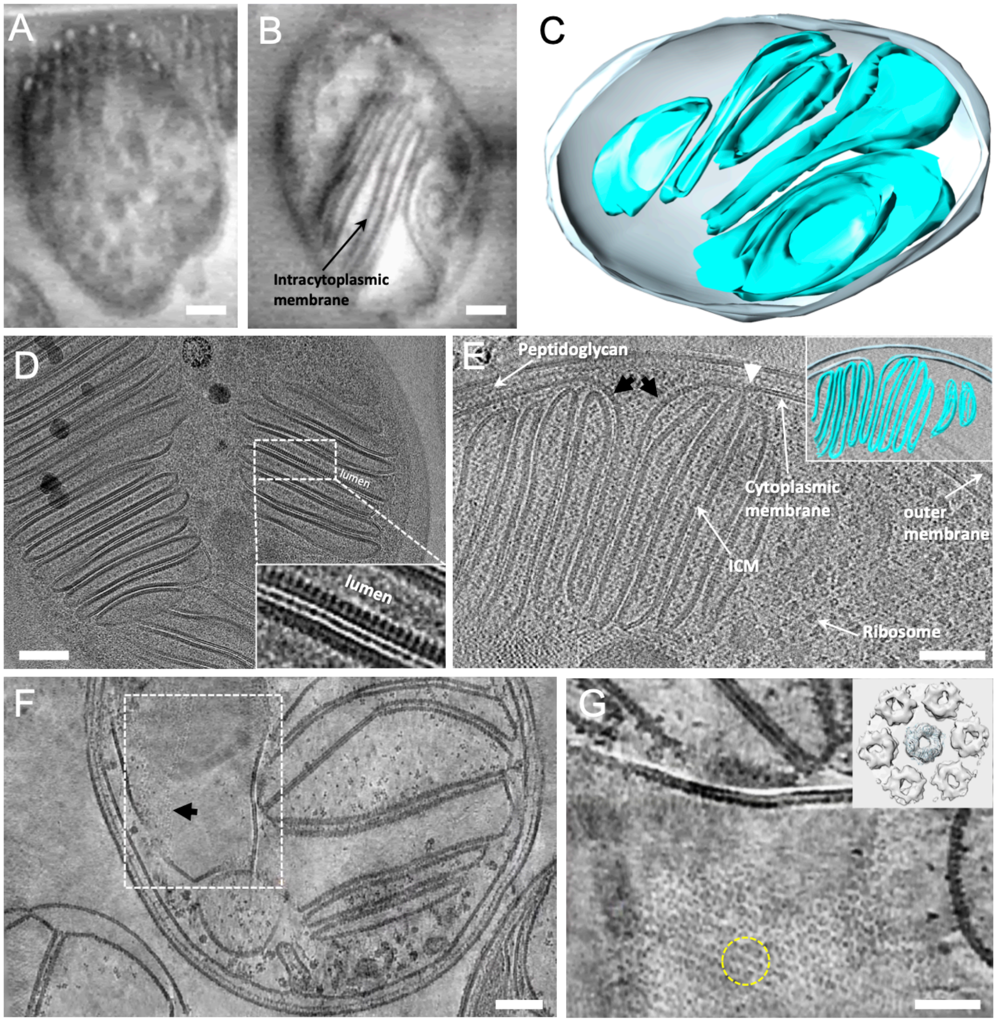

Figure 3.1. Copper-induced intracytoplasmic membranes of methanotrophic bacteria. (A-B) Representative slices from serial cryoFIB/SEM volumes of Bath cultured in medium containing 0 uM (A) or 25 uM (B) $CuSO_4$. (C) Membrane segmentation of the cell in (B). Cell membrane is shown in grey, intracytoplasmic membranes in cyan. (D) A projection image of cryoFIB lamella of Bath cultured in copper-containing medium. Inset, enlarged view of boxed area, displaying comb-like edge-on view of membrane-bound protein arrays. (E) An 8.5 nm thick tomographic slice of Bath cell lamella. Inner and outer cell membranes, peptidoglycan, intracytoplasmic membrane and ribosome are labeled. The inner cell membrane continues with intracytoplasmic membrane (black arrows), where the transition point is marked (white arrow). (F) A tomographic slice of Bath lamella, display an array of particles (black arrow). (G) An enlarged view of the boxed region in (F), tilted and rotated to show the face-on view of membrane-bound particles organized in a hexagonal lattice. Inset, a subtomogram average of the 7-particle volume (yellow circle). Scale bars, 200 nm in (A) and (B), 100 nm in (D) to (F), and 50 nm in (G).

3.3.2. Array formation of pMMO in membranes

While most lamellae display the cross-section of ICM vesicles (Fig. 3.1D-E), lamellae that were milled along the ICMs exhibit hexagonally ordered arrays of pMMO particles covering the whole membrane surface (Fig. 3.1F-G). Such extensive, well-ordered arrays within the intact cells have not been observed previously, though small partially ordered patches were found in the isolated *M. capsulatus* (Bath) membranes.[210] Extracting and aligning subtomogram volumes containing seven particles (Fig. 3.1G, dashed yellow circle) yielded a subtomogram average map at 15 Å resolution (Fig. 3.1G inset). The map reveals donut-shaped particles with a central donut surrounded by six equivalent neighbours. The central particle can be fitted well with the pMMO trimer crystal structure (PDB: 3RGB)[61] (Fig. 3.1G inset).

3.3.3. CryoET structure of pMMO in a membrane

To understand the molecular organization of the extended array, we isolated membranes from *M. capsulatus* (Bath) and carried out cryoET analysis. CryoEM projection images show that the membranes are densely packed with small ring-like particles similar to those observed in the intact cell (Fig. S3.1B), presumably pMMO trimers as the pMMO subunits are the main components in the sample (Fig. S3.1A) and the particle size and shape are consistent with the pMMO crystal and cryoEM structures. CryoET of these membrane vesicles reveals that the ring-like particles are organized into an ordered hexagonal array (Fig. 3.2A). The distance between two neighboring particles is ~10 nm, similar to the interparticle distance in the cell (Fig. 3.1G). Using a template containing seven pMMO particles (Fig. 3.2A, dashed yellow circle), the result of template matching by emClarity[219,220] reveals that more than 70% of membranes are covered by the hexagonal array of pMMO particles (Fig. S3.1C). Further subtomogram averaging resulted in a map at an overall resolution of 10 Å, where the central particle is well resolved (Fig. 3.2B) and fits the crystal structure of pMMO trimer neatly (Fig. 3.2C). In contrast to relatively equal quality among the seven particles derived from cell lamella (Fig. 3.1G inset), the central particle here is much better resolved than the surrounding six particles, indicating that the hexagonal lattice in these isolated ICMs is less well ordered compared to that in the intact cell.

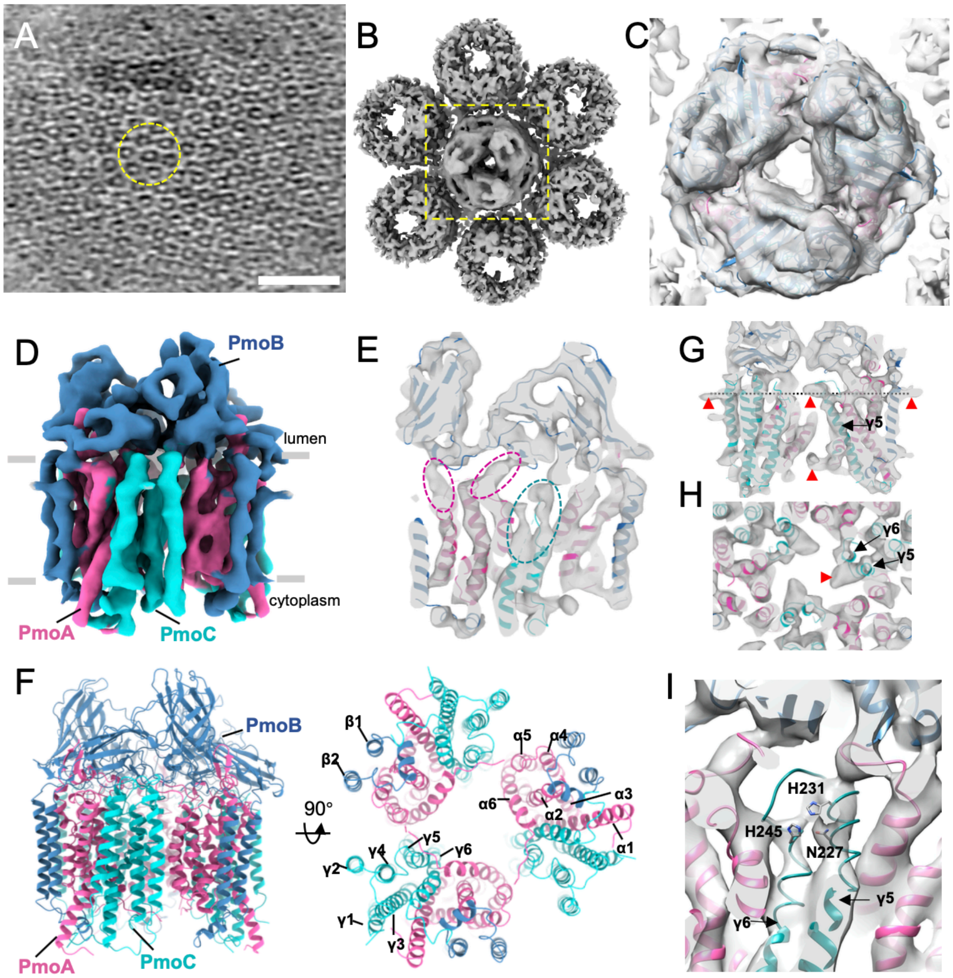

Figure 3.2. CryoET STA of native pMMO trimer from isolated intracytoplasmic membrane. (A) A tomographic slice of isolated intracytoplasmic membrane. Yellow dashed circle encloses a unit of 7 particles. (B) Subtomogram average of the 7-particle unit. (C) An enlarged view of the central particle in (B), superimposed with the docked crystal structure of pMMO trimer (PDB: 3RGB). (D) The pMMO trimer STA map at 4.8 Å resolution, with each pMMO monomer consisting of PmoA (pink), PmoB (blue) and PmoC (cyan). (E) A central slice view of pMMO map superimposed with pMMO crystal structure model. The dashed oval regions indicate the newly observed densities for PmoA (pink) and PmoC (cyan) that were not resolved in the previous crystal or cryoEM SPA structures of detergent solubilized pMMO. (F) Overall structure of active pMMO trimer embedded in native membrane, with PmoA, B and C coloured accordingly. Alpha helices of PmoA, PmoB and PmoC are labelled as α1-6, β1-2 and γ1-6, respectively. (G-H) Side and cross-sectional (at the plane indicated by the dotted line) views of the pMMO map, superimposed with the cryoEM pMMO nanodisc model (PDB 7SH4). Red arrowheads indicate extra densities that are not fitted with the model. (I) Three invariant residues, N227, H231 and H245, in the newly resolved highly conserved PmoC helices γ5 and γ6, potentially make up a new Cu-active site. Scale bars, 50 nm.

Previous structural studies of pMMO involved detergent solubilization steps that abolish or diminish activity, including purification in detergent for crystallization[59-63] and reconstitution of detergent-solubilized samples into lipid nanodiscs for cryoEM single particle analysis.[211] To investigate pMMO in its native environment without the use of detergent, we conducted cryoET STA of pMMO embedded within isolated *M. capsulatus* (Bath) membranes. We determined the structure of the pMMO trimer to 4.8 Å resolution (Fig. 3.2D, Fig. S3.2, Table S3.1), to our knowledge the highest resolution achieved to date for membrane embedded protein complexes by cryoET[215,221-225] (Table S3.2). The trimer architecture and folds of PmoA, PmoB, and PmoC resemble the previous crystal and cryoEM structures. Densities corresponding to regions of PmoA and PmoC not resolved crystallographically are apparent in the map (Fig. 3.2E, dashed ovals), including part of PmoA (Fig. 3.2E, dashed pink ovals) and segments of two highly conserved PmoC helices facing the interior of the trimer (M219 to L254) (Fig. 3.2E, dashed cyan oval). These regions were fully modelled in the recent cryoEM structure of pMMO in native nanodiscs,[211] which fits the cryoET STA map extremely well (Fig. 3.2F, Fig. S3.2). Several densities not accounted for by the pMMO model are also present and may correspond to more flexible loop regions or potentially lipids (Fig. 3.2G-H). The high resolution of the native nanodisc cryoEM structure (2.15 Å) also allowed the modelling of a copper site coordinated by PmoC residues Asn 227, His 231, and His 245[211]. Although the side chains are not resolved at 4.8 Å resolution, a density corresponding to the backbone helixes is present in cryoET STA map (Fig. 3.2I).

3.3.4. Biochemistry of array formation

CryoET of both cryoFIB milled and isolated membranes reveals that pMMO assembles into regular hexagonal arrays in the native membrane (Fig. 3.1G, Fig. 3.2A). Furthermore, when purified pMMO was reconstituted into lipid nanodiscs, we observed a substantial fraction of nanodiscs containing three pMMO trimers in samples that were optimized for formation of single pMMO trimer-containing nanodiscs (Fig. S3.4). These findings raise the key question of whether the pMMO higher-order array plays a role in driving ICM biogenesis and high pMMO activity in whole cells.[38] To investigate the relationship between array formation and methane oxidation, we formed arrays with native lipid nanodiscs and measured the resulting activity. Previous work with nanodiscs has shown that altering the ratio of lipid to membrane scaffold protein (MSP) can result in larger nanodiscs containing more than one enzyme per disc.[176,197] When we reconstituted pMMO into nanodiscs with a 1.5 x lipid:MSP ratio compared to the ratio optimized for single particle nanodiscs, we were able to separate nanodiscs of various sizes using size-exclusion chromatography (SEC) (Fig. 3.3A-B). The SEC fractions exhibited decreasing size with elution volume, with the single particle nanodiscs measuring ~100 Å by dynamic light scattering (Fig. 3.3C) as expected based on the cryoEM single particle structure.[211] Small partially ordered patches of pMMO assemblies were observed by negative stain EM (Fig. 3.3A). Interestingly, the SEC fractions corresponding to the larger nanodisc arrays exhibited up to 3-fold the methane oxidation activity of the single particle nanodiscs, reaching activity levels close to that of pMMO in isolated membranes (Fig. 3.3D). These observations support the idea that pMMO activity is enhanced by array formation.

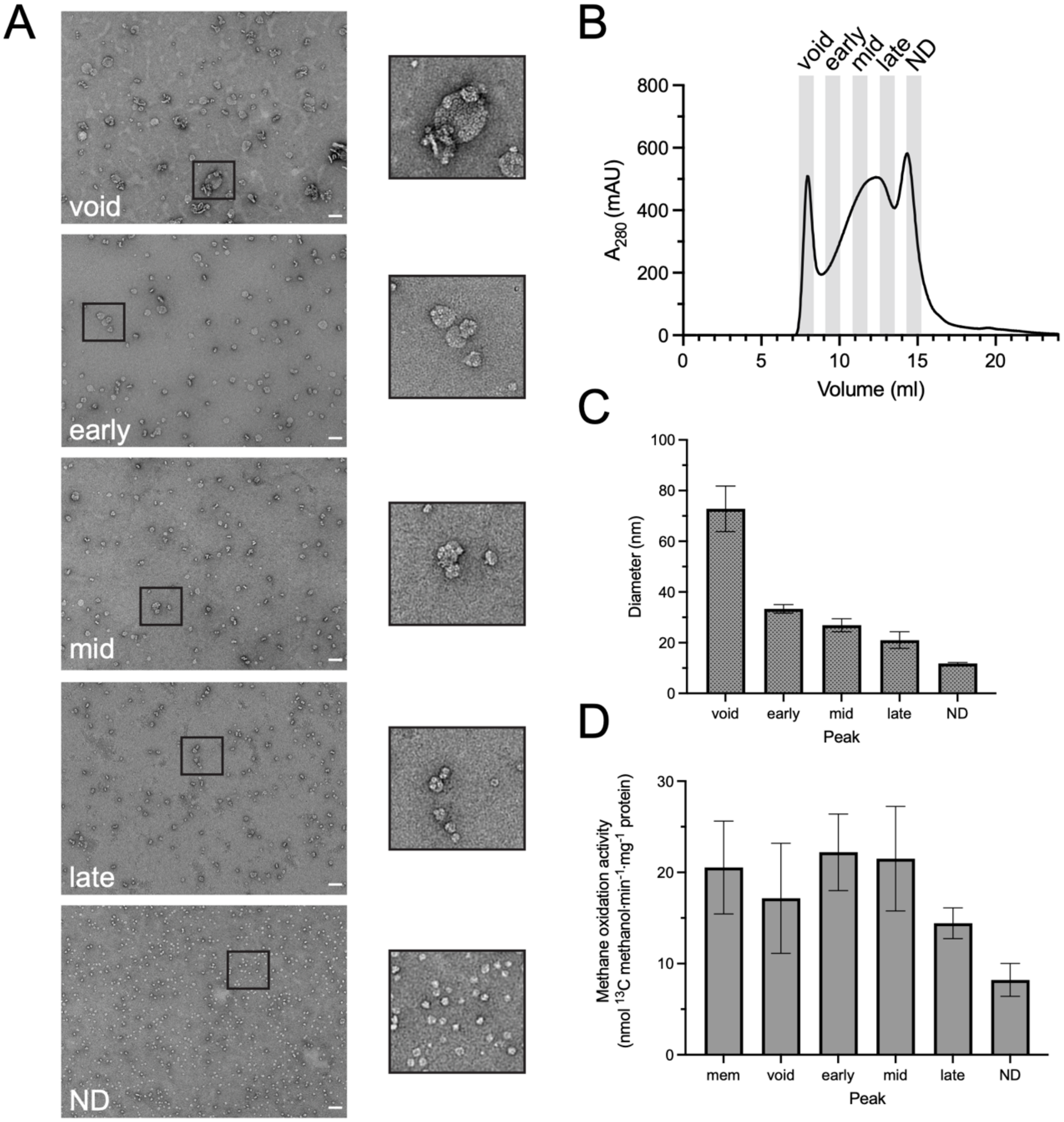

Figure 3.3. Methane oxidation by pMMO reconstituted in lipid nanodiscs. (A) Representative images and enlarged views of the boxed area from elution fractions of pMMO nanodisc size-exclusion column. (B) The elution profile of pMMO nanodisc from a Superose 6 size-exclusion column. The fractions collected are indicated. (C) Size distribution of pMMO nanodiscs, as measured by the diameter by dynamic light scattering. (D) pMMO specific activities measured from each fraction and from isolated membranes. Scale bar, 50 nm

3.3.5. Mediation of pMMO array

To further investigate array formation, we focused our cryoET STA analysis on the inter-trimer interface (Fig. 3.4A), obtaining a 12 Å resolution STA map into which three pMMO trimers were fit well using rigid-body docking (Fig. 3.4B-C). We then carried out all-atom molecular dynamics simulations to identify specific residues mediating trimer-trimer interactions. For this purpose, we constructed a 2 × 2 lattice patch containing four pMMO trimers (Fig. 3.4D), utilizing periodic boundary conditions to mimic the symmetry of the extended pMMO array. The simulation showed several interactions between the PmoB soluble domains of adjacent pMMO trimers, including a strong salt bridge interaction between K60 and E338 (Fig. 3.4E) as well as more transient interactions involving residues K58/E160 and R167/D339 (Fig. 3.4F). No interactions were observed within the transmembrane domains of PmoA, PmoB, or PmoC, suggesting the inter-trimer interactions responsible for array formation are primarily mediated by the PmoB soluble domains.

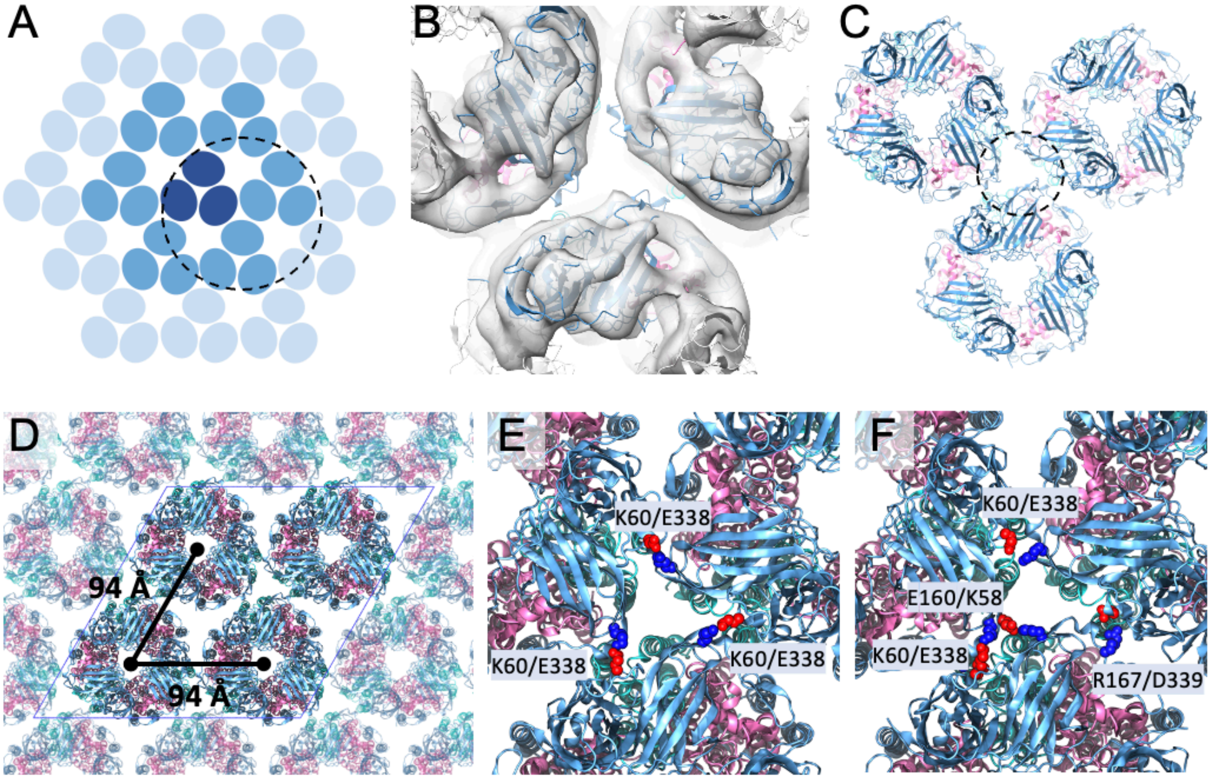

Figure 3.4. Higher-order assembly of pMMO trimers. (A) A schematic of pMMO trimer hexagonal array. Each blue oval represents a pMMO monomer consisting PmoA, B and C. The central pMMO trimer (dark blue), together with 6 surrounding trimers (medium blue), represent the 7-particle unit shown in Figure 1G and Figure 2B. (B) CryoET STA of the subvolumes enclosing an inter-trimer interface, shown as circled unit in (A), superimposed with docked pMMO model. (C) Structural model of pMMO trimer assembly. The inter-trimer interaction is mediated by PmoB (blue), shown in the dashed circle. (D) Molecular model of the extended pMMO trimer hexagonal array, with a 94 Å inter trimer distance. The four-trimer system used for MD simulation is shown in opaque colours with the simulation box bounded by a blue rhombus and periodic pMMO trimer images shown as transparent. PmoA, B and C colours are as in Figure 3. (E-F) Interactions between the neighboring pMMO trimers, mediated by pairs of charged residues, K60/E338, K58/E160, and R167/D339, as indicated.

3.4. Discussion

Recent work has shown that a thorough understanding of pMMO function requires studying it in as close to the native lipid environment as possible.[63,71,211] Our cryoET STA investigation of pMMO in intact cells and isolated membranes reveals that pMMO forms hexagonally ordered arrays in ICMs that derive directly from the inner cell membrane. Formation of these arrays, which are possibly stabilized by salt-bridge interactions between PmoB subunits, correlates with increased methane oxidation activity, explaining in part why pMMO activity decreases substantially upon disruption of the membranes by detergent solubilization and cannot be fully recovered in single particle native lipid nanodiscs.[211] *In vitro*, the arrays might enhance activity by increasing solubility of methane, oxygen, and the duroquinol reductant used in the assay. In the cell, formation of dense pMMO arrays in the inner membrane might trigger ICM formation and serve to exclude other enzymes from the respiratory pathway from the ICMs. The arrays might also facilitate recruitment of periplasmic methanol dehydrogenase (MDH) to more efficiently link methane oxidation by pMMO to the next step in the metabolic pathway, methanol oxidation to formaldehyde by MDH.[98,99] Understanding how pMMO arrays assemble and promote methane oxidation will be integral to future efforts to deploy methanotrophs in biotechnology.

3.5. Methods

3.5.1. Cell culture and membrane isolation

Copper-replete *Methylococcus capsulatus* (Bath) was cultured in a 12 L reactor with a continuous flow of 1:3 methane:air at 1 L/min and 45 °C. The culture was grown as described previously in nitrate mineral salts (NMS) buffer containing KNO_3, $MgSO_4 \cdot 7H_2O$, $CaCl_2 \cdot 2H_2O$. 3.9 mM phosphate buffer, pH 6.8, trace element solution, 80 μM NaFeEDTA, and 50 μM

$CuSO_4{\cdot}5H_2O$.[59] Cells were grown to an OD_{600} of 7.0, harvested by centrifugation at 5000 x g for 10 minutes, flash-frozen, and stored at -80 °C.

Copper-starved *M. capsulatus* (Bath) was first grown in 50 ml cultures for 2 weeks with 10 μM $CuSO_4$ and then passaged into another 50 ml culture for 2 weeks at 0.5 μM $CuSO_4$. This culture was then used to inoculate a 3 L bioreactor culture with 0 mM $CuSO_4$ for 1 week until OD_{600} of 5.0 was reached. Cells were harvested as described above, flash-frozen, and stored at -80 °C.

To isolate membranes, cells were thawed in buffer containing 25 mM PIPES, pH 7.3, 250 mM NaCl with DNase and protease inhibitor cocktail (Roche). The cells were sonicated on ice for 10 min at 40 % amplitude with 1 s /1 s on/off pulses (Qsonica 700). The lysate was centrifuged at 20,000 x g for 45 min followed by collection of the soluble fraction and centrifugation at 140,000 x g for 1 h at 4 °C to isolate the membranes. The isolated membranes were washed with 40 ml of the same buffer, passing through a Dounce homogenizer before centrifuging again. This step was repeated for a total of three washes. After the final spin, membranes were resuspended in 8 ml of the same buffer, aliquoted, and flash frozen. The protein concentration in the membranes was measured by DC Lowry assay (Bio-Rad).

3.5.2. pMMO solubilization, nanodisc reconstitution, and activity measurements

pMMO was isolated from membranes using n-dodecyl-β-D-maltoside (DDM) mixed with the membranes at a 1.2:1 mg:mg ratio at 4 °C for 1 h. The mixture was then centrifuged at 140,000 x g to separate out the insoluble portion. Solubilized pMMO was concentrated and exchanged into buffer containing 25 mM PIPES. pH 7.3, 250 mM NaCl, 0.02% DDM. The protein concentration was measured using the DC-Lowry assay (Bio-Rad).

To form nanodiscs of various sizes, pMMO was mixed with lipids isolated from the native organism and membrane scaffold protein (MSP1E3D1), both prepared as described previously.[211] A ratio of 1:2:120:240 pMMO:MSP:lipid was used to generate these nanodiscs; a larger amount of lipid than necessary was used to ensure formation of homogeneous nanodiscs. The mixture was rotated end-over-end at 4 °C for 15 min along with 20 mM sodium cholate before adding 0.8 mg/ml SM-2 Bio-Beads (Bio-Rad). After 2 h, bio-beads were removed using a syringe filter and the formed discs were purified using a Superose 6 column (Cytiva). Fractions were collected from the void, early, mid, late, and nanodisc (ND) peaks for further characterization (Fig 3.3).

Dynamic light scattering analysis of fractions was performed with a Punk instrument (Unchained Labs), analyzing 5 µl of sample over 10 s with five repeats per sample. Negative-stain samples were prepared by applying 3 µl sample onto a 400-mesh copper grid. Grids were washed for two rounds of 15 s with water and two rounds of 30 s with 1% uranyl formate. Grids were then blotted and allowed to dry. Images were collected on a JEM-1400 microscope (JEOL) at 30000x magnification at 3.71 Å pixel size using Leginon software.

Activity assays were carried out by adding 100 µl sample to a screw-top vial, adding an excess amount of duroquinol, removing 1 ml headspace, adding 1.5 ml ^{13}C-methane and shaking at 45 °C for 5 min. Negative control reactions were performed omitting enzyme, duroquinol, and methane. Reactions were stopped by storing at -20 °C. To analyze the methanol produced by the reactions, the samples were thawed and 500 µl chloroform with 1 mM dicholoromethane was added to each sample as an internal standard. Samples were shaken at 2000 rpm at 4 °C for 10 min followed by centrifugation at 2000 x g for 10 min at 4 °C. Samples were then analyzed for [^{13}C]-methanol concentration using an Agilent 7890B/5977A MSD GC/MS instrument with a PoraBOND Q column (25 m x 250 µm x 3 µm) according to previous methods.[63,71] The [^{13}C]-

methanol peak was integrated, compared to a standard curve, and normalized to the concentration of dichloromethane.

3.5.3. CryoET sample preparation

For *M. capsulatus* (Bath) bacteria, the cells were diluted to an OD_{600} of 2 with NMS buffer. Quantifoil grids (300 mesh, Cu R2/1) were glow-discharged for 45 s. Four microliters of the sample were added onto the carbon side of the grid, which were blotted from the mesh side for 10 s before plunge freezing into liquid ethane with a Leica GP2 (Leica Microsystems). The humidity was set to 100% and the temperature was set to 15 °C during blotting.

For the isolated *M. capsulatus* (Bath) membranes, a 5 mg/ml stock membrane solution was diluted to 1.25 mg/ml with buffer containing 25 mM PIPES, pH 7.3 and 250 mM NaCl, and mixed with 6 nm gold beads before plunge-freezing. Lacey carbon-coated copper grid (300 mesh, Agar Scientific) was glow-discharged for 45 s. 3 µl sample were added onto the carbon side of the grid, and the grid was blotted for 3.5 s with a blotting force of -15 before plunge freezing into liquid ethane using a Vitrobot (Thermo Fisher Scientific). The humidity was set to 100% and the temperature was set to 4 °C during blotting.

3.5.4. Serial CryoFIB/SEM

(3.5.4 – 3.5.9 were conducted by Y. Zhu, C. K. Cassidy et al.)

Samples were imaged on a ZeissCrossbeam 550XL (Carl Zeiss Microscopy, LLC), fitted with a Quorum transfer station and cryo-stage (Quorum Technologies). They were mounted on a Quorum-compatible custom sample holder and coated with Pt for 60 s at 10 mA on the Quorum transfer stage, before loading on the cryo-stage. The stage temperature was set at -165 °C, while the anticontaminator was held at -185 °C. Samples were imaged at 45° tilt after being coated again with Pt for 2x 30s using the FIB-SEM's internal GIS system, with the Pt reservoir held at 25 °C.

Initial trapezoid trenches were milled at 30kV 700 pA over 8.5 μm to reach a final depth of 3.5 μm, without a further polishing step. Serial sectioning and imaging acquisition was performed as follows: for high Cu samples, FIB milling was performed using the 30 kV 50 pA probe, while for low Cu samples, it was done at 30kV 20pA, and both were acquired with a z-slice step of 10 nm and a depth of 3.5 μm over the entire milling box of 8 × 8 μm; SEM imaging was performed at a pixel depth of 2048 x1 536 pixels, which resulted in a pixel size of 5 nm, with the beam set at 1.5kV 20pA, dwell time 50 nsec and scan speed 0, averaging the signal over 100 line scans as a noise-reduction strategy.

3.5.5. CryoFIB milling for lamella preparation

Lamella preparation of *M. capsulatus* (Bath) was performed using a Scios DualBeam cryoFIB/SEM (Thermo Fisher Scientific) equipped with a PP3010T transfer system and stage (Quorum Technologies) using the xT v7.6 software (Thermo Fisher Scientific). Grids were sputter coated with Pt within the PP3010T transfer chamber maintained at -175 °C. After loading onto the Scios stage at -168 °C, the grids were inspected using the SEM (operated at 5 kV and 13 pA). The grid surface was coated using the gas injection system trimethyl (methylcyclopentadienyl) platinum (IV) (Thermo Fisher Scientific) for 4 s, to give a thickness of ~3 μm. Milling was performed using the ion beam operated at 30 kV and currents decreasing from 300 to 30 pA. At 30 pA, lamella thickness was thinned to < 200 nm. During the final stage of milling, SEM lamella inspection was conducted at 2 kV and 13 pA.

3.5.6. CryoET data collection

For isolated membranes, cryoET tilt series were acquired using a Thermo Fisher Titan Krios operated at 300 keV equipped with a Gatan Quantum post-column energy filter (Gatan Inc) operated in zero-loss mode with 20 eV slit width, and Gatan K3 direct electron detector in eBIC (electron BioImaging Centre, Diamond). Tilt series were collected with SerialEM[226] with a nominal magnification of 64k and a physical pixel size of 1.34 Å per pixel. They were acquired using dose-symmetric tilt-scheme[227] starting from 0° with a 3° tilt increment by a group of three and an angular range of ± 63°. The accumulated dose of each tilt series was around 129 $e^{-}/Å^{2}$ with a defocus range between -2.5 and -6 µm. Ten frames were saved in each raw tilt image. Details of data collection parameters are listed in Table S1.

For cell lamellae, cryoET tilt series were collected with SerialEM[226] with a nominal magnification of 42k and physical pixel size of 2.13 angstrom per pixel. They were acquired usng dose-symmetric tilt-scheme[227] starting from 0° with a 3° tilt increment by a group of three and an angular range of ± 54°. The accumulated dose of each tilt series was around 111 $e^{-}/Å^{2}$ with a defocus range between -3.5 and -6 µm. Ten frames were saved in each raw tilt image.

3.5.7. CryoET data processing and subtomogram averaging

The automated cryoET pipeline developed in-house was used for initial tomograms (https://github.com/ffyr2w/cet_toolbox) through performing motion correction[228] of the raw frames, tilt-series alignment and final reconstruction with IMOD.[229] Suitable tilt series were selected. For isolated membranes, the fiducial markers were manually inspected to ensure the centering of predicted markers for each tilt series in eTOMO. For cell lamellae, a fiducial-less tilt-series alignment was performed by using AreTomo.[230]

Subtomogram averaging from the isolated intracytoplasmic membranes was performed following the workflow of emClarity.[219,220] The pMMO trimer crystal structure (PDB 3RGB)[61] was low-pass filtered to 30 Å and used as the initial template for template search. A small dataset of 10 tilt series was used for template search with 4x binned tomograms with a pixel size of 5.36 Å. About 2,000 subtomograms were selected based on their initial positions and orientations in the membrane. Subtomogram averaging and alignment were performed with a volume including 7-pMMO particles. After several refinement cycles, the density map with 7-pMMO was obtained.

A further 127,417 subtomograms were selected from the entire dataset of 187 tilt series. The subtomogram averaging and alignment were performed iteratively using 3x and 2x binned tomograms. A cylindrical alignment mask including one pMMO particle and a 3-fold symmetry were used throughout the alignment procedure. We converted the coordinates from emClarity to Relion-4.0[231] for Relion 3D refinement in bin3 (4.02 Å pixel size) and bin2 (2.68 Å pixel size). The final density map was reconstructed at bin 1 with Relion-4.0[231] and sharpened with a b-factor of -50.

For the three-trimer subtomogram averaging, the orientations for each particle from the above step was kept and the position shifted to the centre of three trimers. A cylindrical alignment mask including the central 3 trimers and a 3-fold symmetry were used for additional averaging and alignment in bin 2 (2.68 Å pixel size) in Relion-4.0.[231]

Subtomogram averaging of pMMO from lamellae was processed similarly as the isolated intracytoplasmic membranes using emClarity[219,220]. A template search using the 7-particle reference was carried out in 4x binned tomograms with a pixel size of 8.52 Å for the thin lamellae. A total of 500 subtomograms were selected based on their initial positions and orientations in the intracellular membranes. The subtomogram averaging and alignment were performed iteratively using 3x and 2x binned tomograms, with pixel sizes of 6.39 Å and 4.26 Å. respectively. A cylindrical alignment mask and a 3-fold symmetry were applied throughout the alignment procedure. The final density map was reconstructed at bin 2 with emClarity.

3.5.8. Model building and refinement and analysis

A starting model of the pMMO trimer was constructed by rigid-body docking the cryoEM SPA structures of PmoA, PmoB and PmoC from pMMO nanodiscs (PDB 7S4H)[211] into our cryoET STA map using Chimera.[232] A model of the extended pMMO array was constructed by hexagonally tiling the pMMO trimer using a lattice constant of 9.4 nm as determined from the subtomogram average of three pMMO trimers (Fig. 4B-C). A four-trimer region was then manually embedded in a lipid bilayer constructed and equilibrated using CHARMM-GUI[233] and containing 57% PVPE, 18% PVPG, 16% PVPC, and 9% cardiolipin[234] and subsequently solvated with TIP3P water and 150 mM NaCl using VMD v1.94.[235]

3.5.9. Molecular dynamics simulations

All-atom molecular dynamics simulations were carried out using NAMD v2.14[236] and the CHARMM36 force field.[237] The four-trimer hexagonal patch was first subjected to a series of conjugant gradient energy minimizations followed by a 10-ns equilibration simulation with backbone restraints and finally a 100-ns production simulation without restraints. Simulations were conducted in the NPT ensemble with conditions maintained at 1 atm and 310 K using the Nosé–Hoover Langevin piston and Langevin thermostat respectively. The r-RESPA integrator scheme was employed with an integration time step of 2 fs and SHAKE constraints applied to all hydrogen atoms. Short-range, nonbonded interactions were calculated every 2 fs with a cut-off of

12 Å; long-range electrostatics were evaluated every 6 fs using the particle-mesh-Ewald method. Periodic boundary conditions were appropriately chosen to permit the protein to interact with its periodic image in the x-y plane, mimicking the molecular interactions within the extended hexagonal array.

CHAPTER 4: Cell-free expression of particulate methane monooxygenase

This work is in preparation as:

Koo, C. W.; Jewett, M. C.; Rosenzweig, A. C.

4.1. Abstract

Particulate methane monooxygenase (pMMO) is a multi-subunit membrane metalloenzyme used by methanotrophic bacteria to convert methane to methanol. A major hurdle in pMMO research has been the lack of a recombinant expression system, precluding investigation of individual residues by mutagenesis and hampering a complete understanding of its mechanism. Here, we develop an *Escherichia coli* lysate-based cell-free protein synthesis (CFPS) system that can be used to express pMMO in vitro in the presence of detergents, bicelles, and nanodiscs. We used a SUMO fusion construct to generate the native PmoB subunit and demonstrate that the SUMO protease (Ulp1) cleaves the protein in the reaction mixture. Using an affinity tag to isolate the complete pMMO complex for the first time, we show that the complex forms without the need for traslocon machinery or chaperones, confirmed by negative stain electron microscopy. This work demonstrates the potential for using CFPS to express complex membrane-bound metalloenzymes directly into lipids or detergents.

4.2. Introduction

Emissions of methane, the second-most important greenhouse gas after carbon dioxide, have been increasing rapidly over the past two decades.[1] Methane is a short-lived but potent greenhouse gas with 84 times the global warming potential as carbon dioxide over a 20 year period.[238] Due to this potency, even modest reductions of methane emissions represents a near-term opportunity to fight rapid global warming.[239]

Methanotrophs, bacteria that metabolize methane, provide a promising solution to this issue.[11,240] They are found in a wide variety of environments and have the unique ability to aerobically convert methane to methanol at ambient temperature and pressure.[14] To break the C-

H bond in methane (105, kcal), they use metalloenzymes called methane monooxygenases (MMOs). There are two types of MMOs used by methanotrophs: An iron-dependent, soluble MMO (sMMO) expressed under low copper conditions by some methanotroph species[30,241] and a copper-dependent membrane bound particulate MMO (pMMO) produced by nearly all methanotrophic species under copper-replete conditions.[31,72] While sMMO has progressed to the level of trapping reaction intermediates,[140] identifying substrate pathways,[131] and characterizing the role of regulatory subunits,[109] progress in understanding pMMO has been comparatively slow due to the inherent difficulties in studying membrane proteins.[173] Multiple copper binding sites,[62,71,181] strictly conserved amino acid resides,[78,173] and stabilized lipids within the structure have been identified,[63,211] but the location of methane oxidation and roles of conserved residues have yet to be definitively determined. A recombinant system for expressing pMMO mutants would address one of the major hurdles in pMMO research efforts by providing a system for probing individual residues and defining their role in methane oxidation.

Recombinant overexpression of membrane proteins can be difficult due to misfolding, aggregation, disruption of the host's membrane environment, and subsequent suppression of gene expression by the host.[242-244] pMMO has the added challenges of requiring proper copper loading for activity and being a multi-subunit complex formed from subunits PmoA (β), PmoB (α), and PmoC (γ), arranged in a $(\alpha\beta\gamma)_3$ formation.[59,211] Cell-free protein synthesis (CFPS) is a recombinant expression platform that addresses these difficulties.[245-247] *Escherichia coli* lysate-based CFPS isolates the transcription and translation machinery from the cell and in doing so, decouples protein synthesis from normal cellular function, preventing any inhibition or modification that the cell may impose on an otherwise cytotoxic protein of interest. The removal of the cell barrier creates an open, tunable reaction mixture that be advantageous for membrane protein expression and can be modified to suit pMMO expression.[248-251] Membrane mimetics such as liposomes, nanodiscs, bicelles, and detergent are provided in the reaction, allowing direct expression of pMMO into a membrane environment.[252-254] The system can also tolerate copper sulfate for loading metalloenzymes[255] and has the benefit of being able to engineer affinity tags onto the pMMO subunits. In this study, membrane mimetics, fusion protein constructs of pMMO and gene arrangements of the pMMO subunits are tested to establish the first CFPS-based multi-subunit membrane metalloenzyme expression system. Cryogenic electron microscopy is used to characterize the resulting complex.

4.3. Results

4.3.1. Initial expression and membrane mimetic test

Membrane mimetics were tested for their ability to solubilize the pMMO subunits from *Methylococcus capsulatus* (Bath). Previous studies demonstrated that nanodiscs and bicelles restore activity to pMMO.[63,211] CFPS studies have successfully used both nanodiscs and bicelles to solubilize membrane proteins and the concentrations used here, 1 mg/ml POPC nanodiscs and 1% DMPC bicelles, are based on those studies.[256-258] Each subunit was expressed individually and in combination in the presence of each membrane mimetic. PmoA and PmoC show soluble expression in the presence of nanodiscs (Fig. 4.1), indicating that the subunits can insert into the nanodiscs without any additional chaperones such as translocon machinery.[259,260] PmoB also had some soluble expression, but exhibited slightly worse soluble expression than the fully transmembrane subunits PmoA and PmoC. When all three subunits were expressed in the same reaction, PmoB soluble expression improves to similar levels as PmoA and PmoC. The use of bicelles reduced total expression by ~25% and only resulted in minimal soluble expression. On the basis of these expression profiles, nanodiscs were used for further experiments.

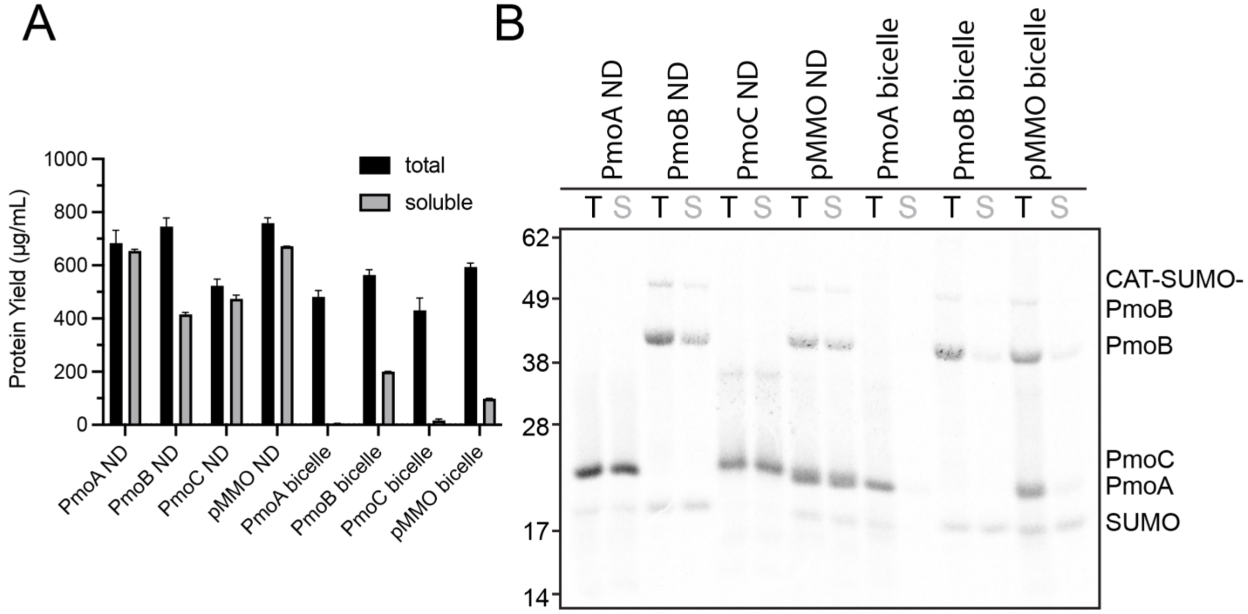

Figure 4.1. Cell free expression of pMMO subunits using nanodiscs and bicelles. (A) Total and soluble expression of each subunit individually and all subunits in combination using bicelles or nanodiscs (ND) as a membrane mimetic, n = 3 replicates. (B) Autoradiogram of total (T) and soluble (S) expression for each reaction detecting protein bands labeled with ^{14}C-leucine. MW markers (SeeBlue prestained marker, Thermo Fisher) are based on the equivalent SDS-PAGE gel.

4.3.2. SUMO protease (Ulp1) cleavage

M. capsulatus (Bath) PmoB includes a 32-residue N-terminal signal sequence that shuttles the soluble domain to the periplasm and is removed by an endogenous protease.[57] This cleavage generates a free amino group of the new N-terminal residue, His 33. The amino group, along with its side chain imidazole group and those of residues His 137 and His 139, coordinates a copper ion (Cu_B).[211,261] To mimic signal peptide cleavage and ensure proper formation of the Cu_B site, an N-terminal SUMO-PmoB fusion protein was generated to be cleaved by SUMO protease (Ulp1) (Fig 4.2A). Ulp1 protease has the advantage of cleaving at the c-terminus of the SUMO fusion protein, leaving no exogenous residues on the cleaved PmoB subunit [262]. To address the lower expression of PmoB compared to the other two subunits (Fig 4.2B), the sequence Met-Glu-Lys-Lys-Ile was added to the N-terminus of the SUMO tag [263,264]. This sequence, derived from chloramphenicol acetyltransferase (CAT), is commonly used to enhance CFPS expression (Fig 4.2A). Reactions including PmoA and PmoC with CAT-SUMO-PmoB showed equimolar expression of the three subunits (Fig 4.2C). Furthermore, the SUMO tag was cleaved successfully in the reaction, generating the native N-terminus of PmoB (Fig. 4.2C).

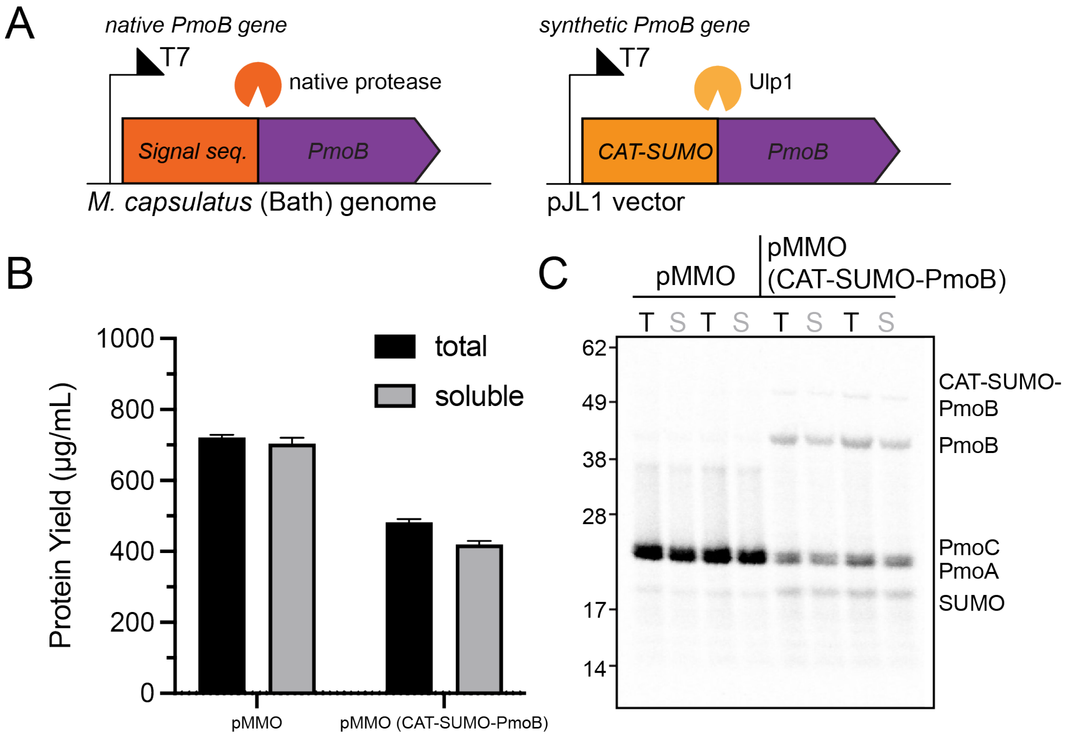

Figure 4.2. Cell free expression of pMMO subunits using CAT-SUMO-PmoB. (A) Total and soluble expression of each subunit individually and all subunits in combination using bicelles or nanodiscs (ND) as a membrane mimetic, n = 3 replicates. (B) Autoradiogram of total (T) and soluble (S) expression for each reaction detecting protein bands labeled with ^{14}C-leucine. MW markers (SeeBlue prestained marker, Thermo Fisher) are based on the equivalent SDS-PAGE gel. Note that the PmoB subunit here is a SUMO fusion protein in order to generate the native N-terminus of the subunit (vide infra).

4.3.3. Copper toleration

pMMO contains up to four copper binding sites and copper is essential for activity.[62,211] While the roles of each site in methane oxidation are not fully established, previous studies have shown that copper is necessary to recover pMMO activity after metals removal. The methanotroph genome encodes genes for special machinery to import copper and maintain high level of intracellular copper.[265] To provide copper for these sites copper was titrated into the CFPS reaction and expression of the pMMO subunits was measured. Total expression begins to decrease with the inclusion of 150 µM $CuSO_4$, is reduced by ~50% at 500 µM $CuSO_4$, and is abolished at 1 mM $CuSO_4$. Soluble expression, however, is only modestly decreased at 250 µM $CuSO_4$, consistent with previous work investigating copper tolerance for CFPS expression of a multicopper oxidase.[255] Therefore, 200 µM $CuSO_4$ was included in each subsequent reaction. Interestingly, SUMO cleavage is almost completely inhibited at 500 µM $CuSO_4$.

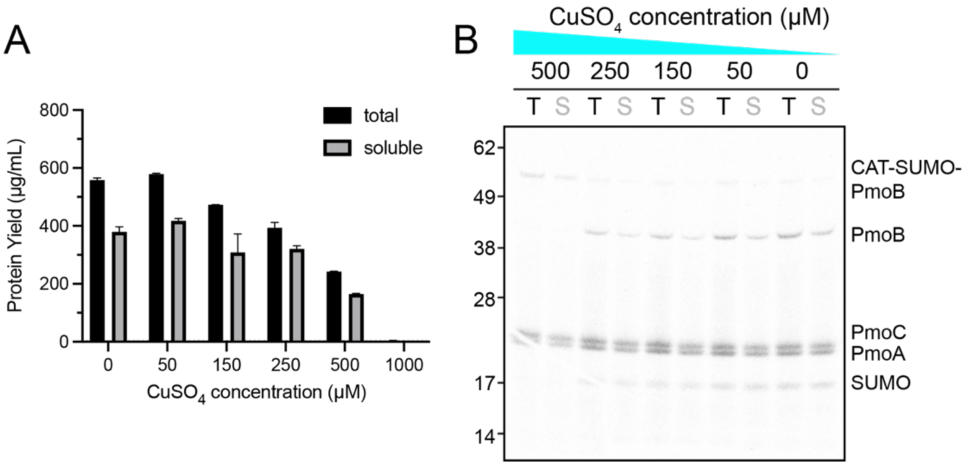

Figure 4.3. Copper sensitivity of pMMO CFPS reaction. (A) Total and soluble expression of pMMO with increasing amounts of $CuSO_4$, n = 3 replicates. (B) Autoradiogram showing the relative expression of pMMO subunits with increasing copper concentration. Molecular weights are marked according to the position of the SeeBlue (Thermo Fisher) markers (fig S4.1).

4.3.4. Multi- vs single-plasmid approach

In the *M. capsulatus* genome, the pMMO subunit genes are organized in an operon as *pmoCAB* with a promoter identified upstream of *pmoC*. To replicate this arrangement, a single plasmid containing the genes is this order was designed. In an initial experiment, protein expression decreased along the transcript: PmoC expressed well, but there was only a small amount of PmoA expression and no PmoB expression (Fig S4.2A). To improve expression of PmoA and PmoB, T7 promoters were added to each gene by switching from the pJL1 vector to the pCDF-Duet backbone with a third multiple cloning site included and the CAT sequence appended to the PmoB N-terminus. This approach increase the expression of PmoB relative to PmoA and PmoC (Fig S4.2B). The CAT sequence was added to the N-terminus of all three genes (Fig 4.4A), and the resultant construct was then tested using multiple different membrane mimetic conditions. Nanodiscs provided the best total and soluble expression of pMMO (Fig 4.4B) with expression of each subunit and effective SUMO cleavage (Fig 4.4C). This optimized single-plasmid approach was then used for protein isolation.

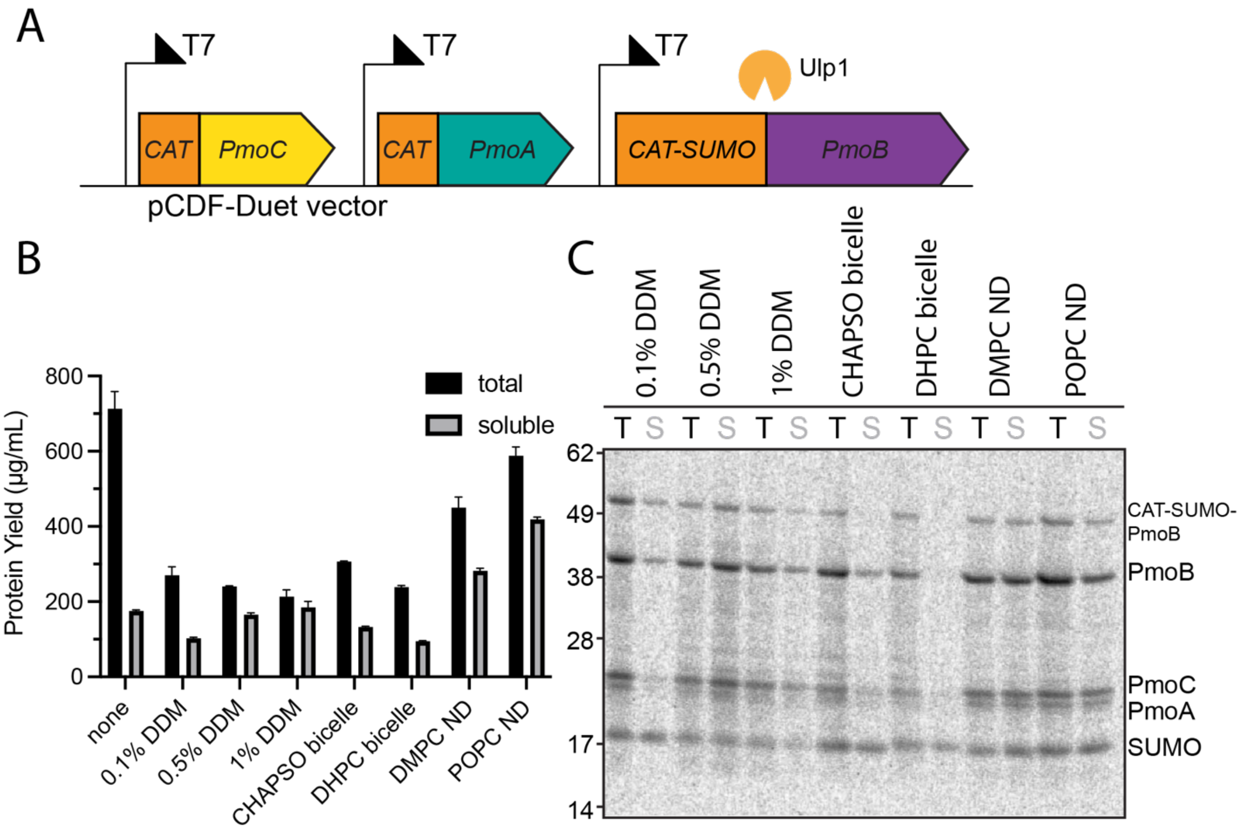

Figure 4.4. Polycistronic DNA and a screen of membrane mimetics. (A) Arrangement of pMMO subunits in the pCDF-Duet vector, mimicking the native arrangement in the genome. (B) Total and soluble protein expression in detergents, bicelles, and nanodiscs. n = 3 replicates. (C) Corresponding autoradiogram showing the relative expression of each pMMO subunit.

4.3.5. Tagging subunits and isolation from CFPS

A major benefit of using CFPS for pMMO expression is the ability to add affinity tags to the subunits for purification. The C-termini of PmoA and PmoC face the cytoplasm and are relatively flexible,[59,61] providing promising sites for affinity tags. The C-terminus of PmoB is periplasmic and is folded into a beta sheet making it possible that an affinity tag might disrupt the folding or complex assembly at this location. However, since the N-terminus is unavailable due to the signal peptide and the necessity to leave His33 unmodified, a C-terminal tag was tested for PmoB as well.. The Strep-tag II was used since this purification normally results in less contaminants from the affinity purification step. Reactions were scaled up from 30 ul to >500 ul for these tests and conducted in a sealed 6-well culture plate rather than a 1.5 ml microfuge tube[266]. The elution fractions off of the affinity column (Cytiva) showed that PmoC-Strep pulled down the other two subunits and the membrane scaffold protein, suggesting that the three subunits form a complex in a nanodisc (Fig 4.5). The PmoA-Strep and PmoB-Strep constructs failed to pull down the other subunits. This may mean that the PmoA Strep tag is inaccessible and the PmoB Strep tag disrupts either its folding or its complex formation. The PmoC-Strep construct was used for further experiments.

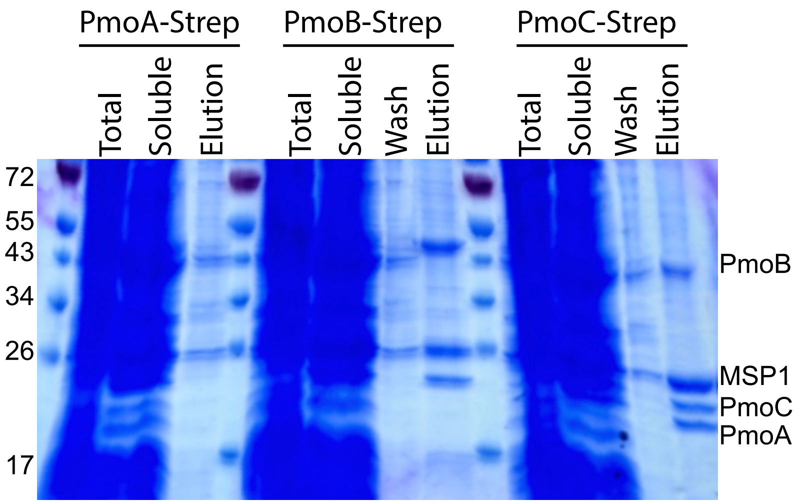

Figure 4.5. Tagging pMMO subunits. Reactions were run with plasmids for each subunit and C-terminal tagging of each subunit was tested. Protein was then isolated using a StrepTactin column. Gel shows total and soluble fractions from CFPS, wash and elution fractions from the column.

4.3.6. Negative-stain and cryoEM results

Although the complex was isolated successfully, no methane oxidation activity was observed either with copper sulfate added or with no extra copper added. To study the complex further and identify possible reasons for the lack of activity, samples were prepared for negative stain and cryoelectron microscopy (cryoEM). Polycistronic DNA was used in the presence of $CuSO_4$ and POPC nanodiscs and the complex was purified using a strep tag on the PmoC subunit (Figs A, B). The sample was investigated by negative stain electron microscopy which resulted in 2D class average images of the pMMO complex that resemble native-expressed pMMO in a nanodisc.[211] Along with the PmoC Strep tag pulling down the other two subunits and the MSP, this provides further evidence that the full pMMO complex is expressed into a nanodisc in the cell-free reaction and assembles into a trimeric complex similar to the native pMMO.

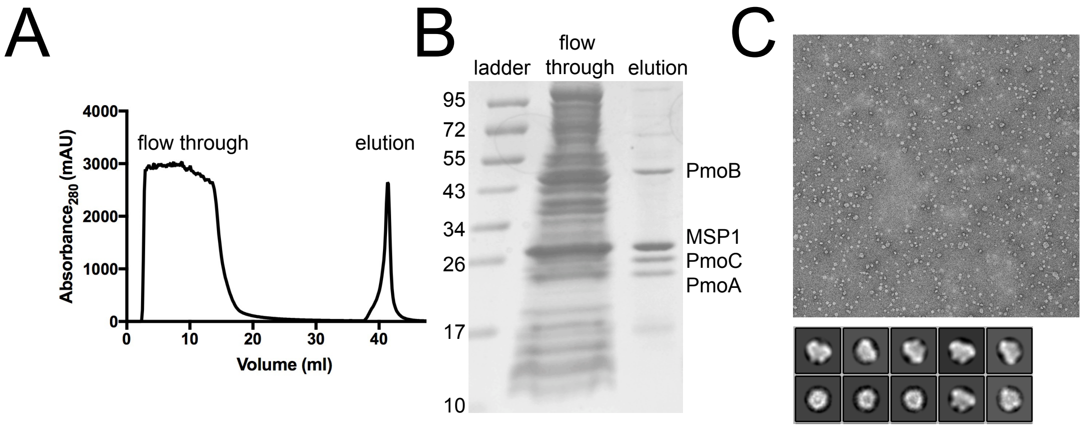

Figure 4.6. Negative stain of pMMO complex. (A) Strep-tagged purification profile using a StrepTactin HP column (Cytiva). (B) SDS-PAGE gel showing the three pMMO subunits and the membrane scaffold protein in the elution. (C) Representative negative stain micrograph and resulting 2D class averages.

4.4. Discussion

Cell-free protein synthesis combined with membrane mimetic technology remains a powerful tool for investigating otherwise intractable membrane enzymes. The ability to control and access the reaction mixture allows for fine control over the expression environment and over the construct being expressed. In this work we have shown how the system can be tuned to overcome the challenges of multi-subunit membrane complexes, copper metalloenzymes, and how the SUMO fusions can be used to generate the native enzyme. Future work should focus on the effect of mutants to the critically conserved regions of the enzyme, further structural work to determine the reason for the lack of activity, and metal spectroscopy to investigate whether the copper sites are loaded properly. There may be cofactors that are essential for activity that are still missing from the reaction mixture such as a partner protein or a small molecule metabolite that is present in methanotrophs and missing from *E. coli* extract.

4.5. Methods

4.5.1. Cloning and construct design

Codon-optimized constructs for *pmoA*, *pmoB*, and *pmoC* genes from *Methylococcus capsulatus* (Bath) were synthesized (Genscript) and cloned individually into the pJL1 vector using Gibosn assembly. They were also cloned into one pCDF-Duet vector backbone using both multiple cloning sites and creating a third site with its own promoter and ribosome binding site. The PmoC gene included a C-terminal Strep-tag II sequence (Trp-Ser-His-Pro-Gln-Phe-Glu-Lys). PmoB was cloned with an N-terminal SUMO fusion protein.[262] The SUMO tag also had an N-terminal CAT sequence (Met-Glu-Lys-Lys-Ile) which has been shown to increase yield in the cell-free system.[263,264]

4.5.2. Cell-free extract preparation

Cell growth was initiated by inoculating 5 ml LB cultures with BL21 Star (DE3) cells from a glycerol stock grown with no antibiotics overnight at 37 °C. This culture was used to inoculate a 100 ml LB culture, which was grown overnight at 37 °C. This culture was then used to inoculate 1 L of 2xYT media with an initial optical density at 600 nm (OD_{600}) of 0.07. This culture was grown to an OD_{600} of 4.0 after ~ 3 h at 37 °C and harvested by centrifugation at 8000 x g for 10 min at 4 °C, yielding approximately 10 g of cells. The cell pellet was washed in cold buffer containing 10 mM Tris-acetate, pH 8.2, 14 mM $Mg(acetate)_2$, and 60 mM potassium acetate by resuspending by vortexing followed by another round of centrifugation (repeated for a total of three washes). The cell pellet was weighed, flash frozen in liquid nitrogen, and stored at -80 °C.

Cell extract was prepared by thawing the cell pellet in cold acetate buffer. Buffer was added to the pellet at a ratio of 0.8 ml per 1 g cells in a 50 ml conical tube, followed by vortexing in 10 s increments, incubating the solution on ice in between vortexing to keep the cells as cold as possible. Once the cells were completely resuspended, the solution was lysed using a chilled Emulsiflex (ATA Scientific) by passing the solution through the system twice. The lysed cells were then centrifuged at 10,000 x g for 10 min at 4 °C to separate insoluble cell material from the soluble cell extract. The soluble portion was collected, aliquoted, and flash frozen with liquid nitrogen, storing at -80 °C.

4.5.3. Nanodisc preparation

Membrane scaffold protein was prepared using established methods.[176,197] BL21 (DE3) cells containing the MSP1 plasmid (Addgene) were grown in TB media at 37 °C to an OD_{600} of

2.1, induced with 1 mM IPTG, grown for 4 h a 37 °C, and harvested by centrifugation at 8000 x g for 10 min. Cell pellets were weighed and flash-frozen in liquid nitrogen. To isolate MSP1, the pellet was resuspended in buffer containing 20 mM Tris, pH 8.0, 250 mM NaCl, and 10 mM imidazole and lysed by sonication for 10 min with 1s/2 s on/off pulses on ice at 35% amplitude. The lysate was centrifuged at 20,000 x g for 30 min, and the soluble fraction was applied to a nickel-NTA gravity column. The beads were washed with 5 column volumes (cv) buffer containing 20 mM Tris, pH 8.0, 250 mM NaCl, 10 mM imidazole, and 50 mM sodium cholate followed by 10 cv buffer containing 20 mM Tri,s pH 8.0, 250 mM NaCl, 10 mM imidazole. MSP1 was eluted from the beads with 5 cv buffer containing 20 mM, Tris pH 8.0, 250 mM NaCl, and 250 mM imidazole. TEV protease was added at a ratio of 1:50 mol:mol and the elution fraction was dialyzed against buffer containing 20 mM Tris, pH 8.0, 250 mM NaCl, and 10 mM imidazole overnight at 4 °C. The elution was applied to nickel-NTA beads, and the flow through containing cleaved MSP1 was collected. The solution was concentrated and buffer exchanged into 25 mM PIPES, pH 7.3, 250 mM NaCl using an Amicon centrifugal concentrator with a 10 kDa molecular weight cutoff, aliquoted, and flash frozen in liquid nitrogen.

POPC or DMPC lipids dissolved in chloroform were prepared by drying the solution under nitrogen until a thin layer was formed in a glass vial which was then dried overnight in a vacuum desiccator wrapped in foil. The lipids were resuspended to a lipid concentration of 50 mM in buffer containing 25 mM PIPES, pH 7.3, 250 mM NaCl, and 100 mM sodium cholate by alternating vortexing, heating at 60 °C, and sonication in an ultrasonic bath until the lipids were fully dissolved. The lipid solution was aliquoted and stored at -20 °C.

Lipids and MSP1 were mixed together at a molar ratio of 1:130 MSP1:POPC and 1:150 MSP1:DMPC. The mixture was mixed end over end at 20 rpm at 4 °C for 15 min and then dialyzed against buffer containing 25 mM HEPES, pH 7.0, 250 mM NaCl for 2 h at 4 °C, exchanging the buffer and dialyzing overnight. The solution was then concentrated and applied to a Superose 6 increase GL 10/300 column, and fractions containing empty nanodiscs were collected, aliquoted, and flash frozen.

4.5.4. Cell-free reaction

Cell free reactions were prepared in either 30 µl reactions for radioactive quantitation tests in 1.5 ml microfuge tubes or 500 µl reactions for protein isolation in a 6-well cell plate. The reaction mixture was composed of 8 mM magnesium glutamate, 10 mM ammonium glutamate, 130 mM potassium glutamate, 1.2 mM ATP, 0.85 mM each of UTP, CTP, and GTP, 0.034 mg/ml folic acid, 0.171 mg/ml *E. coli* tRNA mixture, 2 mM each of the 20 standard amino acids, 10 µM of L-[^{14}C(U)]-leucine (only for radioactive quantitation experiments), 30 mM phosphoenoylpyruvate (PEP), 0.33 mM nicotinamide adenine dinucleotide (NAD), 0.27 coenzyme-A (CoA), 4 mM sodium oxalate, 1 mM putrescine, 1.5 mM spermidine, 100 µg/ml T7 polymerase, 57 mM HEPES, pH 7.2, 26.7 µg/ml plasmid, and 27% (v/v) extract. 50 µg/ml SUMO protease, copper, membrane mimetic. All reactions were performed at room temperature for 20 h.

4.5.5. Radioactive Quantification

Radioactive L-[^{14}C(U)]-leucine was added to 15 µl reactions for quantification of protein expression. At the end of the reaction, 2 µl was removed for gel electrophoresis of total protein expression and 4 µl was removed for quantification. The reaction was centrifuged at 12,000 x g for 10 min to pellet insoluble protein, and 2 µl of the soluble fraction was removed for gel electrophoresis and 4 μl was removed for quantification of soluble protein expression. 100 μl 0.1 M NaOH was added to each quantification fraction and incubated at 37 °C for 20 min. Two tabs of Whatmann 3MM chromatography paper (GE Healthcare) were prepared for each reaction, marked "washed" and "unwashed", and suspended above an aluminum foil-wrapped Styrofoam block using straight pins. Following incubation, samples were mixed by pipetting and 50 μl were applied to each of the two filter papers and dried for 1 h under a heat lamp. Tabs designated for washing were placed in a beaker with 5% trichloroacetic acid (TCA) at 4 °C to precipitate the protein. After 15 min, the buffer was removed and replaced with fresh 5% TCA buffer, for a total of 3 exchanges. Afterwards, the tabs were immersed in 100% ethanol for 10 min at room temperature. The tabs were then mounted on Styrofoam and dried for 1 h under a heat lamp. Finally, each tab was placed in a microfuge tube and submerged in 1 mL scintillation fluid. Remaining radioactivity was measured using a MicroBeta 2 scintillaton counter (Perkin Elmer). Protein yield was determined according to the following equation:

$$\begin{aligned}&[((Washed\ cpm - Background\ cpm)/\ Unwashed\ cpm) * [Leucine\ in\ rxn]\ uM \\ &\qquad * (MW\ protein\ ug/Mol)]\ /\ [(\#\ Leucine\ residues) * (1000\ mL/L) = ug/mL\end{aligned}$$

4.5.6. Autoradiogram

For autoradiogram analysis, CFPS reactions included 10 μM L-[^{14}C(U)]-leucine. As described above, 2 μl each of the total and soluble fractions were collected and run on a 12% Bis-Tris NuPAGE gel (Thermo Fisher sciences). After electrophoresis, the gel was soaked in gel drying solution (Bio-Rad) for 30 min and fixed with cellophane film. The film was dried in a

GelAir Dryer (Bio-Rad) and exposed for 1 day on a Storage Phosphor screen (GE Healthcare). A Typhoon FLA 7000 Imager (GE Healthcare) was then used to image the autoradiogram.

4.5.7. Protein purification

The reaction mixture was centrifuged for 10 min at 14,000 x g and then applied to a StrepTactin HP column (Cytiva) followed by washing with 10 cv of buffer containing 25 mM PIPES, pH 7.3, and 250 mM NaCl. The complex was eluted using 5 cv of the same buffer containing 2.5 mM desthiobiotin. Fractions containing the eluted complex were combined and concentrated using an Amicon filter (100 kDa MWCO, MilliporeSigma). The concentrated fractions were then applied to a Superose 6 increase 10/300 GL column (Cytiva) and peak fractions were concentrated.

4.5.8. Negative stain and 2D class averaging

400-mesh carbon-coated copper grids (Fisher) were prepared for negative stain by applying 3 μl sample at 0.01 mg/ml and incubated at room temperature for 1 min. The sample was blotted using Whatman filter paper and washed in 50 μl drops of water for 15 s twice followed by 15 s in 50 ul drops of 2% uranyl formate twice. The grid was blotted, dried, and stored in a gridbox.

The sample was imaged using a JEM-1400 microscope (Jeol). 12 images were collected with a random defocus ranging from 3-6 μm. The micrographs were analyzed using Relion v3.1.[267] Particles were picked using LoG picker with a range of 110 – 150 Å, resulting in 20,000 particles from which 2D class averages were generated.

CHAPTER 5: Further work and prospectus

5.1. Further *Methylococcus capsulatus* (Bath) cryoEM work.

5.1.1. No copper added structure

Following the publication of the cryoEM manuscript, a structure of *M. capsulatus* (Bath) pMMO in a native nanodisc with no additional copper added was solved to a resolution of 2.2 Å. This sample has similar methanol oxidation activity to DDM-solubilized pMMO (Fig. 2.2) and nanodisc samples had higher activity, regardless of the lipid used. The main pMMO nanodisc sample reconstituted with 3 equivalents of copper sulfate (MC01) was ~ 5x more active (Fig. 2.2). At this high resolution, neither copper nor water molecules are detected in either Cu_C or Cu_D (Fig 5.1). Therefore, while the restoration of the 4-helix bundle in PmoC alone restores some methane oxidation activity, proper metal loading of Cu_D is responsible for the improved activity in the sample with copper added (MC01). It should also be noted that Cu_B and the bis-His site are both loaded in the no Cu nanodisc sample.

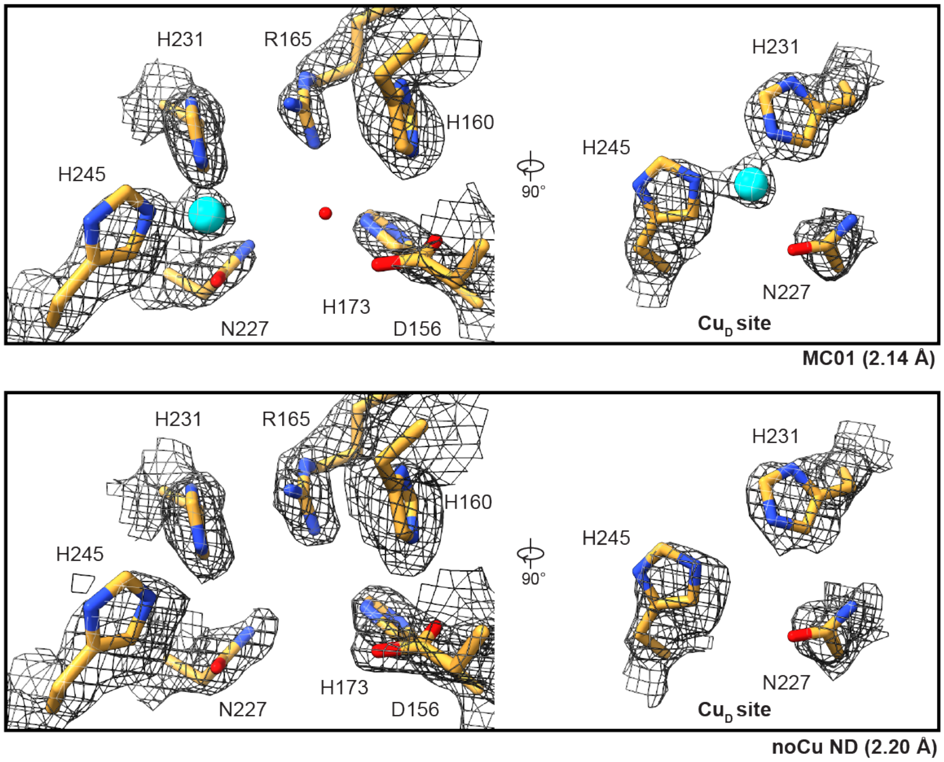

Figure 5.1. $\mathrm{Cu_C}$ and $\mathrm{Cu_D}$ sites in pMMO nanodisc reconstituted with copper (MC01) and without copper (noCu ND). The maps are shown at the same threshold level. The overall arrangement of both sites are shown on the left and the $\mathrm{Cu_D}$ sites are shown alone on the right.

5.2. Ammonia monooxygenase structure and sample preparations

5.2.1. Introduction to ammonia monooxygenase

Ammonia monooxygenase (AMO) and particulate methane monooxygenase (pMMO) belong to the same superfamily of membrane-bound copper-dependent enzymes that oxidize a range of small compounds.[69,268] Although their host bacteria are dissimilar in physiology and lifestyle, both enzymes fulfill a similar role. AMO converts ammonia to hydroxylamine as the first step of nitrogen fixation by nitrifying bacteria whereas pMMO converts methane to methanol in methanotrophs.[67,269] Due to the difficulty of culturing these bacteria and the absence of a viable heterologous expression system, pMMO is the only enzyme of this superfamily that has been structurally characterized. Solving the AMO structure would pinpoint the residues necessary for both ammonia and methane oxidation and determine the residues are responsible for differentiating between the two substrates. This will shed light on the mechanism of ammonia oxidation and on the mechanism of the overall superfamily of enzymes.

5.2.2. AMO isolation and mass spectrometry identification

Nitrosomonas europaea cells were solubilized in buffer containing 25 mM PIPES, pH 7.3, 250 nM NaCl, protease inhibitor cocktail (Roche) and DNase. Cells were lysed by sonication on ice using 1 s/1 s on/off pulses for a total of 10 minutes (Qsonica 700). Cell debris was removed by centrifugation at 20,000 x g for 45 min and membranes were isolated by centrifuging the supernatant at 150,000 x g for 60 min. The membrane fraction was resuspended in 40 ml of buffer containing 25 mM PIPES, pH 7.3, and 250 mM NaCl using a Dounce homogenizer and centrifuged at 150,000 x g for 30 min. This process was repeated twice. The final membrane fraction was resuspended in 7 ml of the same buffer and flash frozen in 1 ml aliquots. Protein concentration was measured by DC-Lowry assay (Bio-Rad).

Membrane aliquots were thawed and resuspended with n-undecyl-beta-maltoside (UDM) at a 1.2:1 mg:mg ratio end over end for 1 h at 4 °C. Solubilized enzyme was separated out by centrifugation at 150,000 x g for 1 h, collecting the soluble fraction. The soluble fraction was concentrated using an Amicon concentrator with a 100 kDa molecular weight cutoff. SDS-PAGE gels were run and in-gel digestion combined with mass spectrometry was used to confirm the presence of AMO subunits in this solubilized fraction (Fig 5.2).

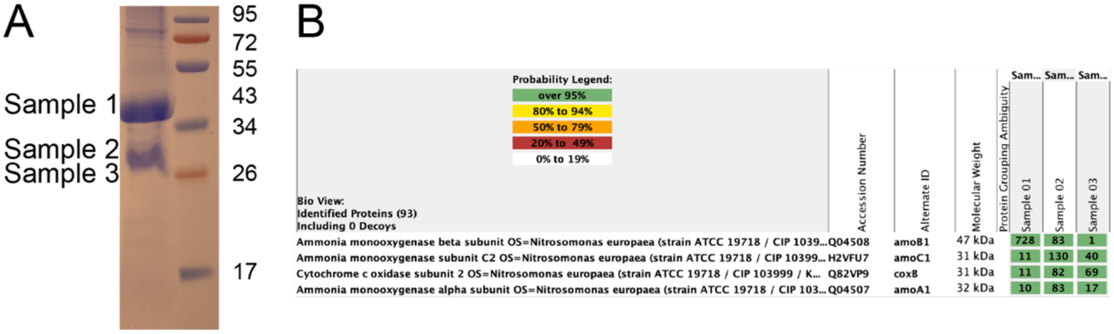

Probability Legend:
- 🟩 over 95%
- 🟨 80% to 94%
- 🟧 50% to 79%
- 🟥 20% to 49%
- ⬜ 0% to 19%

Bio View:
Identified Proteins (93)
Including 0 Decoys

	Accession Number	Alternate ID	Molecular Weight	Protein Grouping Ambiguity	Sam... Sample 01	Sam... Sample 02	Sam... Sample 03
Ammonia monooxygenase beta subunit OS=Nitrosomonas europaea (strain ATCC 19718 / CIP 1039...	Q04508	amoB1	47 kDa		728	83	1
Ammonia monooxygenase subunit C2 OS=Nitrosomonas europaea (strain ATCC 19718 / CIP 10399...	H2VFU7	amoC1	31 kDa		11	130	40
Cytochrome c oxidase subunit 2 OS=Nitrosomonas europaea (strain ATCC 19718 / CIP 103999 / K...	Q82VP9	coxB	31 kDa		11	82	69
Ammonia monooxygenase alpha subunit OS=Nitrosomonas europaea (strain ATCC 19718 / CIP 103...	Q04507	amoA1	32 kDa		10	83	17

Figure 5.2. AMO subunits identified by mass spectrometry in a UDM-solubilized sample. (A) SDS-PAGE gel with UDM-solubilized AMO and Prestained Ladder (Thermo Fisher). (B) Identified proteins from samples cut out of the gel and digested by trypsin. The counts indicate the presence of the three AMO subunits in the sample.

5.2.3. Detergent cryoEM sample

Samples were prepared for cryoEM analysis using a Vitrobot (Fisher) by applying 3 µl of sample at 1 mg/ml to a plasma-cleaned 400-mesh 1.2/1.3 c-flat copper grid (Electron Microscopy Sciences), incubating at 100% humidity and 4 °C for 30 s, blotting with 0 blot force for 4 s, and plunge-freezing in liquid ethane. The samples were screened on a JEM-1400 transmission electron microscope (Jeol). The sample appeared monodisperse and present in the open hole (Fig 5.3A). The sample was sent to the Pacific Northwest CryoEM Center (PNCC) for data collection.

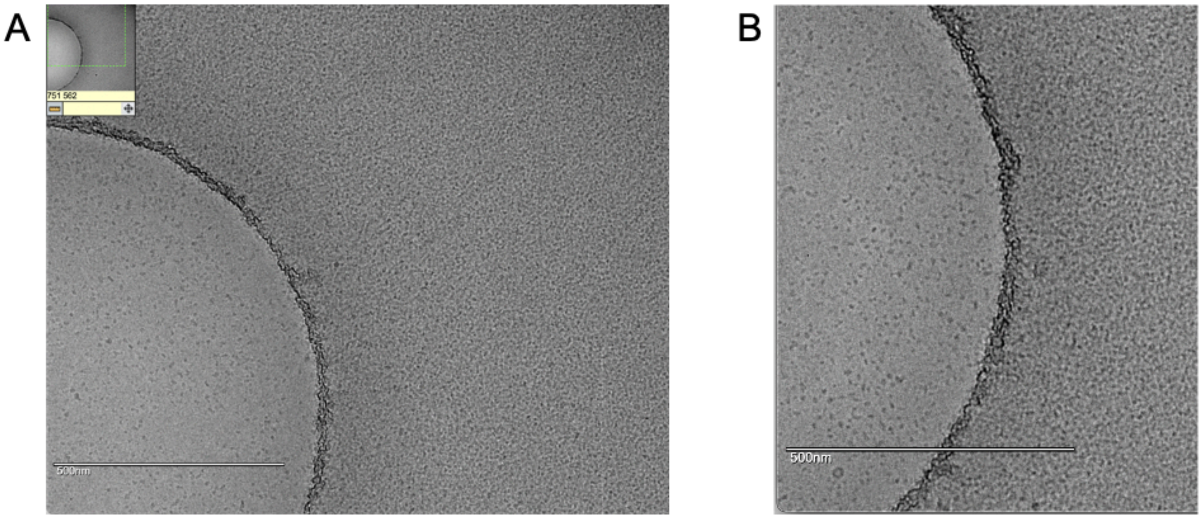

Figure 5.3. CryoEM screening images of AMO samples. AMO solubilized by UDM (A) and reconstituted into a nanodisc (B). Curvature indicates the open hole where the vitreous ice layer forms.

5.2.4. Nanodisc reconstitution and cryoEM sample

Nanodiscs of AMO were formed using MSP1 and a similar approach to the pMMO reconstitution methods. Surprisingly, Bio-Bead (Bio-Rad) AMO nanodisc reconstitution resulted in a large void peak whereas formation by removal of detergent via overnight dialysis resulted in a robust nanodisc peak. For the pMMO project, nanodisc reconstitution via removal of detergent by dialysis is a gentler method, but Bio-Beads were favored because this method resulted in active pMMO whereas dialysis diluted the copper concentration leaving the labile sites in PmoC. For AMO, Bio-Beads resulted in a large void peak upon size-exclusion chromatography (Fig 5.4A). Overnight removal of detergent by dialysis resulted in a smaller void peak relative to the nanodisc peak (Fig 5.4B). The nanodisc peak was then used to make another cryoEM sample by the same methods as above. The sample was screened in a similar fashion and showed good particle dispersity (Fig. 5.3B). Data collection and structural characterization on this sample is also ongoing at PNCC.

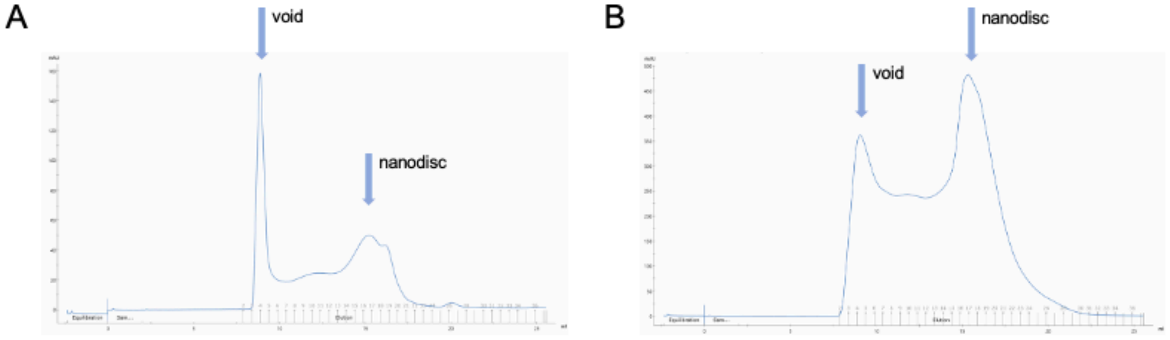

Figure 5.4. AMO nanodisc size-exclusion chromatograms. UV absorbance at 280 nm (A_{280}) from a Superose 6 column for AMO nanodiscs formed with Bio-Beads (A) and by overnight dialysis (B).

5.3. Initial styrene-maleic acid co-polymer experiments

Styrene-maleic acid lipid particles (SMALPs) are nanodiscs formed using a styrene-maleic acid (SMA) co-polymer instead of a membrane scaffold protein (MSP). The SMA co-polymers are small enough to slide into the membrane bilayer and wrap around the lipid tails, solubilizing the embedded enzyme directly from the membrane bilayer.[270-272] This avoids the detergent extraction step that is necessary when using MSPs and has been used in cryoEM studies to solve of membrane proteins embedded in native lipids.[273]

There are many formulations of SMA co-polymers available that differ in their styrene:maleic acid ratios, producing discs of varysing sizes. Three formulations, XIRAN 25010, XIRAN 30010, and XIRAN 40005 (Polyscope) were tested for solubilizing pMMO from *M. capsulatus* (Bath)l. Isolated membranes containing pMMO were mixed with SMA co-polymers at a final concentration of 5 mg/ml pMMO and 2.5% w/v SMA. After mixing for 2 h at 4 C, the solution was centrifuged at 150,000 x g for 30 min and the soluble fraction was purified by superose 6 size-exclusion chromatography.

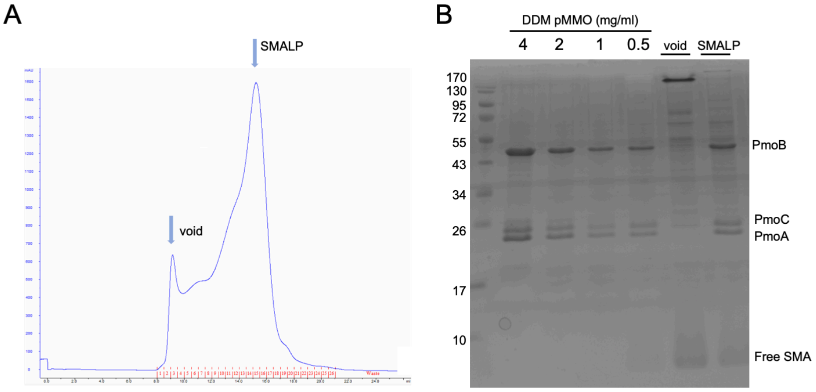

Figure 5.5. SMALP extraction of *M. capsulatus* (Bath) pMMO. (A) Size exclusion chromatogram showing the A_{280} trace for pMMO-SMALP. (B) Corresponding gel with DDM-solubilized pMMO included as a standard for protein quantification purposes.

The three SMA co-polymer formulations were tested and XIRAN 30010 resulted in a SMALP nanodisc peak (Fig 5.5A) while the other two resulted in a large void peak. The elution profile of the SMALPs indicated that they are similar size as MSP nanodiscs. The SMA co-polymer can be visualized by coommassie stain and can be seen in the SMALP lane of the gel (Fig 5.5B). While this is the first non-detergent extraction of pMMO, the resulting sample was not active. This may be due to chelation of copper or other disruption to the pMMO structure by the SMA. There are many formulations and SMA co-polymer products available and other SMA formulations may result in an active pMMO sample.

5.4. Prospectus

In this thesis dissertation, nanodiscs and cryoEM techniques were used to investigate pMMO structure and function in an active form. This work revealed the structure of the strictly conserved region of the enzyme and a new metal binding site, paving the way for future investigations into the native occupancy and organization of the pMMO active stie. A cell-free protein synthesis system was also developed to express mutants of pMMO, investigating the role of individual amino acids in methane oxidation. The groundwork was laid for such a system and future work is needed to obtain active enzyme before generating and characterizing mutants of pMMO. This work has established new areas of focus for the next phase of pMMO investigation.

5.4.1. Native occupancy of the Cu_C and Cu_D sites

The cryoEM structures of pMMO consistently showed that the active form of pMMO has metal density at the newly-discovered Cu_D site. However, the results were not as clear for the crystallographic Cu_C site. The question remains whether one or both sites are occupied in vivo and a secondary question about whether past spectroscopic work was detecting the $\mathrm{Cu_C}$ or $\mathrm{Cu_D}$ site. A DDM-solubilized cryoEM structure may resolve this question since this structure will be more similar to the samples that have been previously investigated by spectroscopy rather than the crystal structure which is buffer exchanged into cymal-5 detergent. Furthermore, the structure of pMMO from the *Verrucomicrobia* lacking $\mathrm{Cu_B}$ residues will be useful in resolving this question.

Beyond this, the asparagine binding to copper and the arginine are new additions to the PmoC site. Asparagine is an unusual amino acid to coordinate copper and warrants further investigation. Arginine is a charged amino acid commonly found buried within hydrophobic regions and may be important for orienting oxygen or methanol after methane oxidation. Also there is a density assigned as a water that sits in the cavity below the $\mathrm{Cu_D}$ site. The identity of this ion may shed light on the role of the $\mathrm{Cu_C}$ and $\mathrm{Cu_D}$ sites.

5.4.2. Quinol/reductant binding site and electron transfer

The overall roles of $\mathrm{Cu_B}$, $\mathrm{Cu_C}$, and $\mathrm{Cu_D}$ are still undetermined. It is possible that $\mathrm{Cu_B}$ shuttles electrons to $\mathrm{Cu_C}$/$\mathrm{Cu_D}$ through hole hopping. A possible quinol binding site was also identified on the exterior of pMMO with some conserved residues in proximity. Identifying the site of reductant binding will be essential for elucidating the full system of methane oxidation and mapping electron transfer through the enzyme. This may be accomplished in the future by incubating pMMO with a quinol with a larger headgroup such as menaquinol or else a quinol analog and determining the structure. While there are many aromatic residues through which many electron paths could me mapped, it is difficult to disentangle aromatics that are present for their hydrophobic properties or for their electron transfer possibilities. Identifying the site of quinol binding may provide the starting and ending points for further investigation.

5.4.3. In vivo structure and possible binding partners

There is increasing biochemical evidence that pMMO may interact with binding partners to shuttle substrates, load copper, and recycle reducing equivalents to its active site. Methanol dehydrogenase (MDH) is the next enzyme in the metabolic pathway of methane, converting methanol to formaldehyde. One role of the PmoB periplasmic domain may be to act as a docking site for MDH in order to efficiently shuttle methanol to it. Future in vivo cryoET work or crosslinking single particle cryoEM work may reveal how such a docking site is organized. A supernumerary helix that copurifies with pMMOs from Type II methanotrophs remains to be identified and may play an important role in the stabilization of pMMO in the membrane in these methanotrophs. Finally, the role of the copper-binding enzyme PmoD, found in the extended operon of pMMOs from Type II methanotrophs remains to be determined and whether it interacts with or helps load copper into pMMO.

5.4.4. Cell-free advances in membrane complexes

CFPS remains an intriguing platform for obtaining pMMO mutants. The work here showed that it is possible to obtain pMMO subunits bound together in a nanodisc. The next challenge would be to obtain an active form of pMMO from which mutants can be generated and chatacterized. This work shows that it is possible to express a multi-subunit membrane complex using CFPS in combination with nanodiscs.

APPENDIX A: Supplemental data for chapter 2

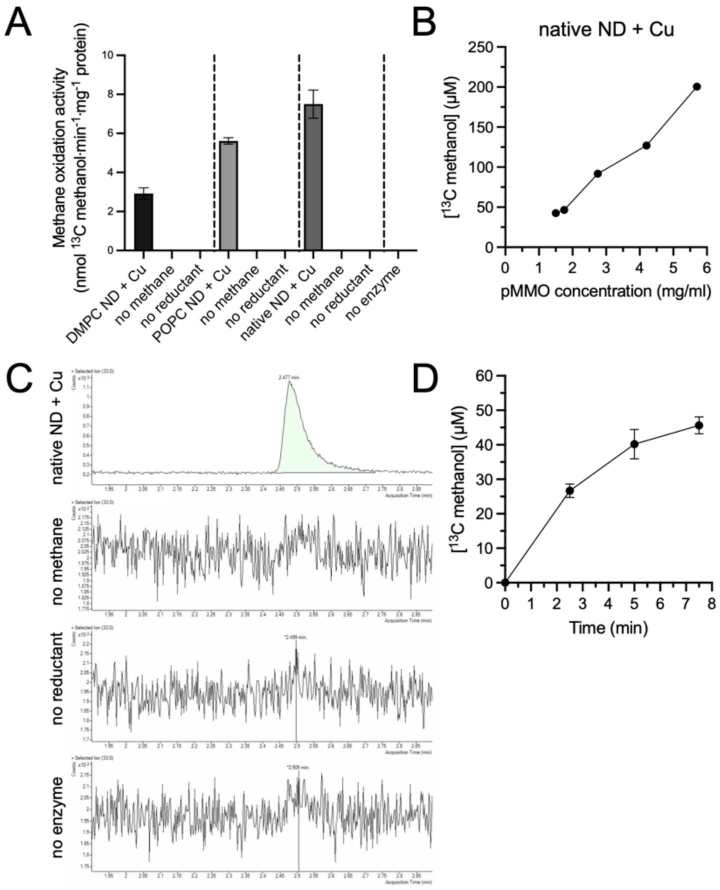

Figure S2.1. Methane oxidation activity assay data. (**A**) Methane oxidation activity of pMMO reconstituted into nanodiscs (ND) in the presence of 3 equivalents of $CuSO_4$ (+ Cu) with varying lipids and the corresponding control reactions. Error bars represent standard deviation of n ≥ 3 biological replicates, each measured in triplicate. (**B**) ^{13}C-methanol produced in the activity assay at varying concentrations of pMMO. Each datapoint represents 3 measurements (error bar too small to show). (**C**) GC-MS traces detecting the +33 ion corresponding to ^{13}C-methanol for the native ND + Cu sample. The area under peaks was integrated to determine ion count and the $^{[13]}$C-methanol concentration. (**D**) Time-dependent production of ^{13}C-methanol for 1 mg/ml pMMO reconstituted into native ND with 3 equivalents of $CuSO_4$ added during reconstitution. Error bars represent standard deviation of n ≥ 3 biological replicates, each measured in triplicate.

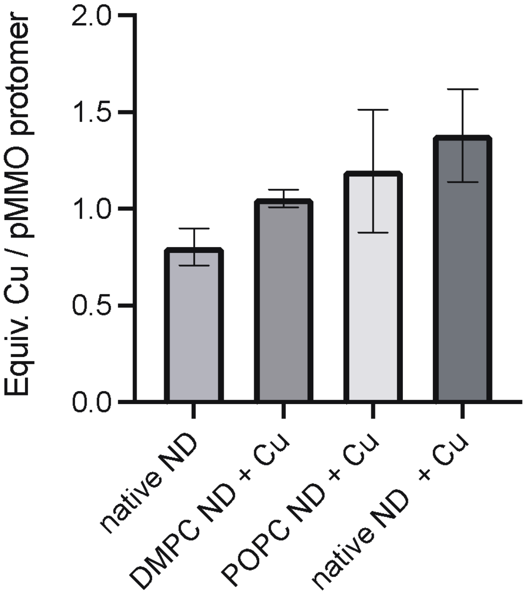

Figure S2.2. Copper content of *M. capsulatus* (Bath) nanodiscs with synthetic and native lipids. Three equivalents of $CuSO_4$ were added to the "+ Cu" samples. Error bars represent standard deviation of n ≥ 3 biological replicates, each measured in triplicate.

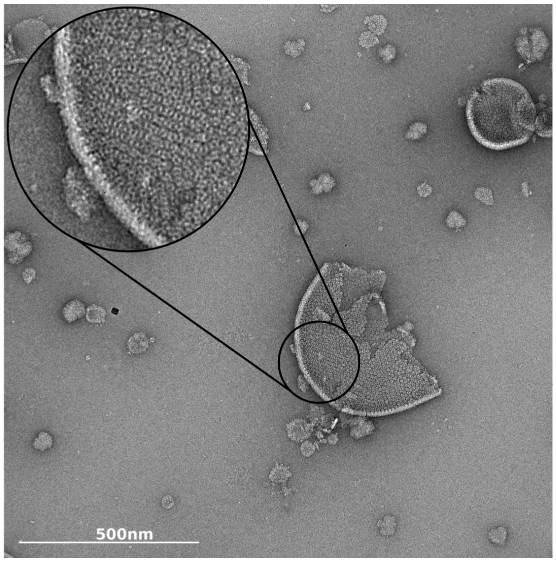

Figure S2.3. Negative stain EM micrograph of *M. capsulatus* (Bath) isolated membranes. Tightly packed pMMO trimers are clearly visible in the membrane.

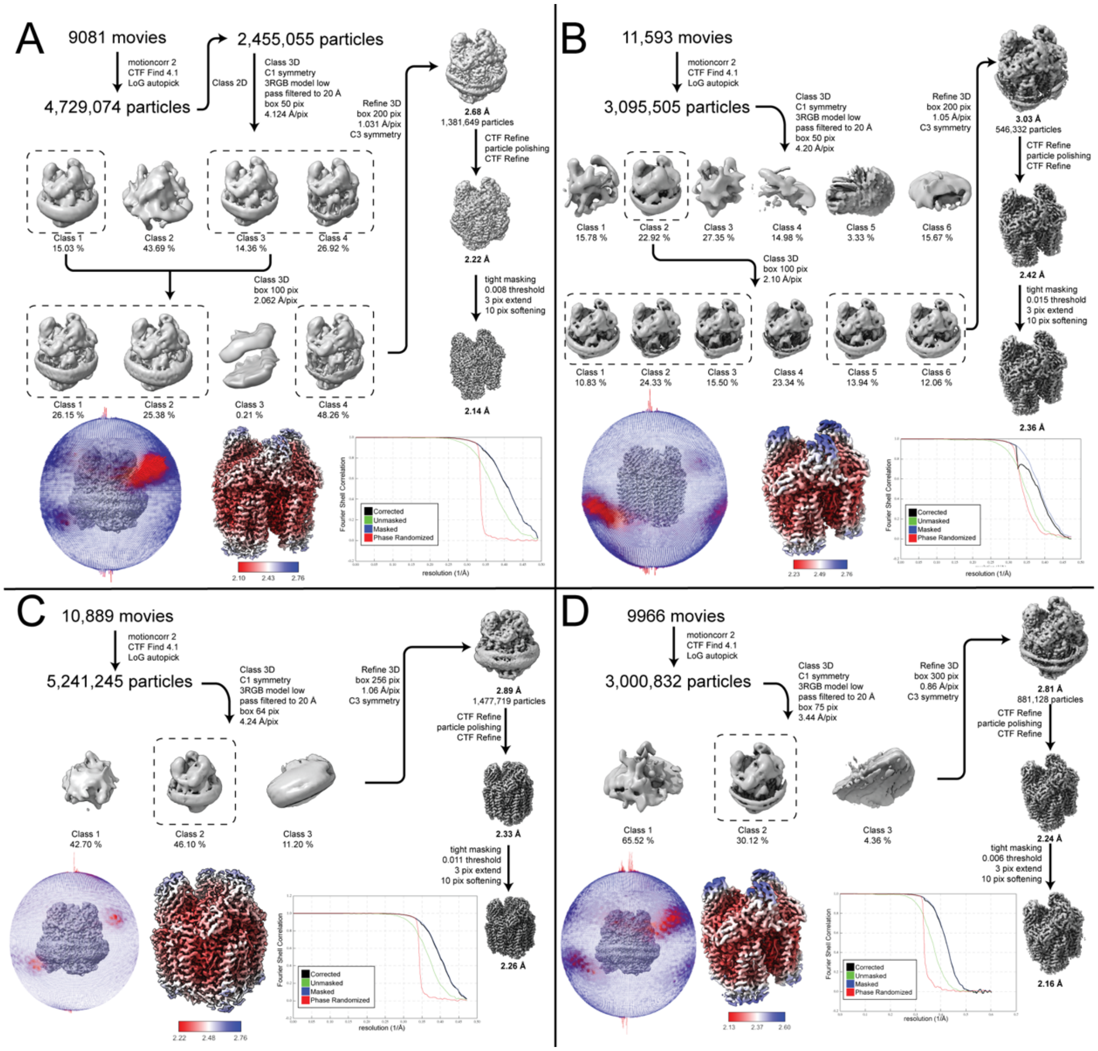

Figure S2.4. Processing pipeline for *M. capsulatus* (Bath) cryoEM maps using Relion v3.1.0, including the local resolution determined by Relion's implementation and FSC curve for each final masked reconstruction. (**A**) MC01 dataset. (**B**) MC04 dataset. (**C**) MC02 dataset. (**D**) MC03 dataset.

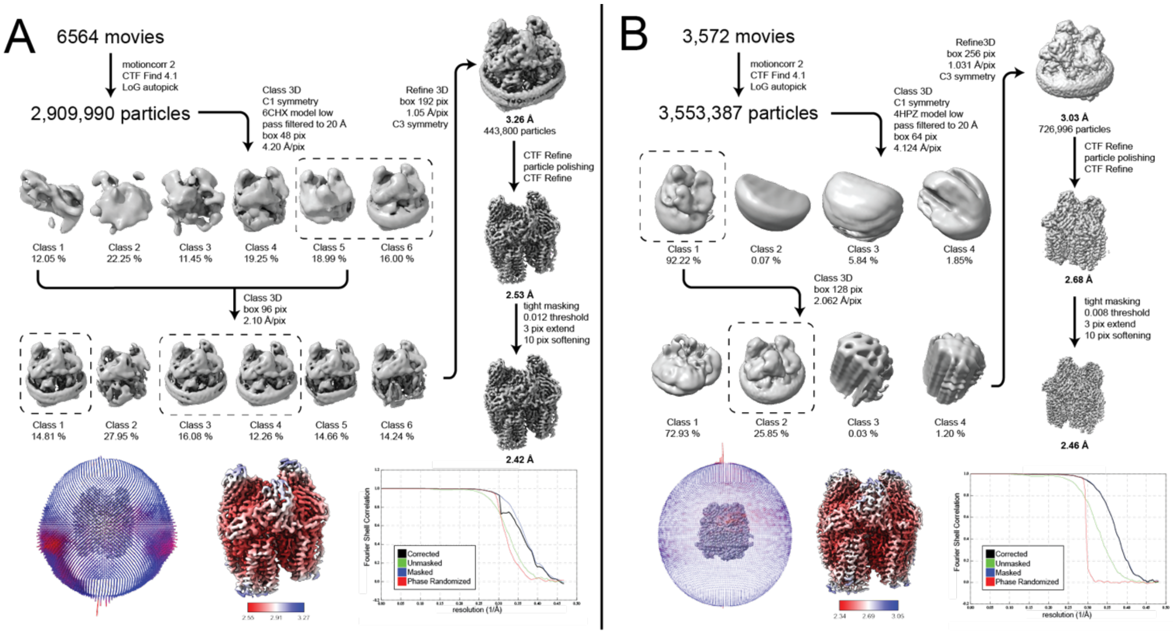

Figure S2.5. Processing pipeline for *Mt. alcaliphilum* comb. nov. 20Z and *Mc.* sp. str. Rockwell using Relion v3.1.0, including the local resolution determined by Relion's implementation and FSC curve for each final masked reconstruction. (**A**) 20Z01 dataset. (**B**) RW01 dataset.

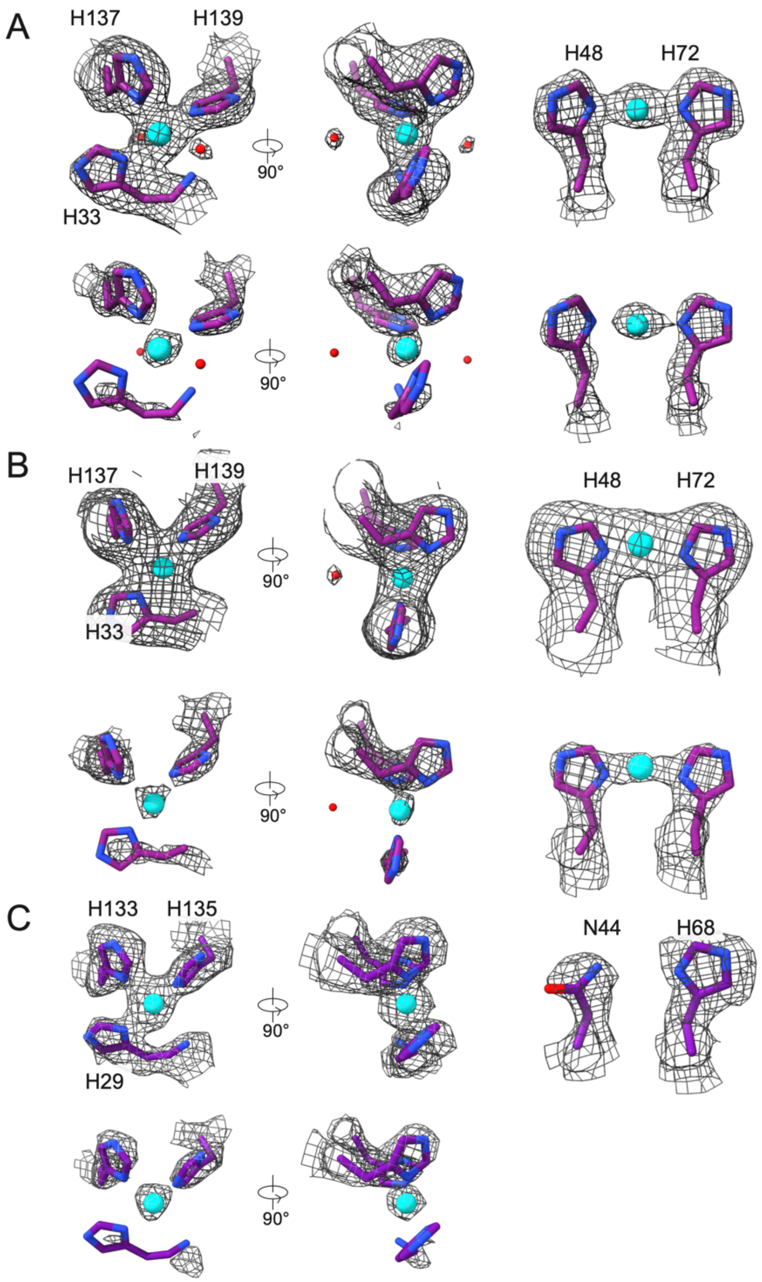

Figure S2.6. Cu_B site and bis-His site in cryoEM maps. (**A**) pMMO from *M. capsulatus* (Bath) resolved to 2.14 Å (MC01) is shown at two thresholds (0.026 and 0.056). At the higher threshold, it is clear that each site is mononuclear. (**B**) pMMO from *Mt. alcaliphilum* comb. nov. 20Z resolved to 2.44 Å (20Z01). (**C**) pMMO from *Mc.* sp. str. Rockwell resolved to 2.42 Å (RW01). The bis-His site is not conserved in this species and residue Asn44 corresponds to the missing histidine.

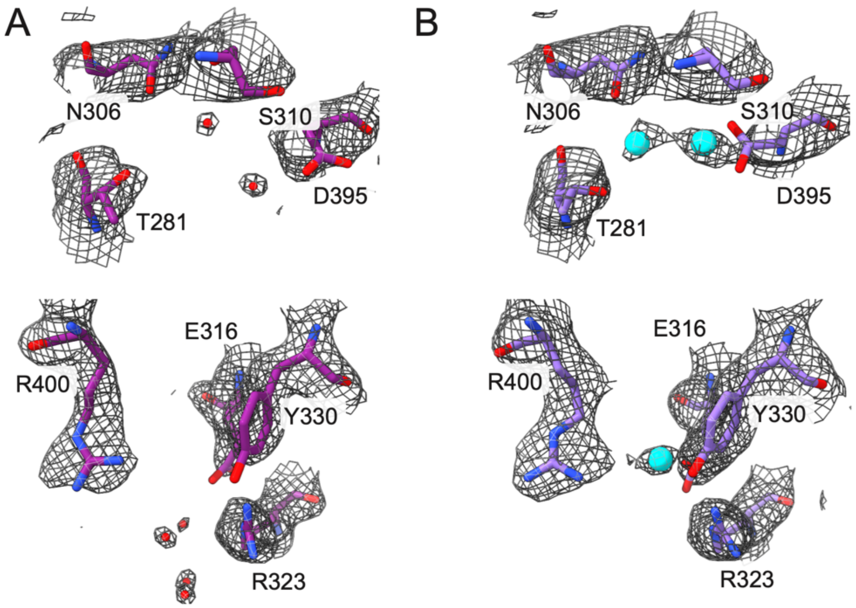

Figure S2.7. CryoEM density at the proposed "copper sponge" site in the PmoB subunit of *M. capsulatus* (Bath) pMMO. (**A**) The 2.14 Å resolution map (MC01, this study) and model of active pMMO in native lipid nanodiscs shown at 0.018 threshold. (**B**) The 2.6 Å resolution model (PDB 7EV9) and map (EMDB 31325) of pMMO in detergent shown at 0.6 threshold. At this threshold level, where water molecules are visible in (**A**), there is no evidence for copper ions at this site.

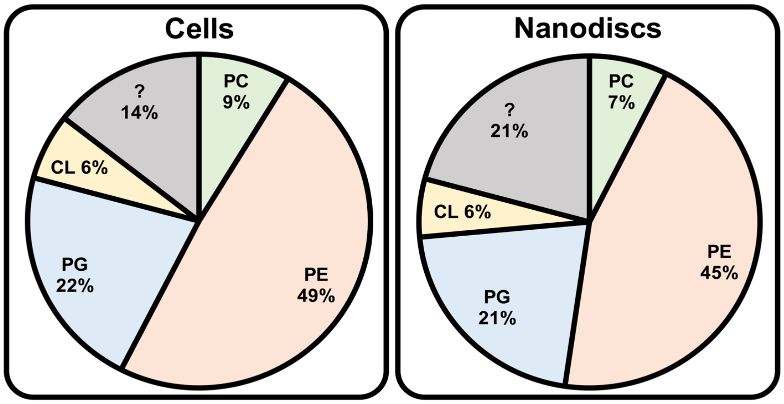

Figure S2.8. Distribution of different classes of lipids in *M. capsulatus* (Bath) whole cells and *M. capsulatus* (Bath) pMMO reconstituted into native lipid nanodiscs. Phosphatidylethanolamine (PE), phosphatidylcholine (PC), phosphatidylglycerol (PG), and cardiolipin (CL) were identified. A percentage of the lipids in each sample could not be identified (gray).

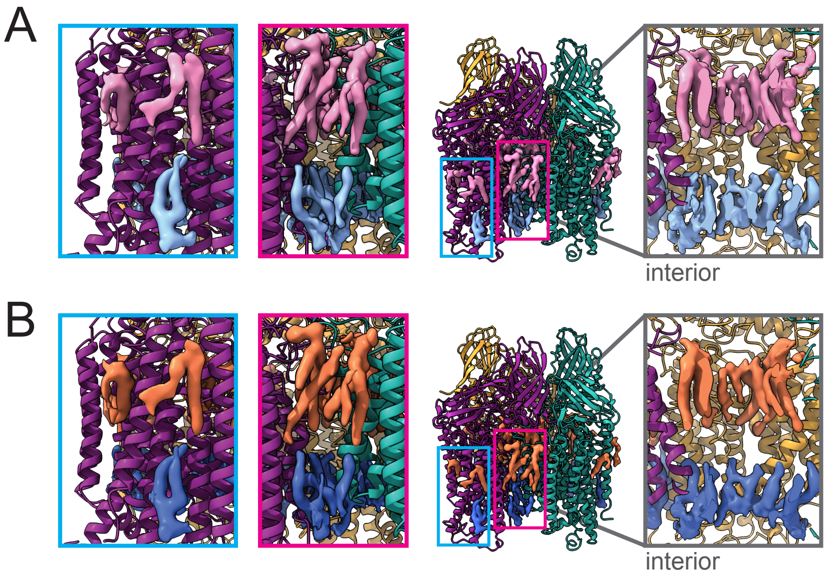

Figure S2.9. Comparison of lipid densities between structures of pMMO in native lipid (MC01) and POPC (MC02) nanodiscs. (**A**) Model and densities from map MC01. Native periplasmic lipids are in pink and cytoplasmic lipids are in light blue. (**B**) Model and densities from map MC02. POPC periplasmic lipids are in orange and cytoplasmic lipids are in dark blue. The left panels show lipids on the exterior of the enzyme while the right panels show lipids on the interior of the pore. Yellow arrows (left panels) denote lipid densities whose headgroups are significantly different from other well-defined lipids.

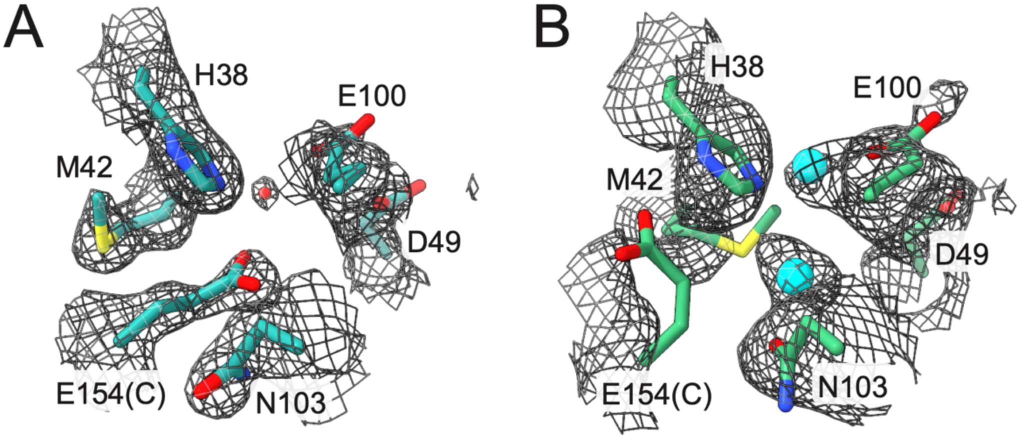

Figure S2.10. CryoEM density at the proposed "trinuclear" copper site in the PmoA subunit of *M. capsulatus* (Bath) pMMO. (**A**) The 2.14 Å resolution map (MC01, this study) and model of the active pMMO in native lipid nanodiscs shown at 0.034 threshold. (**B**) The 2.6 Å resolution model (PDB 7EV9) and map (EMDB 31325) of pMMO in detergent shown at 0.42 threshold. At this threshold level where waters are visible, there is no evidence for a trinuclear copper center. Instead, residue E154 from PmoC fits into the density assigned as copper in 7EV9. A water is modeled in MC01 in the density assigned as a second copper ion in 7EV9.

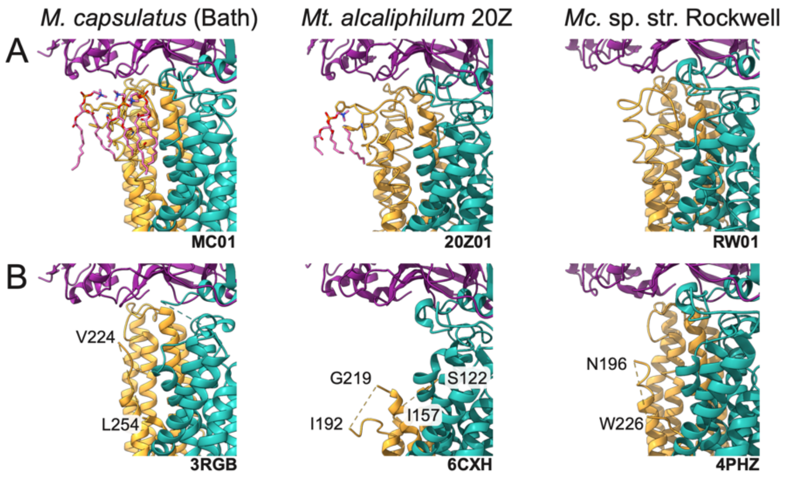

Figure S2.11. Conserved region of PmoC newly observed in the cryoEM maps. (**A**) Models based on the cryoEM maps. (**B**) Crystal structures of pMMO from each species. PmoB is colored in purple, PmoA in teal, and PmoC in gold. The terminal residues adjacent to the missing regions are labeled.

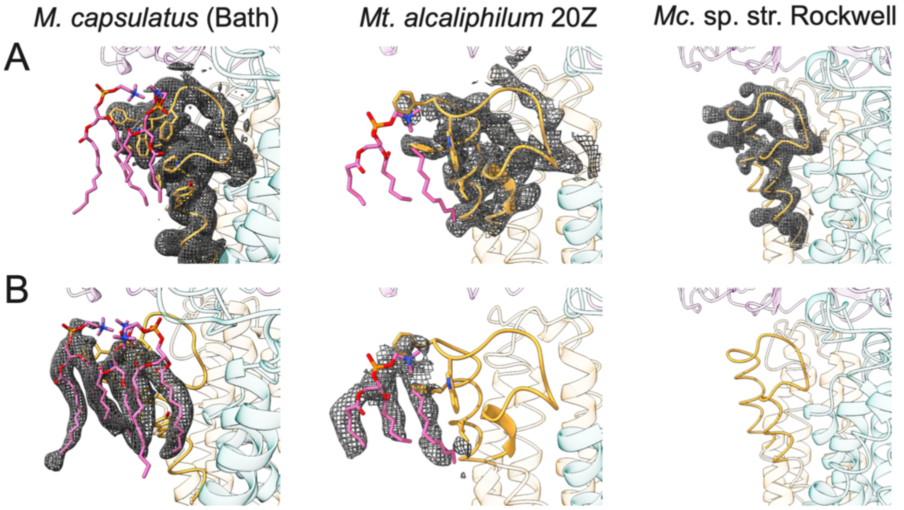

Figure S2.12. Densities for conserved region of PmoC and neighboring lipids. (**A**) CryoEM map corresponding to the region missing in the crystal structures. (**B**) Models of the new region with density for stabilizing inner lipids. Residues that interact with lipids (< 4 Å distance) include *M. capsulatus* (Bath) PmoC residues Leu226, Trp229, Phe233, Trp234, Phe235, Pro243, and Tyr246 and *Mt. alcaliphilum* comb. nov. 20Z PmoC residues Leu198, Trp201, Phe205, and Phe206. While there is density present at the corresponding positions in the map of *Mc.* sp. str. Rockwell pMMO (RW01), lipids could not be fit definitively into this density.

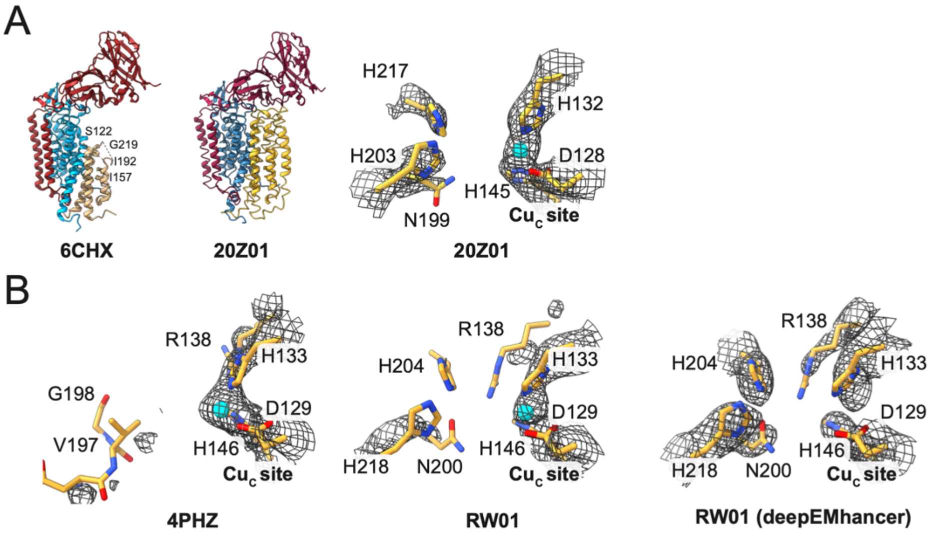

Figure S2.13. Copper binding sites in *Mt. alcaliphilum* comb. nov. 20Z and *Mc.* sp. str. Rockwell PmoC subunits. (**A**) Comparison of the *Mt. alcaliphilum* comb. nov. 20Z crystal structure and cryoEM structure. The $\mathrm{Cu_C}$ site and surrounding region is completely missing in the crystal structure, whereas residues 20-89, 123-156, and 193-218 are visible in the cryoEM density. The $\mathrm{Cu_C}$ site is occupied in the nanodisc structure, although the residue corresponding to Arg165 in M. capsulatus (Bath) PmoC (Arg137) is missing. (**B**) Comparison of the *Mc.* sp. str. Rockwell crystal structure and cryoEM structure. DeepEMhancer[193] was used to fit the $\mathrm{Cu_D}$ residues Asn200, His204, His218, and Arg138.

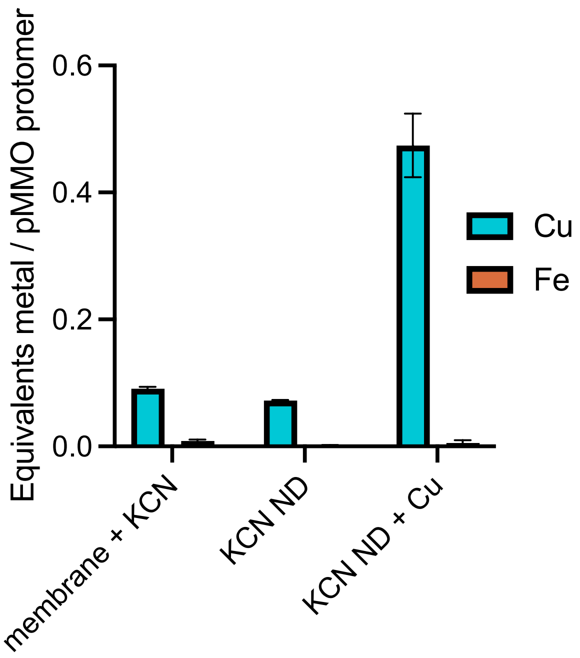

Figure S2.14. ICP-MS analysis of pMMO treated with potassium cyanide (KCN). Membrane + KCN, isolated *M. capsulatus* (Bath) membranes treated with KCN; KCN ND, nanodiscs formed with pMMO from the KCN-treated membranes and native lipids; KCN ND + Cu, copper added back to KCN-treated membranes followed by pMMO isolation from those membranes and reconstitution into nanodiscs with native lipids. Error bars represent standard deviation of n = 3 biological replicates, each measured in triplicate.

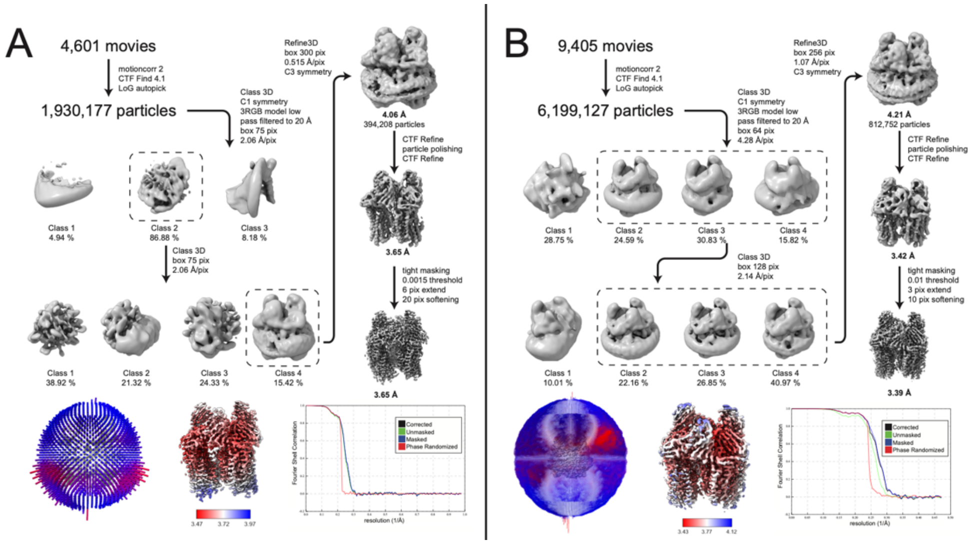

Figure S2.15. Processing pipeline for *M. capsulatus* (Bath) samples treated with potassium cyanide, including the local resolution determined by Relion's implementation and FSC curve for each final masked reconstruction. (**A**) MC05 dataset. (**B**) MC06 dataset.

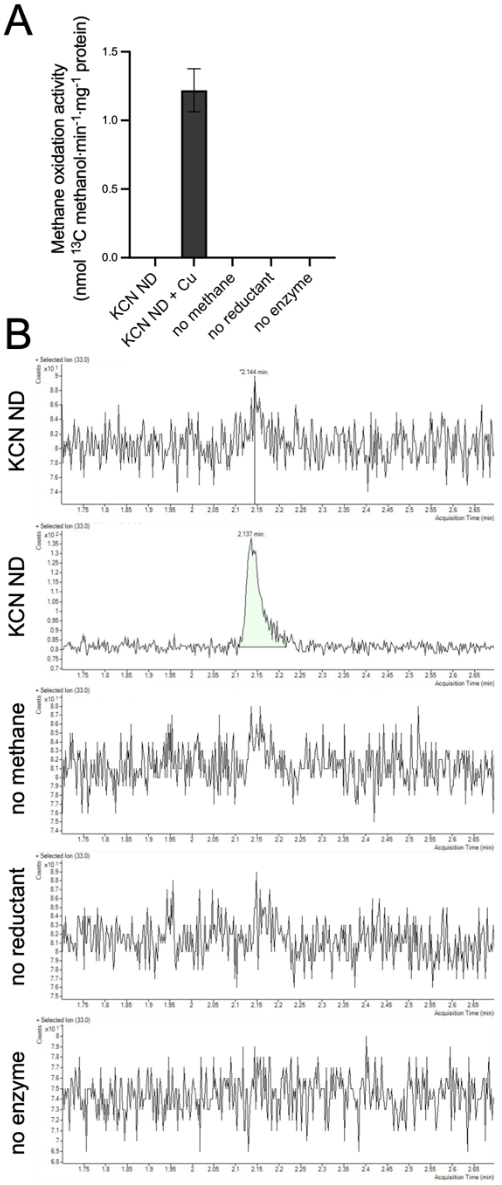

Figure S2.16. Methane oxidation by pMMO treated with potassium cyanide (KCN). (**A**) KCN ND, nanodiscs formed with pMMO from the KCN-treated membranes and native lipids; KCN ND + Cu, copper added back to KCN-treated membranes followed by pMMO isolation from those membranes and reconstitution into nanodiscs with native lipids. Error bars represent standard deviation of n = 2 biological replicates, each measured in triplicate. (**B**) GC/MS traces measuring +33 ion corresponding to [13]C-methanol for the native nanodisc sample.

Table S2.1. pMMO activity data

Sample	Methanotroph	Substrate	Reductant	Turnover number per protomer (s^{-1})	Specific activity (nmol mg total protein^{-1} min^{-1})	References
Cells producing pMMO	*M. capsulatus* (Bath)	propylene	formate	1.4-2.5[a]	167-300	[38,39]
	Ms. trichosporium OB3b	methane	NA	0.68-2.5[b]	82-300	[274,275]
Membrane-bound pMMO	*M. capsulatus* (Bath)	methane	NADH	0.083-0.146[c]	40-70	[62,63]
			duroquinol	0.026-0.042[d]	12-20	[62,63]
		propylene	NADH	0.044-0.246[e]	21-118	[38,75]
			duroquinol	0.033-0.179[e]	16-86	[38,75]
	Mc. sp. str. Rockwell	methane	NADH	0.017-0.024[d,f]	8-11.5	[62,78]
			duroquinol	0.004-0.006[d,f]	1.8-3	[62,78]
	Mt. alcaliphilum 20Z	methane	NADH	0.006[c,f]	3	[63]
			duroquinol	0	0	[63]
Purified pMMO in DDM[g]	*M. capsulatus* (Bath)	methane	NADH	0	0	[63]
			duroquinol	0.002[h,i]	1	[63], this work
	M. capsulatus (Bath)	propylene	NADH	0	0	[38,75]
			duroquinol	0.032-0.21[i,j]	18-126	[38,75]
	Mc. sp. str. Rockwell	methane	NADH	0	0	[62]
			duroquinol	0	0	[62]
	Mt. alcaliphilum 20Z	methane	NADH	0	0	[63]
			duroquinol	0	0	[63]
Purified pMMO in bicelles	*M. capsulatus* (Bath)	methane	NADH	0.009[f,h]	5.2	[63]
			duroquinol	0.006[f,h]	3.5	[63]
	Mt. alcaliphilum 20Z	methane	NADH	0	0	[63]
			duroquinol	0.007[f,h]	4.4	[63]
Purified pMMO in nanodiscs[i]						
DMPC[g]	*M. capsulatus* (Bath)	methane	duroquinol	0.005[h]	3	this work
POPC[g]	*M. capsulatus* (Bath)			0.009[h]	5.4	this work
native lipids	*M. capsulatus* (Bath)			0.012[h]	7.2	this work
POPC[g]	*Mc.* sp. str. Rockwell	methane	duroquinol	0.011[h]	6.6	[78]
POPC[e]	*Mt. alcaliphilum* 20Z	methane	duroquinol	0	0	this work

[a] Calculated from rate of propylene epoxidation monitored by gas chromatography (GC) and assuming pMMO is 20% of the total protein

[b] Calculated from rate of methane uptake and assuming that pMMO is 20% of the total protein.

[c] Calculated from rate of conversion of $^{13}CH_4$ to $^{13}CH_3OH$ monitored by GC/mass spectrometry (GC/MS) and assuming that membrane-bound protein is 80% pMMO.

[d] Calculated from rate of conversion of CH_4 to CH_3OH monitored by GC and assuming that membrane-bound protein is 80% pMMO. Values from (*10*) were converted to ^{13}C values by applying a correction factor of 0.5 (*11*).

[e] Calculated from rate of propylene epoxidation monitored by GC and assuming that membrane-bound protein is 80% pMMO.

[f] Activity assay was performed at 30 °C. All other activity assays were performed at 45 °C.

[g] Abbreviations used: DDM, n-dodecyl-β-D-maltoside; DMPC, 1,2-dimyristoyl-sn-glycero-3-phosphocholine; POPC, 1-palmitoyl-2-oleoylphosphatidylcholine.

[h] Calculated from rate of conversion of $^{13}CH_4$ to $^{13}CH_3OH$ monitored by GC/MS.

[i] The samples used for the *M. capsulatus* (Bath) pMMO crystal structure determination were not assessed for methane oxidation activity and did not exhibit propylene epoxidation activity [59].

[j] Calculated from rate of propylene epoxidation monitored by GC.

Table S2.2. CryoEM data collection, refinement, and validation statistics

Sample	**MC01**	**MC02**	**MC03**	**MC04**	**20Z01**	**RW01**	**MC05**	**MC06**
Species	*M. capsulatus* (Bath)	*M. capsulatus* (Bath)	*M. capsulatus* (Bath)	*M. capsulatus* (Bath)	*Mt. alcaliphilum* 20Z	*Mc.* sp. str. Rockwell	*M. capsulatus* (Bath)	*M. capsulatus* (Bath)
Lipid type	native	POPC	native	native	POPC	POPC	native	native
PDB code	7S4H	7S4I	7S4J	7S4K	7S4L	7S4M	7T4O	7T4P
EMDB code	24827	24828	24829	24830	24831	24832	25683	25684
Data collection and processing								
Center	PNCC	PNCC	SLAC	NCCAT	NCCAT	SLAC	PNCC	PNCC
Microscope	Titan Krios-3							
Voltage (kV)	300							
Camera	Gatan K3							
Magnification	30k	30k	40k	30k	30k	30k	40k	30k
Magnification at detector (Å/pixel)	1.02	1.02	0.86	1.05	1.07	1.04	0.84	1.07
Total e^- exp (e^-/Å^2)	54	52	50	64	64	40	50	50
Defocus range (μm)	-2.0 to -4.0							
Automation software	SerialEM							
Energy filter slit (eV)	n. a.	n. a.	20	20	20	20	n. a.	n. a.
Micrographs collected	9,081	10,889	9,966	11,593	6,564	3,565	4,601	9,405
Reconstruction								
Refined particles	1,381,649	1,477,719	881,128	546,332	443,800	490,196	394,208	812,752
Symmetry	C3							
Resolution, FSC 0.143 (Å)	2.14	2.26	2.16	2.36	2.46	2.42	3.65	3.39
Map sharpening B factor (Å^2)	-69	-70	-72	-69	-120	-101	-181	-154

Map sharpening methods	Coot							
Model composition								
Protein residues	2577	2577	2577	2577	2619	2574	2310	2574
Ligands	63	63	54	63	36	27	27	54
Waters	410	355	304	110	14	36	0	0
Model Refinement								
Refinement package	Phenix							
Real or reciprocal space	Real							
Model-Map scores								
CC	0.84	0.84	0.82	0.89	0.87	0.59	0.78	0.83
Average FSC B factors (Å^2)								
Protein Residues	43.93	41.92	49.84	68.38	74.03	141.00	85.92	21.51
Ligands	20.27	20.27	20.16	20.38	83.19	73.68	20.75	20.23
Waters	39.80	38.25	44.97	59.73	72.96	135.02	n. a.	n. a.
R.m.s. deviations								
Bond lengths (Å)	0.009	0.009	0.010	0.010	0.006	0.009	0.007	0.010
Bond Angles (°)	1.110	1.266	1.318	1.340	1.012	1.262	0.903	1.110
Validation								
MolProbity score	2.36	2.48	2.51	2.41	2.71	2.65	2.30	2.20
CaBLAM outliers	2.95	3.19	2.72	2.95	3.29	3.52	2.95	2.60
Clashscore	14.25	15.60	13.55	13.41	24.10	13.99	16.49	19.10
Rotamer outliers (%)	2.83	3.29	4.30	3.29	3.26	6.06	1.85	0.82
C-beta deviations (%)	0.13	0.00	0.04	0.13	0.00	0.08	0.00	0.13
Ramachandran plot								
Favored (%)	94.92	94.29	94.33	94.37	92.95	94.04	94.37	93.51
Outliers (%)	0.23	0.47	0.51	0.23	0.35	0.42	0.26	0.35

APPENDIX B: Supplemental data for chapter 3

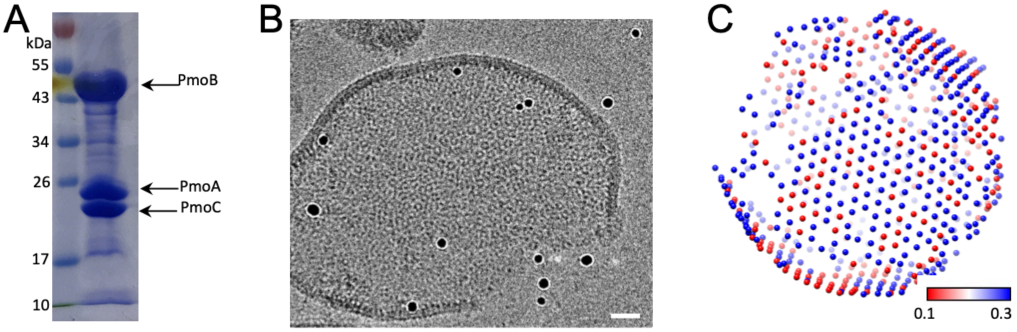

Figure S3.1. CryoET of isolated intracytoplasmic membranes. (A) SDS-PAGE of isolated membranes containing pMMO. Three most abundant proteins are labeled. (B) A projection of isolated intracytoplasmic membrane. (C) emClarity template matching results using the 7-particle unit as a template, colored by the cross-correlation values (0.1-0.3) from highest (blue) to lowest (red). Scale bar, 50 nm

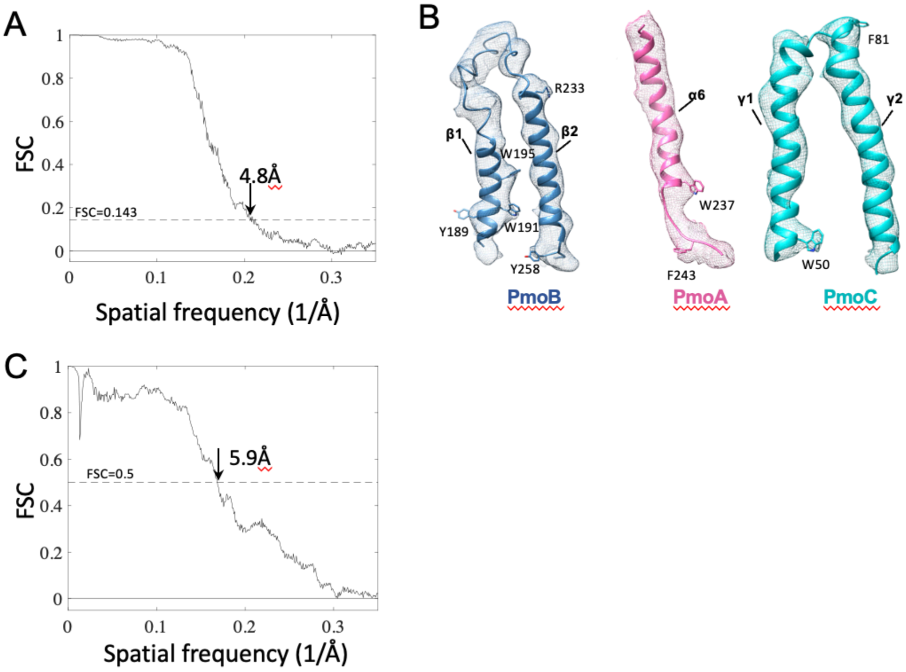

Figure S3.2. CryoET STA of pMMO trimer. (A) Fourier Shell Correlation (FSC) plot of pMMO trimer. The resolution is indicated at the FSC value of 0.143. (B) Representative alpha helix densities from PmoA, PmoB and PmoC, superimposed with the structure model (PDB: 3RGB), with some bulky amino acids labeled. (C) Fourier Shell Correlation (FSC) plot of pMMO trimer map with pMMO structure model from nanodisc (PDB: 7S4H).

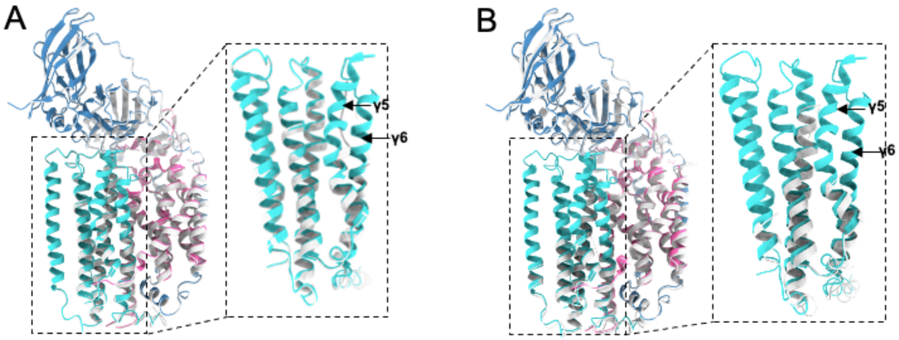

Figure S3.3 Comparison of cryoET STA structure with published structures. A) Comparison of cryoET STA structure with X-ray crystal structure (PDB:3RGB, grey). B) Comparison of cryoET STA structure with cryoEM SPA structure (PDB:7EV9, grey). Inset, enlarged view of boxed region, showing PmoC only. Arrows indicate the newly resolved helices, γ5 and γ6, in the cryoET STA structure.

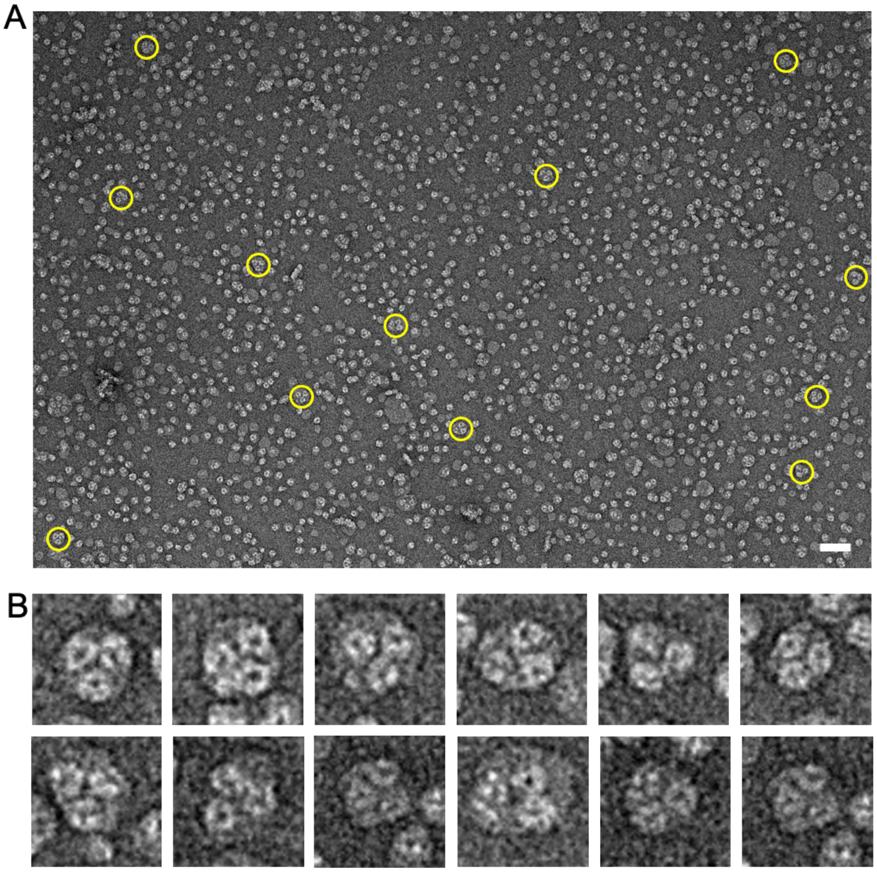

Figure S3.4. EM characterization of pMMO reconstituted in lipid nanodiscs. (A) A projection image of negatively stained pMMO particles in MSP2N2 nanodiscs. Circled nanodiscs contain three pMMO particles. (B) Gallery of enlarged views of the circled nanodiscs. Scale bar, 50 nm

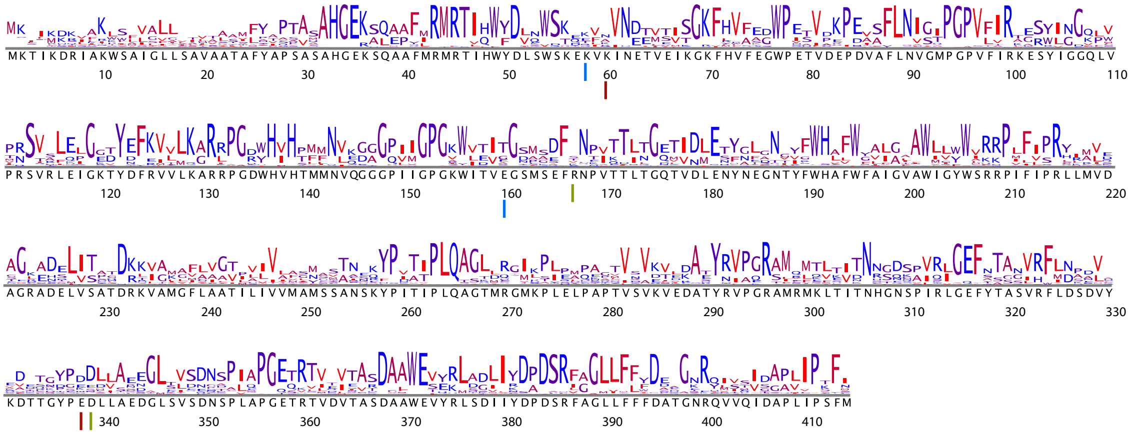

Figure S3.5. Sequence conservation logo for PmoB from type I methanotrophs. The logo was generated from 175 sequences from alphaproteobacterial methanotrophs aligned using a hidden Markov model from pfam PF04744. Residues are colored by hydrophobicity with blue as hydrophilic and red as hydrophobic. Residues that are modeled for having salt bridges are labeled by matching colored lines (blue, red, green). The sequence shown in black is of PmoB from *M. capsulatus* (Bath).

Data acquisition	
Microscope	Titan Krios
Voltage (keV)	300
Detector	Gatan Quantum K3 Direct Electron Detector
Energy-filter	Yes
Slit width (eV)	20
Super-resolution mode	No
Å/pixel	1.34
Defocus range (µm)	-2.5 to -6
Defocus increment (µm)	0.3
Acquisition scheme	Dose-Symmetric, -63/63, 3^{o} step, group 3
Total Dose (electrons/Å^{2})	129
Number of Frames	10
Number of Tomograms	187
Structure determination	
No. of subotomograms	127,417
Resolution (Å)	4.8
b-factor applied	-50
Data deposited	EMD-14399, EMD-14530

Table S3.1. CryoET data collection and structure determination of pMMO trimer from isolated intracytoplasmic membrane.

EMDB ID	**Res***	**Sample information**	**Ref**
EMD-4315	9.1	OST-containing ribosome-translocon complexes from canine rough microsomal membranes	(35)
EMD-8330	6.4	Outer membrane pore complex PilQ in Pelagibacter cell	**
EMD-10840	9.1	Structure of RyR1 in apo/closed state in native membrane	(36)
EMD-10752	7.7	Hexagon bounding clathrin leg in clathrin coats assembled on a membrane	(37)
EMD-10753	7.7	Pentagon bounding clathrin legs in clathrin coats assembled on a membrane	(37)
EMD-21411	9.4	HIV envelope glycoprotein bound with soluble CD4 (D1-D2) and antibody 17b on AT-2 treated BaL strain virus	(38)
EMD-21413	9.9	HIV envelope glycoprotein bound with antibodies 10-1074 and 3BNC117 on AT-2 treated BaL strain virus	(38)
EMD-10050	8.4	Structure of the E. coli Chemotaxis Core Signalling Unit	(28)
EMD-25178	9.1	STA structure of HIV-1 Envelope protein in native membrane	(39)
EMD-14399	4.8	STA of pMMO trimer in intracytoplasmic membranes	***

* The achieved resolution in Å.
** not published
*** This study

Table S3.2. Summary of EMDB depositions of *in situ* membrane protein structures determined by cryoET STA.

APPENDIX C: Supplemental data for chapter 4

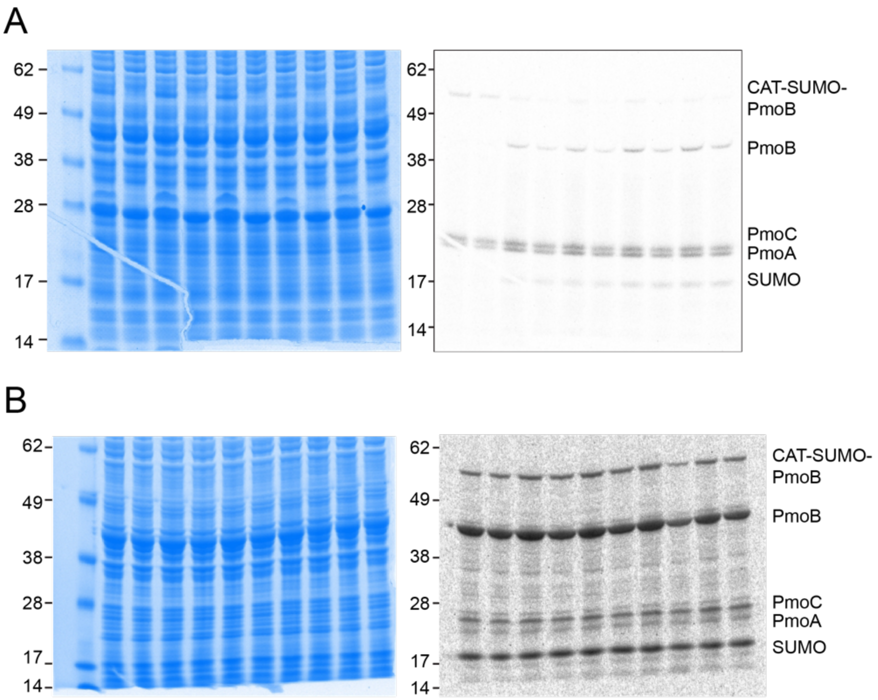

Figure S4.1. Gel comparison for molecular weight (MW) marker position. Gel used for autoradiogram exposure was imaged, showing the position of the MW markers (SeeBlue, ThermoFisher). (A) Copper titration gel from Fig. 4.3. (B) Polycistronic gel (fig. S4.2B)

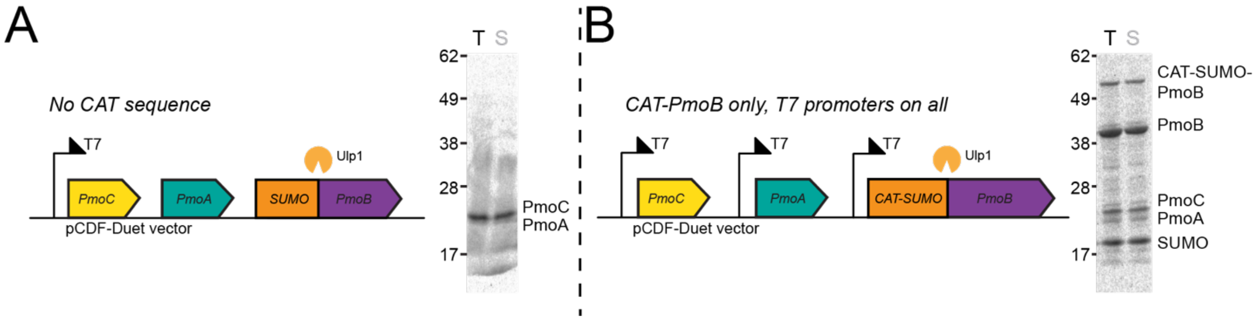

Figure S4.2. Strategies for producing pMMO from a single plasmid. (A) A single promoter with no CAT sequence. (B) Each gene with its own promoter and a CAT sequence on pMOB

REFERENCES

1 Fletcher, S. E. M. & Schaefer, H. Rising methane: A new climate challenge. *Science* **364**, 932-933, doi:10.1126/science.aax1828 (2019).

2 Saunois, M., Jackson, R. B., Bosquet, P., PPoulter, B. & Canadell, J. G. The growing role of methane in anthropogenic climate change. *Environ. Res. Lett.* **11**, doi:10.1088/1748-9326/11/12/120207 (2016).

3 Myhre, G., D. Shindell, F.-M. Bréon, W. Collins, J. Fuglestvedt, J. Huang, D. Koch, J.-F. Lamarque, D. Lee, B. Mendoza, T. Nakajima, A. Robock, G. Stephens, T. Takemura and H. Zhang. in *In: Climate Change 2013: The Physical Science Basis. Contribution of Working Group I to the Fifth Assessment Report of the Intergovernmental Panel on Climate Change* (ed T.F. Stocker, D. Qin, G.-K. Plattner, M. Tignor, S.K. Allen, J. Boschung, A. Nauels, Y. Xia, V. Bex and P.M. Midgley) (Cambridge University Press, 2013).

4 Haynes, C. A. & Gonzalez, R. Rethinking biological activation of methane and conversion to liquid fuels. *Nat. Chem. Biol.* **10**, 331-339, doi:10.1038/nchembio.1509 (2014).

5 Blanksby, S. J. & Ellison, G. B. Bond dissociation energies of organic molecules. *Acc. Chem. Res.* **36**, 255-263, doi:10.1021/ar020230d (2003).

6 Wood, D. A., Nwaoha, C. & Towler, B. F. Gas-to-liquids (GTL): A review of an industry offering several routes for monetizing natural gas. *J. Nat. Gas Sci. Eng.* **9**, 196-208, doi:10.1016/j.jngse.2012.07.001 (2012).

7 Ge, X. M., Yang, L. C., Sheets, J. P., Yu, Z. T. & Li, Y. B. Biological conversion of methane to liquid fuels: Status and opportunities. *Biotech. Adv.* **32**, 1460-1475, doi:10.1016/j.biotechadv.2014.09.004 (2014).

8 Lawton, T. J. & Rosenzweig, A. C. Biocatalysts for methane conversion: Big progress on breaking a small substrate. *Curr. Opin. Chem. Biol.* **35**, 142-149, doi:10.1016/j.cbpa.2016.10.001 (2016).

9 Clomburg, J. M., Crumbley, A. M. & Gonzalez, R. Industrial biomanufacturing: The future of chemical production. *Science* **355**, doi:10.1126/science.aag0804 (2017).

10 Hanson, R. S. & Hanson, T. E. Methanotrophic bacteria. *Microbiol. Rev.* **60**, 439-471, doi:10.1128/mr.60.2.439-471.1996 (1996).

11 Semrau, J. D., Dispirito, A. A. & Yoon, S. Methanotrophs and copper. *FEMS Microbiol. Lett.* **34**, 496-531, doi:10.1111/j.1574-6976.2010.00212.x (2010).

12 Kwon, M., Ho, A. & Yoon, S. Novel approaches and reasons to isolate methanotrophic bacteria with biotechnological potentials: recent achievements and perspectives. *Appl. Microbiol. Biotechnol.* **103**, 1-8, doi:10.1007/s00253-018-9435-1 (2019).

13 Henard, C. A. *et al.* Biogas biocatalysis: Methanotrophic bacterial cultivation, metabolite profiling, and bioconversion to lactic acid. *Front. Microbiol.* **9**, 2610, doi:10.3389/fmicb.2018.02610 (2018).

14 Strong, P. J., Xie, S. & Clarke, W. P. Methane as a resource: Can the methanotrophs add value? *Environ. Sci. Technol.* **49**, 4001-4018, doi:10.1021/es504242n (2015).

15 Bowman, J. P., Sly, L. I. & Stackebrandt, E. The phylogenetic position of the family Methylococcaceae. *Int. J. Syst. Bacteriol.* **45**, 182-185, doi:10.1099/00207713-45-1-182 (1995).

16 Kalyuzhnaya, M. G., Puri, A. W. & Lidstrom, M. E. Metabolic engineering in methanotrophic bacteria. *Metab. Eng.* **29**, 142-152, doi:10.1016/j.ymben.2015.03.010 (2015).

17 Davies, S. L. & Whittenbury, R. Fine structure of methane and other hydrocarbon-utilizing bacteria. *J. Gen. Microbiol.* **61**, 227-232, doi:10.1099/00221287-61-2-227 (1970).

18 Makula, R. A. Phospholipid composition of methane-oxidizing bacteria. *J. Bacteriol.* **134**, 771-777 (1978).

19 Knief, C. Diversity and habitat preferences of cultivated and uncultivated aerobic methanotrophic bacteria evaluated based on pmoA as molecular marker. *Front. Microbiol.* **6**, 1346, doi:10.3389/fmicb.2015.01346 (2015).

20 Op den Camp, H. J. *et al.* Environmental, genomic and taxonomic perspectives on methanotrophic Verrucomicrobia. *Environ. Microbiol. Rep.* **1**, 293-306, doi:10.1111/j.1758-2229.2009.00022.x. (2009).

21 Khadem, A. F. *et al.* Autotrophic methanotrophy in verrucomicrobia: *Methylacidiphilum fumariolicum* SolV uses the Calvin-Benson-Bassham cycle for carbon dioxide fixation. *J. Bacteriol.* **193**, 4438-4446, doi:10.1128/JB.00407-11 (2011).

22 van Teeseling, M. C. *et al.* Expanding the verrucomicrobial methanotrophic world: Description of three novel species of *Methylacidimicrobium* gen. nov. *Appl. Environ. Microbiol.* **80**, 6782-6791, doi:10.1128/AEM.01838-14 (2014).

23 Bowman, J. P., McCammon, S. A. & Skerratt, J. H. *Methylosphaera hansonii* gen. nov., sp. nov., a psychrophilic, group I methanotroph from Antarctic marine-salinity, meromictic lakes. *Microbiol.* **143**, 1451-1459, doi:10.1099/00221287-143-4-1451. (1997).

24 Kalyuzhnaya, M. G. *et al.* A new moderately halophilic methanotroph of the genus *Methylobacter*. *Mikrobiologiia* **67**, 438-444, doi:10.1023/B:MICI.0000036991.31677.13 (1998).

25 Khmelenina, V. N., Kalyuzhnaya, M. G., Starostina, N. G., Suzina, N. E. & Trotsenko, Y. A. Isolation and characterization of halotolerant alkaliphilic methanotrophic bacteria from Tuva Soda Lakes. *Curr. Microbiol.* **35**, 257-261, doi:10.1007/s002849900249 (1997).

26 Pol, A. *et al.* Methanotrophy below pH1 by a new Verrucomicrobia species. *Nature* **450**, 874-878, doi:10.1038/nature06222 (2007).

27 Hou, S. B. *et al.* Complete genome sequence of the extremely acidophilic methanotroph isolate V4, *Methylacidiphilum infernorum*, a representative of the bacterial phylum Verrucomicrobia. *Biol. Direct* **3**, doi:10.1186/1745-6150-3-26 (2008).

28 Dunfield, P. F. *et al.* Methane oxidation by an extremely acidophilic bacterium of the phylum Verrucomicrobia. *Nature* **450**, 879-882, doi:https://doi.org/10.1038/nature06411 (2007).

29 Islam, T., Jensen, S., Reigstad, L. J., Larsen, O. & Birkeland, N. K. Methane oxidation at 55°C and pH 2 by a thermoacidophilic bacterium belonging to the *Verrucomicrobia* phylum. *Proc. Natl. Acad. Sci. USA* **105**, 300-304, doi:10.1073/pnas.0704162105 (2008).

30 Ross, M. O. & Rosenzweig, A. C. A tale of two methane monooxygenases. *J. Biol. Inorg. Chem.* **22**, 307-319, doi:10.1007/s00775-016-1419-y (2017).

31 Sirajuddin, S. & Rosenzweig, A. C. Enzymatic oxidation of methane. *Biochemistry* **54**, 2283-2294, doi:10.1021/acs.biochem.5b00198 (2015).

32 Banerjee, R., Jones, J. C. & Lipscomb, J. D. Soluble methane monooxygenase. *Annu. Rev. Biochem.* **88**, 409-431, doi:10.1146/annurev-biochem-013118-111529 (2019).

33 Dunfield, P. F., Khmelenina, V. N., Suzina, N. E., Trotsenko, Y. A. & Dedysh, S. N. *Methylocella silvestris* sp. nov., a novel methanotroph isolated from an acidic forest cambisol. *Int. J. Syst. Evol. Microbiol.* **53**, 1231-1239, doi:10.1099/ijs.0.02481-0 (2003).

34 Dedysh, S. N., Knief, C. & Dunfield, P. F. *Methylocella* species are facultatively methanotrophic. *J. Bacteriol.* **187**, 4665-4670, doi:10.1128/JB.187.13.4665-4670.2005 (2005).

35 Vorobev, A. V. *et al. Methyloferula stellata* gen. nov., sp. nov., an acidophilic, obligately methanotrophic bacterium that possesses only a soluble methane monooxygenase. *Int. J. Syst. Evol. Microbiol.* **61**, 2456-2463, doi:10.1099/ijs.0.028118-0 (2011).

36 Whittenbury, R., Phillips, K. C. & Wilkinson, J. F. Enrichment, isolation and some properties of methane-utilizing bacteria. *J. Gen. Microbiol.* **61**, 205-218, doi:10.1099/00221287-61-2-205 (1970).

37 Prior, S. D. & Dalton, H. The effect of copper ions on membrane content and methane monooxygenase activity in methanol-grown cells of *Methylococcus capsulatus* (Bath). *J. Gen. Microbiol.* **131**, 155-163, doi:10.1099/00221287-131-1-155 (1985).

38 Choi, D. W. *et al.* The membrane-associated methane monooxygenase pMMO and pMMO-NADH:quinone oxidoreductase complex from *Methylococcus capsulatus* Bath. *J. Bacteriol.* **185**, 5755-5764, doi:10.1128/JB.185.19.5755-5764.2003 (2003).

39 Martinho, M. *et al.* Mössbauer studies of the membrane-associated methane monooxygenase from *Methylococcus capsulatus* Bath: Evidence for a diiron center. *J. Am. Chem. Soc.* **129**, 15783-15785, doi:10.1021/ja077682b (2007).

40 Stanley, S. H., Prior, S. D., Leak, D. J. & Dalton, H. Copper stress underlies the fundamental change in intracellular location of methane monooxygenase in methane oxidizing organisms: studies in batch and continuous cultures. *Biotechnol. Lett.* **5**, 487-492, doi:10.1007/BF00132233 (1983).

41 Nielsen, A. K., Gerdes, K. & Murrell, J. C. Copper-dependent transcriptional regulation of methane monooxygenase genes in *Methylococcus capsulatus* and *Methylosinus trichosporium*. *Mol. Microbiol.* **25**, 399-409, doi:10.1046/j.1365-2958.1997.4801846.x (1997).

42 Kenney, G. E., Sadek, M. & Rosenzweig, A. C. Copper-responsive gene expression in the methanotroph *Methylosinus trichosporium* OB3b. *Metallomics* **8**, 931-940, doi:10.1039/c5mt00289c (2016).

43 Jahng, D. & Wood, T. K. Trichloroethylene and chloroform degradation by a recombinant pseudomonad expressing soluble methane monooxygenase from *Methylosinus trichosporium* OB3b. *Appl. Environ. Microbiol.* **60**, 2473-2482, doi:10.1128/aem.60.7.2473-2482.1994 (1994).

44 Murrell, J. C., Gilbert, B. & McDonald, I. R. Molecular biology and regulation of methane monooxygenase. *Arch. Microbiol.* **173**, 325-332, doi:10.1007/s002030000158 (2000).

45 Gou, Z. *et al.* Functional expression of the particulate methane mono-oxygenase gene in recombinant *Rhodococcus erythropolis*. *FEMS Microbiol. Lett.* **263**, 136-141, doi:10.1111/j.1574-6968.2006.00363.x (2006).

46 Balasubramanian, R., Smith, S. M., Rawat, S., Stemmler, T. L. & Rosenzweig, A. C. Oxidation of methane by a biological dicopper centre. *Nature* **465**, 115-119, doi:10.1038/nature08992 (2010).

47 Kruse, T., Ratnadevi, C. M., Erikstad, H. A. & Birkeland, N. K. Complete genome sequence analysis of the thermoacidophilic verrucomicrobial methanotroph "Candidatus Methylacidiphilum kamchatkense" strain Kam1 and comparison with its closest relatives. *BMC Genomics* **20**, 642, doi:10.1186/s12864-019-5995-4 (2019).

48 Anvar, S. Y. *et al.* The genomic landscape of the verrucomicrobial methanotroph *Methylacidiphilum fumariolicum* SolV. *BMC Genomics* **15**, 914, doi:10.1186/1471-2164-15-914 (2014).

49 del Cerro, C. *et al.* Genome sequence of the methanotrophic poly-β-hydroxybutyrate producer *Methylocystis parvus* OBBP. *J. Bacteriol.* **194**, 5709-5710, doi:10.1128/jb.01346-12 (2012).

50 Vuilleumier, S. *et al.* Genome sequence of the haloalkaliphilic methanotrophic bacterium *Methylomicrobium alcaliphilum* 20Z. *J. Bacteriol.* **194**, 551-552, doi:10.1128/jb.06392-11 (2012).

51 Stein, L. Y. *et al.* Genome sequence of the methanotrophic alphaproteobacterium *Methylocystis* sp. strain Rockwell (ATCC 49242). *J. Bacteriol.* **193**, 2668-2669, doi:10.1128/jb.00278-11 (2011).

52 Svenning, M. M. *et al.* Genome sequence of the arctic methanotroph *Methylobacter tundripaludum* SV96. *J. Bacteriol.* **193**, 6418-6419, doi:10.1128/jb.05380-11 (2011).

53 Chen, Y. *et al.* Complete genome sequence of the aerobic facultative methanotroph *Methylocella silvestris* BL2. *J. Bacteriol.* **192**, 3840-3841, doi:10.1128/jb.00506-10 (2010).

54 Stein, L. Y. *et al.* Genome sequence of the obligate methanotroph *Methylosinus trichosporium* strain OB3b. *J. Bacteriol.* **192**, 6497-6498, doi:10.1128/JB.01144-10 (2010).

55 Ward, N. *et al.* Genomic insights into methanotrophy: The complete genome sequence of *Methylococcus capsulatus* (Bath). *PLoS Biol.* **2**, e303, doi:10.1371/journal.pbio.0020303 (2004).

56 Stolyar, S., Costello, A. M., Peeples, T. L. & Lidstrom, M. E. Role of multiple gene copies in particulate methane monooxygenase activity in the methane-oxidizing bacterium *Methylococcus capsulatus* Bath. *Microbiol.* **145**, 1235-1244, doi:10.1099/13500872-145-5-1235 (1999).

57 Semrau, J. D. *et al.* Particulate methane monooxygenase genes in methanotrophs. *J. Bacteriol.* **177**, 3071-3079, doi:10.1128/jb.177.11.3071-3079.1995 (1995).

58 McDonald, I. R. & Murrell, J. C. The particulate methane monooxygenase gene pmoA and its use as a functional gene probe for methanotrophs. *FEMS Microbiol. Lett.* **156**, 205-210, doi:10.1111/j.1574-6968.1997.tb12728.x (1997).

59 Lieberman, R. L. & Rosenzweig, A. C. Crystal structure of a membrane-bound metalloenzyme that catalyses the biological oxidation of methane. *Nature* **434**, 177-182, doi:10.1038/nature03311 (2005).

60 Hakemian, A. S. *et al.* The metal centers of particulate methane monooxygenase from *Methylosinus trichosporium* OB3b. *Biochemistry* **47**, 6793-6801, doi:10.1021/bi800598h (2008).

61 Smith, S. M. *et al.* Crystal structure and characterization of particulate methane monooxygenase from *Methylocystis* species strain M. *Biochemistry* **50**, 10231-10240, doi:10.1021/bi200801z (2011).

62 Sirajuddin, S. *et al.* Effects of zinc on particulate methane monooxygenase activity and structure. *J. Biol. Chem.* **289**, 21782-21794, doi:10.1074/jbc.M114.581363 (2014).

63 Ro, S. Y. *et al.* From micelles to bicelles: Effect of the membrane on particulate methane monooxygenase activity. *J. Biol. Chem.* **293**, 10457-10465, doi:10.1074/jbc.RA118.003348 (2018).

64 Zhu, J. *et al.* Structure of subcomplex Iβ of mammalian respiratory complex I leads to new supernumerary subunit assignments. *Proc. Natl. Acad. Sci. U S A* **112**, 12087-12092, doi:10.1073/pnas.1510577112 (2015).

65 Hakemian, A. S. *et al.* The metal centers of particulate methane monooxygenase from Methylosinus trichosporium OB3b. *Biochemistry* **47**, 6793-6801, doi:10.1021/bi800598h (2008).

66 Gerlt, J. A. *et al.* Enzyme Function Initiative-Enzyme Similarity Tool (EFI-EST): A web tool for generating protein sequence similarity networks. *Biochim. Biophys. Acta* **1854**, 1019-1037, doi:10.1016/j.bbapap.2015.04.015 (2015).

67 Arp, D. J., Sayavedra-Soto, L. A. & Hommes, N. G. Molecular biology and biochemistry of ammonia oxidation by *Nitrosomonas europaea*. *Arch. Microbiol.* **178**, 250-255, doi:10.1007/s00203-002-0452-0 (2002).

68 Liew, E. F., Tong, D. C., Coleman, N. V. & Holmes, A. J. Mutagenesis of the hydrocarbon monooxygenase indicates a metal centre in subunit-C, and not subunit-B, is essential for copper-containing membrane monooxygenase activity. *Microbiol.* **160**, 1267-1277, doi:10.1099/mic.0.078584-0 (2014).

69 Lawton, T. J., Ham, J., Sun, T. & Rosenzweig, A. C. Structural conservation of the B subunit in the ammonia monooxygenase/particulate methane monooxygenase superfamily. *Proteins* **82**, 2263-2267, doi:10.1002/prot.24535 (2014).

70 Lemos, S. S., Collins, M. L. P., Eaton, S. S., Eaton, G. R. & Antholine, W. E. Comparison of EPR-visible Cu^{2+} sites in pMMO from *Methylococcus capsulatus* (Bath) and *Methlyomicrobium album* BG8. *Biophys. J.* **79**, 1085-1094, doi:10.1016/s0006-3495(00)76362-4 (2000).

71 Ross, M. O. *et al.* Particulate methane monooxygenase contains only mononuclear copper centers. *Science* **364**, 566-570, doi:10.1126/science.aav2572 (2019).

72 Koo, C. W. & Rosenzweig, A. C. in *Encyclopedia of Inorganic and Bioinorganic Chemistry* (ed R. A. Scott) (John Wiley & Sons, Ltd, 2020).

73 Ciano, L., Davies, G. J., Tolman, W. B. & Walton, P. H. Bracing copper for the catalytic oxidation of C-H bonds. *Nat. Catal.* **1**, 571-577, doi:10.1038/s41929-018-0110-9 (2018).

74 Walton, P. H. & Davies, G. J. On the catalytic mechanisms of lytic polysaccharide monooxygenases. *Curr. Opin. Chem. Biol.* **31**, 195-207, doi:10.1016/j.cbpa.2016.04.001 (2016).

75 Lieberman, R. L. *et al.* Purified particulate methane monooxygenase from *Methylococcus capsulatus* (Bath) is a dimer with both mononuclear copper and a copper-containing

cluster. *Proc. Natl. Acad. Sci. USA* **100**, 3820-3825, doi:10.1073/pnas.0536703100 (2003).

76 Lieberman, R. L. *et al.* Characterization of the particulate methane monooxygenase metal centers in multiple redox states by X-ray absorption spectroscopy. *Inorg. Chem.* **45**, 8372-8381, doi:10.1021/ic060739v (2006).

77 Cao, L. L., Caldararu, O., Rosenzweig, A. C. & Ryde, U. Quantum refinement does not support dinuclear copper sites in crystal structures of particulate methane monooxygenase. *Angew. Chem. Int. Ed.* **57**, 162-166, doi:10.1002/anie.201708977 (2018).

78 Ro, S. Y. *et al.* Native top-down mass spectrometry provides insights into the copper centers of membrane-bound methane monooxygenase. *Nat. Commun.* **10**, 2675, doi:10.1038/s41467-019-10590-6 (2019).

79 Shiota, Y., Juhasz, G. & Yoshizawa, K. Role of tyrosine residue in methane activation at the dicopper site of particulate methane monooxygenase: A density functional theory study. *Inorg. Chem.* **52**, 7907-7917, doi:10.1021/ic400417d (2013).

80 Shiota, Y. & Yoshizawa, K. Comparison of the reactivity of bis(μ-oxo)$Cu^{II}Cu^{III}$ and $Cu^{III}Cu^{III}$ species to methane. *Inorg. Chem.* **48**, 838-845, doi:10.1021/ic8003933 (2009).

81 Yoshizawa, K. & Shiota, Y. Conversion of methane to methanol at the mononuclear and dinuclear copper sites of particulate methane monooxygenase (pMMO): A DFT and QM/MM study. *J. Am. Chem. Soc.* **128**, 9873-9881, doi:10.1021/ja061604r (2006).

82 Kim, H. J. *et al.* Biological conversion of methane to methanol through genetic reassembly of native catalytic domains. *Nat. Catal.* **2**, 342-353, doi:10.1038/s41929-019-0255-1 (2019).

83 Nyerges, G. & Stein, L. Y. Ammonia cometabolism and product inhibition vary considerably among species of methanotrophic bacteria. *FEMS Microbiol. Lett.* **297**, 131-136, doi:10.1111/j.1574-6968.2009.01674.x (2009).

84 Stein, L. Y. & Arp, D. J. Loss of ammonia monooxygenase activity in nitrosomonas europaea upon exposure to nitrite. *Appl. Environ. Microbiol.* **64**, 4098-4102, doi:10.1128/AEM.64.10.4098-4102.1998 (1998).

85 Coleman, N. V. *et al.* Hydrocarbon monooxygenase in *Mycobacterium*: Recombinant expression of a member of the ammonia monooxygenase superfamily. *Isme J.* **6**, 171-182, doi:10.1038/ismej.2011.98 (2012).

86 Smith, D. D. S. & Dalton, H. Solubilisation of methane monooxygenase from *Methylococcus capsulatus* (Bath). *Eur. J. Biochem.* **182**, 667-671, doi:10.1111/j.1432-1033.1989.tb14877.x (1989).

87 Shiemke, A. K., Cook, S. A. & Miley, T. Quinols as electron donors for detergent solubilized and membrane-bound methane monooxygenase. *J. Inorg. Biochem.* **59**, 385, doi:10.1016/0162-0134(95)97483-7 (1995).

88 Heinrich, H. & Werner, S. Identification of the ubiquinone-binding site of NADH-ubiquinone oxidoreductase (complex I) from *Neurospora crassa*. *Biochemistry* **31**, 11413-11419, doi:10.1021/bi00161a020 (1992).

89 Cook, S. A. & Shiemke, A. K. Evidence that a type-2 NADH:quinone oxidoreductase mediates electron transfer to particulate methane monooxygenase in *Methylococcus capsulatus*. *Arch. Biochem. Biophys.* **398**, 32-40, doi:10.1006/abbi.2001.2628 (2002).

90 de la Torre, A. *et al.* Genome-scale metabolic reconstructions and theoretical investigation of methane conversion in *Methylomicrobium buryatense* strain 5G(B1). *Microb. Cell Fact.* **14**, 188, doi:10.1186/s12934-015-0377-3 (2015).

91 Leak, D. J. & Dalton, H. Growth yields of methanotrophs. 2. A Theoretical analysis. *Appl. Microbiol. Biotechnol.* **23**, 477-481 (1986).

92 Lieven, C. *et al.* A genome-scale metabolic model for *Methylococcus capsulatus* (Bath) suggests reduced efficiency electron transfer to the particulate methane monooxygenase. *Front. Microbiol.* **9**, 15, doi:10.3389/fmicb.2018.02947 (2018).

93 Bordel, S. *et al.* Genome scale metabolic modeling reveals the metabolic potential of three Type II methanotrophs of the genus *Methylocystis*. *Metab. Eng.* **54**, 191-199, doi:10.1016/j.ymben.2019.04.001 (2019).

94 Bordel, S., Rojas, A. & Munoz, R. Reconstruction of a genome scale metabolic model of the polyhydroxybutyrate producing methanotroph *Methylocystis parvus* OBBP. *Microb. Cell Fact.* **18**, 104, doi:10.1186/s12934-019-1154-5 (2019).

95 Nguyen, A. D. *et al.* Genome-scale evaluation of core one-carbon metabolism in gammaproteobacterial methanotrophs grown on methane and methanol. *Metab. Eng.* **57**, 1-12, doi:10.1016/j.ymben.2019.10.004 (2020).

96 Naizabekov, S. & Lee, E. Y. Genome-scale metabolic model reconstruction and in silico investigations of methane metabolism in *Methylosinus trichosporium* OB3b. *Microorganisms* **8**, doi:10.3390/microorganisms8030437 (2020).

97 Myronova, N., Kitmitto, A., Collins, R. F., Miyaji, A. & Dalton, H. Three-dimensional structure determination of a protein supercomplex that oxidizes methane to formaldehyde in *Methylococcus capsulatus* (Bath). *Biochemistry* **45**, 11905-11914, doi:10.1021/bi061294p (2006).

98 Culpepper, M. A. & Rosenzweig, A. C. Structure and protein-protein interactions of methanol dehydrogenase from *Methylococcus capsulatus* (Bath). *Biochemistry* **53**, 6211-6219, doi:10.1021/bi500850j (2014).

99 Deng, Y. W., Ro, S. Y. & Rosenzweig, A. C. Structure and function of the lanthanide-dependent methanol dehydrogenase XoxF from the methanotroph *Methylomicrobium buryatense* 5GB1C. *J. Biol. Inorg. Chem.*, doi:10.1007/s00775-018-1604-2 (2018).

100 Fisher, O. S. *et al.* Characterization of a long overlooked copper protein from methane- and ammonia-oxidizing bacteria. *Nat. Commun.* **9**, 4276, doi:10.1038/s41467-018-06681-5 (2018).

101 Murrell, J. C. Molecular genetics of methane oxidation. *Biodeg.* **5**, 145-159, doi:10.1007/BF00696456 (1994).

102 Lee, S.-K., Nesheim, J. C. & Lipscomb, J. D. Transient intermediates of the methane monooxygenase catalytic cycle. *J. Biol. Chem.* **268**, 21569-21577, doi:10.1016/S0021-9258(20)80579-1 (1993).

103 Liu, Y., Nesheim, J. C., Lee, S. K. & Lipscomb, J. D. Gating effects of component B on oxygen activation by the methane monooxygenase hydroxylase component. *J. Biol. Chem.* **270**, 24662-24665, doi:10.1074/jbc.270.42.24662 (1995).

104 Merkx, M. & Lippard, S. J. Why OrfY? Characterization of *mmoD*, a long overlooked component of the soluble methane monooxygenase from *Methylococcus capsulatus* (Bath). *J. Biol. Chem.* **277**, 5858-5865, doi:10.1074/jbc.M107712200 (2002).

105 Sazinsky, M. H., Merkx, M., Cadieux, E., Tang, S. Y. & Lippard, S. J. Preparation and X-ray structures of metal-free, dicobalt and dimanganese forms of soluble methane monooxygenase hydroxylase from *Methylococcus capsulatus* (Bath). *Biochemistry* **43**, 16263-16276, doi:10.1021/bi048140z (2004).

106 Rosenzweig, A. C., Frederick, C. A., Lippard, S. J. & Nordlund, P. Crystal structure of a bacterial non-haem iron hydroxylase that catalyses the biological oxidation of methane. *Nature* **366**, 537-543, doi:10.1038/366537a0 (1993).

107 Elango, N. *et al.* Crystal structure of the hydroxylase component of methane monooxygenase from *Methylosinus trichosporium* OB3b. *Protein Sci.* **6**, 556-568, doi:10.1002/pro.5560060305 (1997).

108 Rosenzweig, A. C., Nordlund, P., Takahara, P. M., Frederick, C. A. & Lippard, S. J. Geometry of the soluble methane monooxygenase catalytic diiron center in two oxidation states. *Chem. Biol.* **2**, 409-418, doi:10.1016/1074-5521(95)90222-8 (1995).

109 Srinivas, V. *et al.* High resolution XFEL structure of the soluble methane monooxygenase hydroxylase complex with its regulatory component at ambient temperature in two oxidation states. *J. Am. Chem. Soc.* **142**, 14249-14266, doi:10.1021/jacs.0c05613 (2020).

110 Walters, K. J., Gassner, G. T., Lippard, S. J. & Wagner, G. Structure of the soluble methane monooxygenase regulatory protein B. *Proc. Natl. Acad. Sci. USA* **96**, 7877-7882, doi:10.1073/pnas.96.14.7877 (1999).

111 Chang, S. L., Wallar, B. J., Lipscomb, J. D. & Mayo, K. H. Solution structure of component B from methane monooxygenase derived through heteronuclear NMR and molecular modeling. *Biochemistry* **38**, 5799-5812, doi:10.1021/bi982992f (1999).

112 Müller, J., Lugovskoy, A. A., Wagner, G. & Lippard, S. J. NMR structure of the [2Fe-2S] ferredoxin domain from soluble methane monooxygenase reductase and interaction with its hydroxylase. *Biochemistry* **41**, 42-51, doi:10.1021/bi015668k (2002).

113 Chatwood, L. L., Muller, J., Gross, J. D., Wagner, G. & Lippard, S. J. NMR structure of the flavin domain from soluble methane monooxygenase reductase from *Methylococcus capsulatus* (Bath). *Biochemistry* **43**, 11983-11991, doi:10.1021/bi049066n (2004).

114 Lee, S. J., McCormick, M. S., Lippard, S. J. & Cho, U.-S. Control of substrate access to the active site in methane monooxygenase. *Nature* **494**, 380-384, doi:10.1038/nature11880 (2013).

115 Kim, H. *et al.* MMOD-induced structural changes of hydroxylase in soluble methane monooxygenase. *Science advances* **5**, eaax0059, doi:10.1126/sciadv.aax0059 (2019).

116 Wang, W. X., Iacob, R. E., Luoh, R. P., Engen, J. R. & Lippard, S. J. Electron transfer control in soluble methane monooxygenase. *J. Am. Chem. Soc.* **136**, 9754-9762, doi:10.1021/ja504688z (2014).

117 Kopp, D. A., Berg, E. A., Costello, C. E. & Lippard, S. J. Structural features of covalently cross-linked hydroxylase and reductase proteins of soluble methane monooxygenase as revealed by mass spectrometric analysis. *J. Biol. Chem.* **278**, 20939-20945, doi:10.1074/jbc.M301581200 (2003).

118 Fox, B. G., Liu, Y., Dege, J. E. & Lipscomb, J. D. Complex formation between the protein components of methane monooxygenase from *Methylosinus trichosporium* OB3b. *J. Biol. Chem.* **266**, 540-550, doi:10.1016/S0021-9258(18)52470-4 (1991).

119 Liu, Y., Nesheim, J. C., Paulsen, K. E., Stankovich, M. T. & Lipscomb, J. D. Roles of the methane monooxygenase reductase component in the regulation of catalysis. *Biochemistry* **36**, 5223-5233, doi:10.1021/bi962743w (1997).

120 Acheson, J. F., Bailey, L. J., Elsen, N. L. & Fox, B. G. Structural basis for biomolecular recognition in overlapping binding sites in a diiron enzyme system. *Nat. Commun.* **5**, 5009, doi:10.1038/ncomms6009 (2014).

121 Liu, K. E. & Lippard, S. J. Redox properties of the hydroxylase component of methane monooxygenase from *Methylococcus capsulatus* (Bath). *J. Biol. Chem.* **266**, 12836-12839, 24859, doi:10.1016/S0021-9258(18)98768-5 (1991).

122 Paulsen, K. E. *et al.* Oxidation-reduction potentials of the methane monooxygenase hydroxylase component from *Methylosinus trichosporium* OB3b. *Biochemistry* **33**, 713-722, doi:10.1021/bi00169a013 (1994).

123 Brazeau, B. J., Wallar, B. J. & Lipscomb, J. D. Effector proteins from P450$_{\mathrm{cam}}$ and methane monooxygenase: lessons in tuning nature's powerful reagents. *Biochem. Biophys. Res. Commun.* **312**, 143-148, doi:10.1016/j.bbrc.2003.09.242 (2003).

124 Ericson, A. *et al.* Structural characterization by EXAFS spectroscopy of the binuclear iron center in protein A of methane monooxygenase from *Methylococcus capsulatus* (Bath). *J. Am. Chem. Soc.* **110**, 2330–2332, doi:10.1021/ja00215a070 (1988).

125 Fox, B. G., Surerus, K. K., Münck, E. & Lipscomb, J. D. Evidence for a mu-oxo-bridged binuclear iron cluster in the hydroxylase component of methane monooxygenase. *J. Biol. Chem.* **263**, 10553-10556, doi:10.1016/S0021-9258(18)38005-0 (1988).

126 Wang, W., Liang, A. D. & Lippard, S. J. Coupling oxygen consumption with hydrocarbon oxidation in bacterial multicomponent monooxygenases. *Acc. Chem. Res.* **48**, 2632-2639, doi:10.1021/acs.accounts.5b00312 (2015).

127 Whittington, D. A., Rosenzweig, A. C., Frederick, C. A. & Lippard, S. J. Xenon and halogenated alkanes track putative substrate binding cavities in the soluble methane monooxygenase hydroxylase. *Biochemistry* **40**, 3476-3482 (2001).

128 Sazinsky, M. H. & Lippard, S. J. Product bound structures of the soluble methane monooxygenase hydroxylase from *Methylococcus capsulatus* (Bath): Protein motion in the α-subunit. *J. Am. Chem. Soc.* **127**, 5814-5825 (2005).

129 Brazeau, B. J. & Lipscomb, J. D. Key amino acid residues in the regulation of soluble methane monooxygenase catalysis by component B. *Biochemistry* **42**, 5618-5631, doi:10.1021/bi027429i (2003).

130 Wallar, B. J. & Lipscomb, J. D. Methane monooxygenase component B mutants alter the kinetics of steps throughout the catalytic cycle. *Biochemistry* **40**, 2220-2233, doi:10.1021/bi002298b (2001).

131 Jones, J. C., Banerjee, R., Shi, K., Aihara, H. & Lipscomb, J. D. Structural studies of *Methylosinus trichosporium* OB3b soluble methane monooxygenase hydroxylase and regulatory component complex reveal a transient substrate tunnel. *Biochemistry* **59**, 2946–2961, doi:10.1021/acs.biochem.0c00459 (2020).

132 Jasniewski, A. J. & Que, L., Jr. Dioxygen activation by nonheme diiron enzymes: Diverse dioxygen adducts, high-valent intermediates, and related model complexes. *Chem. Rev.* **118**, 2554-2592, doi:10.1021/acs.chemrev.7b00457 (2018).

133 Liu, K. E. *et al.* Characterizaton of a diiron(III) peroxo intermediate in the reaction cycle of methane monooxygenase hydroxylase from *Methylococcus capsulatus* (Bath). *J. Am. Chem. Soc.* **117**, 4987-4990, doi:10.1021/ja00122a032 (1995).

134 Lee, S.-K. & Lipscomb, J. D. Oxygen activation catalyzed by methane monooxygenase hydroxylase component: Proton delivery during the O-O bond cleavage steps. *Biochemistry* **38**, 4423-4432, doi:10.1021/bi982712w (1999).

135 Tinberg, C. E. & Lippard, S. J. Revisiting the mechanism of dioxygen activation in soluble methane monooxygenase from *M. capsulatus* (Bath): Evidence for a multi-step, proton-dependent reaction pathway. *Biochemistry* **48**, 12145-12158, doi:10.1021/bi901672n (2009).

136 Banerjee, R., Meier, K. K., Münck, E. & Lipscomb, J. D. Intermediate P* from soluble methane monooxygenase contains a diferrous cluster. *Biochemistry* **52**, 4331-4342, doi:10.1021/bi400182y (2013).

137 Lee, S.-K., Fox, B. G., Froland, W. A., Lipscomb, J. D. & Münck, E. A transient intermediate of the methane monooxygenase catalytic cycle containing an $Fe^{IV}Fe^{IV}$ cluster. *J. Am. Chem. Soc.* **115**, 6450-6451, doi:10.1016/S0021-9258(20)80579-1 (1993).

138 Liu, K. E. *et al.* Kinetic and spectroscopic characterization of intermediates and component interactions in reactions of methane monooxygenase from *Methylococcus capsulatus* (Bath). *J. Am. Chem. Soc.* **117**, 10174-10185, doi:10.1021/ja00146a002 (1995).

139 Banerjee, R., Proshlyakov, Y., Lipscomb, J. D. & Proshlyakov, D. A. Structure of the key species in the enzymatic oxidation of methane to methanol. *Nature* **518** 431-434, doi:10.1038/nature14160 (2015).

140 Castillo, R. G. *et al.* High-energy-resolution fluorescence-detected X-ray absorption of the Q intermediate of soluble methane monooxygenase. *J. Am. Chem. Soc.* **139**, 18024-18033, doi:10.1021/jacs.7b09560 (2017).

141 Shu, L. *et al.* An $Fe_2^{IV}O_2$ diamond core structure for the key intermediate Q of methane monooxgyenase. *Science* **275**, 515-518, doi:10.1126/science.275.5299.515 (1997).

142 Cutsail, G. E., 3rd *et al.* High-resolution extended X-ray absorption fine structure analysis provides evidence for a longer Fe···Fe distance in the Q intermediate of methane monooxygenase. *J. Am. Chem. Soc.* **140**, 16807–16820, doi:10.1021/jacs.8b10313 (2018).

143 Xue, G., De Hont, R., Munck, E. & Que, L., Jr. Million-fold activation of the $[Fe_2(\mu\text{-}O)_2]$ diamond core for C-H bond cleavage. *Nat. Chem.* **2**, 400-405, doi:10.1038/nchem.586 (2010).

144 Gherman, B. F., Lippard, S. J. & Friesner, R. A. Substrate hydroxylation in methane monooxygenase: Quantitative modeling via mixed quantum mechanics/molecular mechanics techniques. *J. Am. Chem. Soc.* **127**, 1025-1037, doi:10.1021/ja049847b (2005).

145 Huang, S. P., Shiota, Y. & Yoshizawa, K. DFT study of the mechanism for methane hydroxylation by soluble methane monooxygenase (sMMO): Effects of oxidation state, spin state, and coordination number. *Dalton Trans.* **42**, 1011-1023, doi:10.1039/c2dt31304a (2013).

146 Burrows, K. J., Cornish, A., Scott, D. & Higgins, I. J. Substrate specificities of the soluble and particulate methane monooxygenases of *Methylosinus trichosporium* OB3b. *J. Gen. Microbiol.* **130**, 327-3333, doi:10.1099/00221287-130-12-3327 (1984).

147 Green, J. & Dalton, H. Substrate specificity of soluble methane monooxygenase. *J. Biol. Chem.* **264**, 17698-17703, doi:10.1016/S0021-9258(19)84627-6 (1989).

148 Colby, J., Stirling, D. I. & Dalton, H. The soluble methane monooxygenase of *Methylococcus capsulatus* (Bath). Its ability to oxygenate n-alkanes, ethers, and alicyclic, aromatic and heterocyclic compounds. *Biochem. J.* **165**, 395-402 (1977).

149 Priestley, N. D. *et al.* Cryptic stereospecificity of methane monooxygenase. *J. Am. Chem. Soc.* **114**, 7561-7562, doi:10.1021/ja00045a037 (1992).

150 Valentine, A. M. *et al.* Tritiated chiral alkanes as substrates for soluble methane monooxygenase from *Methylococcus capsulatus* (Bath): Probes for the mechanism of hydroxylation. *J. Am. Chem. Soc.* **119**, 1818-1827, doi:10.1021/ja963971g (1997).

151 Liu, K. E., Johnson, C. C., Newcomb, M. & Lippard, S. J. Radical clock studies and kinetic isotope effect studies of the hydroxylation of hydrocarbons by methane monooxygenase. *J. Amer. Chem. Soc.* **115**, 939-947, doi:10.1021/ja00056a018 (1993).

152 Jin, Y. & Lipscomb, J. D. Probing the mechanism of C-H activation: Oxidation of methylcubane by soluble methane monooxygenase from *Methylosinus trichosporium* OB3b. *Biochemistry* **38**, 6178-6186, doi:10.1021/bi990068v (1999).

153 Valentine, A. M., LeTadic-Biadatti, M. H., Toy, P. H., Newcomb, M. & Lippard, S. J. Oxidation of ultrafast radical clock substrate probes by the soluble methane monooxygenase from *Methylococcus capsulatus* (Bath). *J. Biol. Chem.* **274**, 10771-10776, doi:10.1074/jbc.274.16.10771 (1999).

154 Brazeau, B. J., Austin, R. N., Tarr, C., Groves, J. T. & Lipscomb, J. D. Intermediate Q from soluble methane monooxygenase hydroxylates the mechanistic substrate probe norcarane: Evidence for a stepwise reaction. *J. Am. Chem. Soc.* **123**, 11831-11837, doi:10.1021/ja016376+ (2001).

155 Nesheim, J. C. & Lipscomb, J. D. Large kinetic isotope effects in methane oxidation catalyzed by methane monooxygenase -- evidence for C-H bond cleavage in a reaction cycle intermediate. *Biochemistry* **35**, 10240-10247, doi:10.1021/bi960596w (1996).

156 Brazeau, B. J., Wallar, B. J. & Lipscomb, J. D. Unmasking of deuterium kinetic isotope effects on the methane monooxygenase compound Q reaction by site-directed mutagenesis of component B. *J. Am. Chem. Soc.* **123**, 10421-10422, doi:10.1021/ja016632i (2001).

157 Brantner, C. A., Remsen, C. C., Owen, H. A., Buchholz, L. A. & Collins, M. L. P. Intracellular localization of the particulate methane monooxygenase and methanol dehydrogenase in *Methylomicrobium album* BG8. *Arch. Microbiol.* **178**, 59-64 (2002).

158 Cafaro, V. *et al.* Phenol hydroxylase and toluene/o-xylene monooxygenase from Pseudomonas stutzeri OX1: Interplay between two enzymes. *Appl. Environ. Microbiol.* **70**, 2211-2219, doi:10.1128/AEM.70.4.2211-2219.2004 (2004).

159 Pikus, J. D. *et al.* Recombinant toluene-4-monooxygenase: catalytic and Mossbauer studies of the purified diiron and rieske components of a four-protein complex. *Biochemistry* **35**, 9106-9119, doi:10.1021/bi960456m (1996).

160 Smith, T. J. & Murrell, J. C. Mutagenesis of soluble methane monooxygenase. *Methods Enzymol.* **495**, 135-147, doi:10.1016/b978-0-12-386905-0.00009-7 (2011).

161 Smith, T. J. & Nichol, T. in *Methane Biocatalysis: Paving the Way to Sustainability* (eds Marina G. Kalyuzhnaya & Xin-Hui Xing) 153-168 (Springer International Publishing, 2018).

162 Borodina, E., Nichol, T., Dumont, M. G., Smith, T. J. & Murrell, J. C. Mutagenesis of the "leucine gate" to explore the basis of catalytic versatility in soluble methane monooxygenase. *Appl. Environ. Microbiol.* **73**, 6460-6467, doi:10.1128/aem.00823-07 (2007).

163 Lock, M., Nichol, T., Murrell, J. C. & Smith, T. J. Mutagenesis and expression of methane monooxygenase to alter regioselectivity with aromatic substrates. *FEMS Microbiol. Lett.* **364**, doi:10.1093/femsle/fnx137 (2017).

164 Orata, F. D., Meier-Kolthoff, J. P., Sauvageau, D. & Stein, L. Y. Phylogenomic analysis of the Gammaproteobacterial methanotrophs (Order *Methylococcales*) calls for the reclassification of members at the genus and species levels. *Front. Microbiol.* **9**, 3162, doi:10.3389/fmicb.2018.03162 (2018).

165 Puri, A. W. *et al.* Genetic tools for the industrially promising methanotroph *Methylomicrobium buryatense*. *Appl. Environ. Microbiol.* **81**, 1766-1772, doi:10.1128/aem.03795-14 (2015).

166 Yan, X., Chu, F., Puri, A. W., Fu, Y. & Lidstrom, M. E. Electroporation-based genetic manipulation in Type I methanotrophs. *Appl. Environ. Microbiol.* **82**, 2062-2069, doi:10.1128/AEM.03724-15 (2016).

167 Tapscott, T., Guarnieri, M. T. & Henard, C. A. Development of a CRISPR/Cas9 system for *Methylococcus capsulatus* in vivo gene editing. *Appl. Environ. Microbiol.* **85**, doi:10.1128/AEM.00340-19 (2019).

168 Barrett, B., Charles, J. W. & Temte, J. L. Climate change, human health, and epidemiological transition. *Prev. Med.* **70**, 69-75, doi:10.1016/j.ypmed.2014.11.013 (2015).

169 Chai, X. L., Tonjes, D. J. & Mahajan, D. Methane emissions as energy reservoir: Context, scope, causes and mitigation strategies. *Prog. Energy Combust. Sci.* **56**, 33-70, doi:10.1016/j.pecs.2016.05.001 (2016).

170 Curry, C. L. Modeling the soil consumption of atmospheric methane at the global scale. *Glob. Biogeochem. Cycles* **21**, 1-15, doi:10.1029/2006GB002818 (2007).

171 Hwang, I. Y. *et al.* Biological conversion of methane to chemicals and fuels: Technical challenges and issues. *Appl. Microbiol. Biotechnol.* **102**, 3071-3080, doi:10.1007/s00253-018-8842-7 (2018).

172 Nguyen, A. D. & Lee, E. Y. Engineered methanotrophy: A sustainable solution for methane-based industrial biomanufacturing. *Trends Biotechnol.* **39**, 381-396, doi:10.1016/j.tibtech.2020.07.007 (2021).

173 Koo, C. W. & Rosenzweig, A. C. Biochemistry of aerobic biological methane oxidation. *Chem. Soc. Rev.* **50**, 3424-3436, doi:10.1039/d0cs01291b (2021).

174 Garavito, R. M. & Ferguson-Miller, S. Detergents as tools in membrane biochemistry. *J. Biol. Chem.* **276**, 32403-32406, doi:10.1074/jbc.R100031200 (2001).

175 Anishkin, A., Loukin, S. H., Teng, J. & Kung, C. Feeling the hidden mechanical forces in lipid bilayer is an original sense. *Proc. Natl. Acad. Sci. USA* **111**, 7898-7905, doi:10.1073/pnas.1313364111 (2014).

176 Bayburt, T. H. & Sligar, S. G. Membrane protein assembly into nanodiscs. *FEBS Lett.* **584**, 1721-1727, doi:10.1016/j.febslet.2009.10.024 (2010).
177 Bligh, E. G. & Dyer, W. J. A rapid method of total lipid extraction and purification. *Can. J. Biochem. Physiol.* **37**, 911-917, doi:10.1139/o59-099 (1959).
178 Massey, V. in *Flavin and Flavoproteins 1990 Proceedings of the Tenth International Symposium, Como, Italy, July 15-20, 1990* (eds B. Curti, S. Ronchi, & G. Zanetti) 59-66 (Walter de Gruyter, 1991).
179 Peng, W., Qu, X., Shaik, S. & Wang, B. Deciphering the oxygen activation mechanism at the CuC site of particulate methane monooxygenase. *Nat. Catal.* **4**, 266-273, doi:10.1038/s41929-021-00591-4 (2021).
180 Cutsail, G. E., III, Ross, M. O., Rosenzweig, A. C. & DeBeer, S. Towards a unified understanding of the copper sites in particulate methane monooxygenase: An X-ray absorption spectroscopic investigation. *Chem. Sci.* **12**, 6194-6209, doi:10.1039/D1SC00676B (2021).
181 Jodts, R. J. *et al.* Coordination of the copper centers in particulate methane monooxygenase: Comparison between methanotrophs and characterization of the $\mathrm{Cu_C}$ site by EPR and ENDOR spectroscopies. *J. Am. Chem. Soc.*, doi:10.1021/jacs.1021c07018, doi:10.1021/jacs.1c07018 (2021).
182 Chang, W. H. *et al.* Copper centers in the cryo-EM structure of particulate methane monooxygenase reveal the catalytic machinery of methane oxidation. *J. Am. Chem. Soc.* **143**, 9922-9932, doi:10.1021/jacs.1c04082 (2021).
183 Lu, Y. J. *et al.* The PmoB subunit of particulate methane monooxygenase (pMMO) in *Methylococcus capsulatus* (Bath): The Cu(I) sponge and its function. *J. Inorg. Biochem.* **196**, 110691, doi:10.1016/j.jinorgbio.2019.04.005 (2019).
184 Chan, S. I. *et al.* Redox potentiometry studies of particulate methane monooxygenase: Support for a trinuclear copper cluster active site. *Angew. Chem. Int. Ed.* **46**, 1992-1994, doi:10.1002/anie.200604647 (2007).
185 Ng, K.-Y., Tu, L.-C., Wang, Y.-S., Chan, S. I. & Yu, S. S. F. Probing the hydrophobic pocket of the active site in the particulate methane monooxygenase (pMMO) from *Methylococcus capsulatus* (Bath) by variable stereoselective alkane hydroxylation and olefin epoxidation. *ChemBioChem* **9**, 1116-1123, doi:10.1002/cbic.200700628 (2008).
186 Harms, M. J., Schlessman, J. L., Sue, G. R. & Garcia-Moreno, B. Arginine residues at internal positions in a protein are always charged. *Proc. Natl. Acad. Sci. U.S.A.* **108**, 18954-18959, doi:10.1073/pnas.1104808108 (2011).
187 Reid, C. W., Blackburn, N. T. & Clarke, A. J. Role of arginine residues in the active site of the membrane-bound lytic transglycosylase B from *Pseudomonas aeruginosa*. *Biochemistry* **45**, 2129-2138, doi:10.1021/bi052342t (2006).
188 Vita, N. *et al.* Bacterial cytosolic proteins with a high capacity for Cu(I) that protect against copper toxicity. *Sci. Rep.* **6**, 39065, doi:10.1038/srep39065 (2016).
189 Dennison, C. & Harrison, M. D. The active-site structure of umecyanin, the stellacyanin from horseradish roots. *J. Am. Chem. Soc.* **126**, 2481-2489, doi:10.1021/ja0375378 (2004).
190 Hart, P. J. *et al.* A missing link in cupredoxins: Crystal structure of cucumber stellacyanin at 1.6 Å resolution. *Protein Sci.* **5**, 2175-2183, doi:10.1002/pro.5560051104 (1996).

191 Xie, Y. *et al.* Structural reorganization of the copper binding site involving Thr15 of mavicyanin from *Cucurbita pepo medullosa* (zucchini) upon reduction. *J. Biochem.* **137**, 455-461, doi:10.1093/jb/mvi062 (2005).

192 Tian, W., Chen, C., Lei, X., Zhao, J. & Liang, J. CASTp 3.0: Computed atlas of surface topography of proteins. *Nucleic Acids Res.* **46**, W363-W367, doi:10.1093/nar/gky473 (2018).

193 Sanchez-Garcia, R. *et al.* DeepEMhancer: A deep learning solution for cryo-EM volume post-processing. *Commun. Biol.* **4**, 874, doi:10.1038/s42003-021-02399-1 (2021).

194 Bowman, S. E. J., Bridwell-Rabb, J. & Drennan, C. L. Metalloprotein crystallography: More than a structure. *Acc. Chem. Res.* **49**, 695-702, doi:10.1021/acs.accounts.5b00538 (2016).

195 Smith, S. M., Balasubramanian, R. & Rosenzweig, A. C. Metal reconstitution of particulate methane monooxygenase and heterologous expression of the pmoB subunit. *Methods Enzymol.* **495**, 195-210, doi:10.1016/B978-0-12-386905-0.00013-9 (2011).

196 Ojala, D. S., Beck, D. A. & Kalyuzhnaya, M. G. Genetic systems for moderately halo(alkali)philic bacteria of the genus *Methylomicrobium*. *Methods Enzymol.* **495**, 99-118, doi:10.1016/b978-0-12-386905-0.00007-3 (2011).

197 McLean, M. A., Gregory, M. C. & Sligar, S. G. Nanodiscs: A controlled bilayer surface for the study of membrane proteins. *Annu. Rev. Biophys.* **47**, 107-124, doi:10.1146/annurev-biophys-070816-033620 (2018).

198 Katoh, K. & Standley, D. M. MAFFT: Iterative refinement and additional methods. *Methods Mol. Biol.* **1079**, 131-146, doi:10.1007/978-1-62703-646-7_8 (2014).

199 Waterhouse, A. M., Procter, J. B., Martin, D. M. A., Clamp, M. & Barton, G. J. Jalview Version 2-a multiple sequence alignment editor and analysis workbench. *Bioinformatics* **25**, 1189-1191, doi:10.1093/bioinformatics/btp033 (2009).

200 Suloway, C. *et al.* Automated molecular microscopy: The new Leginon system. *J. Struct. Biol.* **151**, 41-60, doi:10.1016/j.jsb.2005.03.010 (2005).

201 Lander, G. C. *et al.* Appion: An integrated, database-driven pipeline to facilitate EM image processing. *J. Struct. Biol.* **166**, 95-102, doi:10.1016/j.jsb.2009.01.002 (2009).

202 Emsley, P. & Cowtan, K. Coot: Model-building tools for molecular graphics. *Acta Cryst.* **D60**, 2126-2132, doi:10.1107/S0907444904019158 (2004).

203 Adams, P. D. *et al.* PHENIX: A comprehensive Python-based system for macromolecular structure solution. *Acta Cryst.* **D66**, 213-221, doi:10.1107/s0907444909052925 (2010).

204 Pettersen, E. F. *et al.* UCSF ChimeraX: Structure visualization for researchers, educators, and developers. *Protein Sci.* **30**, 70-82, doi:10.1002/pro.3943 (2021).

205 Goddard, T. D. *et al.* UCSF ChimeraX: Meeting modern challenges in visualization and analysis. *Protein Sci.* **27**, 14-25, doi:10.1002/pro.3235 (2018).

206 Yu, S. S.-F. *et al.* Production of high-quality particulate methane monooxygenase in high yields from *Methylococcus capsulatus* (Bath) with a hollow-fiber membrane bioreactor. *J. Bacteriol.* **185**, 5915-5924 (2003).

207 Collins, M. L. P., Buchholz, L. A. & Remsen, C. C. Effect of copper on *Methylomonas albus* BG8. *Appl. Environ. Microbiol.* **57**, 1261-1264, doi:10.1128/aem.57.4.1261-1264.1991 (1991).

208 Phelps, P. A., Agarwal, S. K., Speitel, G. E., Jr. & Georgiou, G. *Methylosinus trichosporium* OB3b mutants having constitutive expression of soluble methane

monooxygenase in the presence of high levels of copper. *Appl. Environ. Microbiol.* **58**, 3701-3708 (1992).

209 Whiddon, K. T., Gudneppanavar, R., Hammer, T. J., West, D. A. & Konopka, M. C. Fluorescence-based analysis of the intracytoplasmic membranes of type I methanotrophs. *Microb. Biotechnol.* **12**, 1024-1033, doi:10.1111/1751-7915.13458 (2019).

210 Kitmitto, A., Myronova, N., Basu, P. & Dalton, H. Characterization and structural analysis of an active particulate methane monooxygenase trimer from *Methylococcus capsulatus* (Bath). *Biochemistry* **44**, 10954-10965 (2005).

211 Koo, C. W., Tucci, F. J., He, Y. & Rosenzweig, A. C. Recovery of particulate methane monooxygenase structure and activity in a lipid bilayer. *Science* **375**, 1287-1291, doi:10.1126/science.abm3282 (2022).

212 Rigort, A. & Plitzko, J. M. Cryo-focused-ion-beam applications in structural biology. *Arch. Biochem. Biophys.* **581**, 122-130, doi:10.1016/j.abb.2015.02.009 (2015).

213 Zhang, P. Advances in cryo-electron tomography and subtomogram averaging and classification. *Curr. Opin. Struct. Biol.* **58**, 249-258, doi:10.1016/j.sbi.2019.05.021 (2019).

214 Melia, C. E. & Bharat, T. A. M. Locating macromolecules and determining structures inside bacterial cells using electron cryotomography. *Biochim. Biophys. Acta Proteins Proteom.* **1866**, 973-981, doi:10.1016/j.bbapap.2018.06.003 (2018).

215 Cassidy, C. K. *et al.* Structure and dynamics of the *E. coli* chemotaxis core signaling complex by cryo-electron tomography and molecular simulations. *Commun. Biol.* **3**, 24, doi:10.1038/s42003-019-0748-0 (2020).

216 Zhu, Y. *et al.* Serial cryoFIB/SEM Reveals Cytoarchitectural Disruptions in Leigh Syndrome Patient Cells. *Structure* **29**, 82-87 e83, doi:10.1016/j.str.2020.10.003 (2021).

217 Mendonca, L. *et al.* Correlative multi-scale cryo-imaging unveils SARS-CoV-2 assembly and egress. *Nat. Commun.* **12**, 4629, doi:10.1038/s41467-021-24887-y (2021).

218 De Boer, W. E. & Hazeu, W. Observations on the fine structure of a methane-oxidizing bacterium. *Antonie Van Leeuwenhoek* **38**, 33-47, doi:10.1007/BF02328075 (1972).

219 Himes, B. A. & Zhang, P. emClarity: Software for high-resolution cryo-electron tomography and subtomogram averaging. *Nat. Methods* **15**, 955-961, doi:10.1038/s41592-018-0167-z (2018).

220 Ni, T. *et al.* High-resolution in situ structure determination by cryo-electron tomography and subtomogram averaging using emClarity. *Nat. Protoc.* **17**, 421-444, doi:10.1038/s41596-021-00648-5 (2022).

221 Braunger, K. *et al.* Structural basis for coupling protein transport and N-glycosylation at the mammalian endoplasmic reticulum. *Science* **360**, 215-219, doi:10.1126/science.aar7899 (2018).

222 Sanchez, R. M., Zhang, Y., Chen, W., Dietrich, L. & Kudryashev, M. Subnanometer-resolution structure determination in situ by hybrid subtomogram averaging - single particle cryo-EM. *Nat. Commun.* **11**, 3709, doi:10.1038/s41467-020-17466-0 (2020).

223 Kovtun, O., Dickson, V. K., Kelly, B. T., Owen, D. J. & Briggs, J. A. G. Architecture of the AP2/clathrin coat on the membranes of clathrin-coated vesicles. *Sci. Adv.* **6**, eaba8381, doi:10.1126/sciadv.aba8381 (2020).

224 Li, Z. *et al.* Subnanometer structures of HIV-1 envelope trimers on aldrithiol-2-inactivated virus particles. *Nat. Struct. Mol. Bio.* **27**, 726-734, doi:10.1038/s41594-020-0452-2 (2020).

225 Mangala Prasad, V. *et al.* Cryo-ET of Env on intact HIV virions reveals structural variation and positioning on the Gag lattice. *Cell* **185**, 641-653 e617, doi:10.1016/j.cell.2022.01.013 (2022).

226 Mastronarde, D. N. Automated electron microscope tomography using robust prediction of specimen movements. *J. Struct. Biol.* **152**, 36-51, doi:10.1016/j.jsb.2005.07.007 (2005).

227 Hagen, W. J. H., Wan, W. & Briggs, J. A. G. Implementation of a cryo-electron tomography tilt-scheme optimized for high resolution subtomogram averaging. *J. Struct. Biol.* **197**, 191-198, doi:10.1016/j.jsb.2016.06.007 (2017).

228 Zheng, S. Q. *et al.* MotionCor2: Anisotropic correction of beam-induced motion for improved cryo-electron microscopy. *Nat. Methods* **14**, 331-332, doi:10.1038/nmeth.4193 (2017).

229 Mastronarde, D. N. & Held, S. R. Automated tilt series alignment and tomographic reconstruction in IMOD. *J. Struct. Biol.* **197**, 102-113, doi:10.1016/j.jsb.2016.07.011 (2017).

230 Zheng, S. *et al.* AreTomo: An integrated software package for automated marker-free, motion-corrected cryo-electron tomographic alignment and reconstruction. *bioRxiv*, doi:doi: https://doi.org/10.1101/2022.02.15.480593 (2022).

231 Zivanov, J. *et al.* A Bayesian approach to single-particle electron cryo-tomography in RELION-4.0. *bioRxiv*, doi:https://doi.org/10.1101/2022.02.28.482229 (2022).

232 Pettersen, E. F. *et al.* UCSF Chimera--a visualization system for exploratory research and analysis. *J. Comput. Chem.* **25**, 1605-1612, doi:10.1002/jcc.20084 (2004).

233 Lee, J. *et al.* CHARMM-GUI input generator for NAMD, GROMACS, AMBER, OpenMM, and CHARMM/OpenMM simulations using the CHARMM36 additive force field. *J. Chem. Theory Comput.* **12**, 405-413, doi:10.1021/acs.jctc.5b00935 (2016).

234 Peltola, P., Priha, P. & Laakso, S. Effect of copper on membrane-lipids and on methane monooxygenase activity of *Methylococcus capsulatus* (Bath). *Arch. Microbiol.* **159**, 521-525, doi:10.1007/bf00249029 (1993).

235 Humphrey, W., Dalke, A. & Schulten, K. VMD: Visual molecular dynamics. *J. Mol. Graph.* **14**, 33-38, 27-38, doi:10.1016/0263-7855(96)00018-5 (1996).

236 Phillips, J. C. *et al.* Scalable molecular dynamics with NAMD. *J. Comput. Chem.* **26**, 1781-1802, doi:10.1002/jcc.20289 (2005).

237 Huang, J. & MacKerell, A. D., Jr. CHARMM36 all-atom additive protein force field: Validation based on comparison to NMR data. *J. Comput. Chem.* **34**, 2135-2145, doi:10.1002/jcc.23354 (2013).

238 Kolstad, C. & Urama, K. IPCC 2014 Working Group III Contribution to the Fifth Assessment Report of the Intergovernmental Panel on Climate Change. (Cambridge University, Cambridge, 2014).

239 Stavert, A. R. *et al.* Regional trends and drivers of the global methane budget. *Glob. Chang. Biol.* **28**, 182-200, doi:10.1111/gcb.15901 (2022).

240 Hanson, R. S. Ecology and diversity of methylotrophic organisms. *Adv. Appl. Microbiol.* **26**, 3-37 (1980).

241 Banerjee, R., Jones, J. C. & Lipscomb, J. D. Soluble Methane Monooxygenase. *Annu. Rev. Biochem.* **88**, 409-431, doi:10.1146/annurev-biochem-013118-111529 (2019).

242 Klepsch, M. M., Persson, J. O. & de Gier, J. W. Consequences of the overexpression of a eukaryotic membrane protein, the human KDEL receptor, in *Escherichia coli*. *J. Mol. Biol.* **407**, 532-542, doi:10.1016/j.jmb.2011.02.007 (2011).

243 Bill, R. M. *et al.* Overcoming barriers to membrane protein structure determination. *Nat. Biotechnol.* **29**, 335-340, doi:10.1038/nbt.1833 (2011).

244 Pandey, A., Shin, K., Patterson, R. E., Liu, X. Q. & Rainey, J. K. Current strategies for protein production and purification enabling membrane protein structural biology. *Biochem. Cell Biol.* **94**, 507-527, doi:10.1139/bcb-2015-0143 (2016).

245 Silverman, A. D., Karim, A. S. & Jewett, M. C. Cell-free gene expression: An expanded repertoire of applications. *Nat. Rev. Genet.* **21**, 151-170, doi:10.1038/s41576-019-0186-3 (2020).

246 Carlson, E. D., Gan, R., Hodgman, C. E. & Jewett, M. C. Cell-free protein synthesis: Applications come of age. *Biotechnol. Adv.* **30**, 1185-1194, doi:10.1016/j.biotechadv.2011.09.016 (2012).

247 Perez, J. G., Stark, J. C. & Jewett, M. C. Cell-free synthetic biology: Engineering beyond the cell. *Cold Spring Harb. Perspect. Biol.* **8**, doi:10.1101/cshperspect.a023853 (2016).

248 Karyolaimos, A., Ampah-Korsah, H., Zhang, Z. & de Gier, J. W. Shaping *Escherichia coli* for recombinant membrane protein production. *FEMS Microbiol. Lett.* **365**, doi:10.1093/femsle/fny152 (2018).

249 Hershewe, J. M. *et al.* Improving cell-free glycoprotein synthesis by characterizing and enriching native membrane vesicles. *Nat. Commun.* **12**, 2363, doi:10.1038/s41467-021-22329-3 (2021).

250 Schoborg, J. A. *et al.* A cell-free platform for rapid synthesis and testing of active oligosaccharyltransferases. *Biotechnol. Bioeng.* **115**, 739-750, doi:10.1002/bit.26502 (2018).

251 Matthies, D. *et al.* Cell-free expression and assembly of ATP synthase. *J. Mol. Biol.* **413**, 593-603, doi:10.1016/j.jmb.2011.08.055 (2011).

252 Sachse, R., Dondapati, S. K., Fenz, S. F., Schmidt, T. & Kubick, S. Membrane protein synthesis in cell-free systems: From bio-mimetic systems to bio-membranes. *FEBS Lett.* **588**, 2774-2781, doi:10.1016/j.febslet.2014.06.007 (2014).

253 Klammt, C. *et al.* Cell-free expression as an emerging technique for the large scale production of integral membrane protein. *FEBS J.* **273**, 4141-4153, doi:10.1111/j.1742-4658.2006.05432.x (2006).

254 Henrich, E., Hein, C., Dotsch, V. & Bernhard, F. Membrane protein production in *Escherichia coli* cell-free lysates. *FEBS Lett.* **589**, 1713-1722, doi:10.1016/j.febslet.2015.04.045 (2015).

255 Li, J. *et al.* Cell-free protein synthesis enables high yielding synthesis of an active multicopper oxidase. *Biotechnol. J.* **11**, 212-218, doi:10.1002/biot.201500030 (2016).

256 Lyukmanova, E. N. *et al.* Lipid-protein nanodiscs for cell-free production of integral membrane proteins in a soluble and folded state: Comparison with detergent micelles, bicelles and liposomes. *Biochim. Biophys. Acta* **1818**, 349-358, doi:10.1016/j.bbamem.2011.10.020 (2012).

257 Hein, C., Henrich, E., Orban, E., Dotsch, V. & Bernhard, F. Hydrophobic supplements in cell-free systems: Designing artificial environments for membrane proteins. *Eng. Life Sci.* **14**, 365-379 (2014).

258 Uhlemann, E. M., Pierson, H. E., Fillingame, R. H. & Dmitriev, O. Y. Cell-free synthesis of membrane subunits of ATP synthase in phospholipid bicelles: NMR shows subunit a fold similar to the protein in the cell membrane. *Protein Sci.* **21**, 279-288, doi:10.1002/pro.2014 (2012).

259 Baumann, A. *et al.* In-situ observation of membrane protein folding during cell-free expression. *PLoS One* **11**, e0151051, doi:10.1371/journal.pone.0151051 (2016).

260 Hovijitra, N. T., Wuu, J. J., Peaker, B. & Swartz, J. R. Cell-free synthesis of functional aquaporin Z in synthetic liposomes. *Biotechnol. Bioeng.* **104**, 40-49, doi:10.1002/bit.22385 (2009).

261 Sommerhalter, M., Lieberman, R. L. & Rosenzweig, A. C. X-ray crystallography and biological metal centers: Is seeing believing? *Inorg. Chem.* **44**, 770-778, doi:10.1021/ic0485256 (2005).

262 Lawton, T. J., Kenney, G. E., Hurley, J. D. & Rosenzweig, A. C. The CopC family: Structural and bioinformatic insights into a diverse group of periplasmic copper binding proteins. *Biochemistry* **55**, 2278-2290, doi:10.1021/acs.biochem.6b00175 (2016).

263 Dudley, Q. M., Nash, C. J. & Jewett, M. C. Cell-free biosynthesis of limonene using enzyme-enriched *Escherichia coli* lysates. *Synth. Biol.* **4**, ysz003, doi:10.1093/synbio/ysz003 (2019).

264 Jewett, M. C. & Swartz, J. R. Mimicking the *Escherichia coli* cytoplasmic environment activates long-lived and efficient cell-free protein synthesis. *Biotechnol. Bioeng.* **86**, 19-26, doi:10.1002/bit.20026 (2004).

265 Kenney, G. E. & Rosenzweig, A. C. Methanobactins: Maintaining copper homeostasis in methanotrophs and beyond. *J. Biol. Chem.* **293**, 4606-4615, doi:10.1074/jbc.TM117.000185 (2018).

266 Voloshin, A. M. & Swartz, J. R. Efficient and scalable method for scaling up cell free protein synthesis in batch mode. *Biotechnol. Bioeng.* **91**, 516-521, doi:10.1002/bit.20528 (2005).

267 Zivanov, J. *et al.* New tools for automated high-resolution cryo-EM structure determination in RELION-3. *eLife* **7**, doi:10.7554/eLife.42166 (2018).

268 Arp, D. J. *et al.* in *Microbial Growth on C_1 Compounds: Proceedings of the 8th International Symposium* (eds M. E. Lidstrom & F. R. Tabita) 159-166 (Kluwer Academic Publishers, 1996).

269 Holmes, A. J., Costello, A., Lidstrom, M. E. & Murrell, J. C. Evidence that particulate methane monooxygenase and ammonia monooxygenase may be evolutionarily related. *FEMS Microbiol. Lett.* **132**, 203-208 (1995).

270 Pollock, N. L. *et al.* SMA-PAGE: A new method to examine complexes of membrane proteins using SMALP nano-encapsulation and native gel electrophoresis. *Biochim. Biophys. Acta Biomembr.* **1861**, 1437-1445, doi:10.1016/j.bbamem.2019.05.011 (2019).

271 Parmar, M. *et al.* Using a SMALP platform to determine a sub-nm single particle cryo-EM membrane protein structure. *Biochim. Biophys. Acta Biomembr.* **1860**, 378-383, doi:10.1016/j.bbamem.2017.10.005 (2018).

272 Hall, S. C. L. *et al.* Influence of poly(styrene- co-maleic acid) copolymer structure on the properties and self-assembly of SMALP nanodiscs. *Biomacromolecules* **19**, 761-772, doi:10.1021/acs.biomac.7b01539 (2018).

273 Qiu, W. *et al.* Structure and activity of lipid bilayer within a membrane-protein transporter. *Proc. Natl. Acad. Sci. U S A* **115**, 12985-12990, doi:10.1073/pnas.1812526115 (2018).

274 Lontoh, S. & Semrau, J. D. Methane and trichloroethylene degradation by *Methylosinus trichosporium* OB3b expressing particulate methane monooxygenase. *Appl. Environ. Microbiol.* **64**, 1106-1114, doi:10.1128/aem.64.3.1106-1114.1998 (1998).

275 Lawton, T. J. & Rosenzweig, A. C. Methane-oxidizing enzymes: An upstream problem in biological gas-to-liquids conversion. *J. Am. Chem. Soc.* **138**, 9327-9340, doi:10.1021/jacs.6b04568 (2016).